Growth of Nanowires and Diffusion in Bimetallic Nanowires – A way to Adaptable Nanostructures

Max Planck Institute for Intelligent Systems

by

Eylül Suadiye

Stuttgart, 2023

University of Stuttgart
Faculty of Chemistry

Growth of Nanowires and Diffusion in Bimetallic Nanowires –

A way to Adaptable Nanostructures

Von der Fakultät Chemie der Universität Stuttgart zur Erlangung der Würde eines Doktors der Naturwissenschaften (Dr. rer. nat.) genehmige Abhandlung

Vorgelegt von

Eylül Suadiye

aus der Türkei

Vorsitzender des Prüfungsausschusses:	Prof. Dr. Thomas Schleid
Hauptberichter:	Prof. Gunther Richter
Mitberichter:	Prof. Dr. Eugen Rabkin
Weiterer Mitberichter:	Prof. Dr. Guido Schmitz
Tag der mündlichen Prüfung:	12.07.2023

Max-Planck-Institut für Intelligente Systeme

2023

for those who went to bring roses from the future…

Table of Contents

Abstract

Nano-objects are thought to be the building blocks for future technological devices. However, prior to integration into applications, fabrication routes and the resulting physical properties have to be explored.

This work consisting four main chapters, in which the theoretical background and experiments on 1D nanomaterials (Nanowires) are presented and discussed. Introduction to the work starts with the historical documentations of nanomaterials and fundamental theories on the growth of metallic nanostructures. It continues with the ties between nanoparticles (NPs) and nanowires (NWs) in the context of growth and crystal shapes.

After the introduction, the second chapter will discuss growth mechanisms and effects of the growth parameters on the NWs. All NWs were grown via molecular beam epitaxy (MBE). Finally, we will lay an answer how the NWs are grown with this specific physical vapor deposition technique. The resulting NWs are defect-scarce and unique in their microstructure.

In the subsequent chapters, the NWs are used as templates to investigate advanced nano-object formation. The third chapter will start with the fundamentals of diffusion theory and continues with the novel experimental observations we had at the nanoscale. Again, the experimental samples (bimetallic NWs) of this chapter are grown with the MBE system yet this time specifically designed to directly observe the nanoscale diffusion kinetics with the electron microscopy techniques.

At the last chapter of the thesis, diffusion is utilized to achieve plastic deformation of NWs. A series of experimental results will be introduced to the reader's attention and a discussion over

how the diffusion can be used effectively used to shape the nanoscale materials will be given.

Zusammenfassung

Nano-Objekte gelten als Bausteine für künftige technische Geräte. Bevor sie jedoch in Anwendungen integriert werden können, müssen die Herstellungswege und die daraus resultierenden physikalischen Eigenschaften erforscht werden.

Diese Arbeit besteht aus vier Hauptkapiteln, in denen der theoretische Hintergrund und Experimente zu 1D-Nanomaterialien (Nanodrähten) vorgestellt und diskutiert werden. Die Einführung in die Arbeit beginnt mit den historischen Dokumentationen von Nanomaterialien und den grundlegenden Theorien über das Wachstum von metallischen Nanostrukturen. Die Zusammenhänge zwischen Nanopartikeln (NPs) und Nanodrähten (NWs) im Kontext von Wachstum und Kristallformen wird betrachtet.

Nach der Einführung werden im zweiten Kapitel die Wachstumsmechanismen und die Auswirkungen der Wachstumsparameter auf die NWs diskutiert. Alle NWs wurden mittels Molekularstrahlepitaxie (MBE) gezüchtet. Abschließend wird erläutert, wie die NWs mit dieser speziellen Technik der physikalischen Gasphasenabscheidung gewachsen werden. Die resultierenden NWs sind defektarm und einzigartig in ihrer Mikrostruktur.

In den folgenden Kapiteln werden die NWs als Modell - Objekte verwendet, um die Bildung fortgeschrittener Nano-Objekte zu untersuchen. Das dritte Kapitel beginnt mit den Grundlagen der Diffusionstheorie und fährt mit den neuartigen experimentellen Beobachtungen fort, die wir auf der Nanoskala gemacht haben. Auch in diesem Kapitel werden die experimentellen Proben (Bimetall-NWs) mit dem MBE-System gezüchtet, diesmal jedoch speziell für die direkte Beobachtung

der Diffusionskinetik im Nanobereich mit Hilfe von Elektronenmikroskopietechniken.

Im letzten Kapitel der Arbeit wird die Diffusion genutzt, um eine plastische Verformung der NWs zu erreichen. Eine Reihe von experimentellen Ergebnissen wird dem Leser vorgestellt und es wird diskutiert, wie die Diffusion effektiv zur Formung von Materialien im Nanomaßstab genutzt werden kann.

1. INTRODUCTION

Experiments of scientists like Neri (1612), Glauber (1656), Orschall (1684), Cassius (1685), and Faraday (1858) were the inspiration for the founders of colloid chemistry Thomas Graham and Richard Zsigmondy who build their work on those foundations [1, 2]. Although these dates look pretty impressive when we think of utilization of nanomaterials, in fact, earliest purposeful usage of nanomaterials and their unusual effects in history actually dates further back.

The "Lycurgus cup", a piece of roman artifact dates back to the 4th century shows unusual optical effects. In transmitted light, the cup appears red; in reflected light, it displays a greenish color. Transmission electron microscopy (TEM) revealed that the wondrous color changes are traced to the presence of 70 nm diameter Au–Ag colloids dispersed in the glass [3]. Only a few, 50 to 100, other roman glasses survived the ages and found that showing a similar optical effect [4]. However, vessels reported by Flavius Vopiscus indicate that the dichromatic glasses fabricated intentionally; making them the oldest reported devices of nanotechnology [4].

As we see from the chronological order above, Even though he was not the first to put in to perspective these facts, Ostwald's definition [8] from 1914, *"Structures adopt peculiar properties if their dimensions are too small to be distinguished with the microscope, yet too big to be interpreted as molecules"* is in fact the definition of today's nanotechnology. At the same work, Ostwald foreseen two possible synthesis methods: condensation of individual molecules and dissociation of bigger parts into smaller ones, yet again describing the bottom-up and top-down approaches accurately.

The first report on structures, which can be considered whiskers, are the silver filaments dating back to the 1546. They were observed by Agricola and reported at his *"De naturafossilium libri X"*. In 1671 in his compilation of the mining activities of Europe, John Webster, cites Agricola's work; *"That in the cavities of the stones are found masses of pure silver, as also little pieces are found from the rocks, stones, or marbles, or cleaving unto them, or else most slender leaves of the silver do embrace them: or like gravel sand, or small grit, is mixed with the earth. And also nature doth form or figure pure silver into the shape sometimes of trees, sometimes of little twigs, sometimes of hairs . . ."* [5, 6]. Also Ercker's description for obtaining whiskers from the reduction of silver ores can be considered one of the early reports on formation of whiskers [7].

In the following centuries, whiskers, were mainly produced by reduction of metal sulfides and halides; Bischof 1843 [9], Kohlschütter and Eydmann 1912 [10], Leroux and Friedrich 1906 [11],. Kohlschütter 1932 [12], Brenner 1950s [13-17]. Brenner also observed near theoretical tensile strength values on whiskers during his works [13, 14]. Even though reduction processes were the most common way to synthesis of whiskers Sears used physical vapor deposition (PVD) to produce Mercury whiskers [13]. Similar to his work, we will focus on condensation of individual atoms on substrates, a bottom-up process based on PVD. We will show how to utilize, optimize and design new architectures of nanowires (NWs) using PVD, which is already well established and used at several, works in our group through the years [14-17]. While the way of obtaining the NWs is well known, little understanding of the growth kinetics of the metallic NWs was developed.

The thesis is set up as following. A fundamental overview of the molecular beam epitaxy (MBE) a specific PVD technique which is used to produce the NWs through all of this work is

given. The principles of nucleation and growth on surfaces which will provide a basic insight to atomic interactions between the metallic vapor and the substrate will put in a fundamental perspective. Two of the vapor to whisker growth theories are discussed. Afterwards, in the experimental part of this work I will explain the, growth process of single crystalline (SX) metallic NWs using the Au NWs/cold rolled Mo substrate as base system. Secondly, using the gathered information of the growth we will apply our theory to other metals and verify the growth of different SX metallic NWs and finally (iii) produce SX/SX bimetallic NW systems to directly gather information on nanoscale diffusion.

1.1 Physical Vapor Deposition and Molecular Beam Epitaxy

We can divide the thin film growth via PVD process to three main steps:

1. Production of the “building blocks” in the form of atoms, molecules or ions,

2. Transportation of the “building blocks” onto a certain substrate and

3. Condensation of these “building blocks” at the substrate surface.

These are not the only steps occur (Figure 1.4). Production step here includes all evaporation techniques, transportation has the travel from the target to the substrate as well as the diffusion over the surface and last step, which defined as condensation, includes the nucleation and connected processes. Which will be detailed as the chapter develops.

MBE process classified as a PVD method since during the first two stages no chemical reaction takes place. Since all whisker growth in this work done in MBE, brief introduction to this revolutionary technology is a need.

Not only the experimental and theoretical addition to nanoscience –in fact almost in every area of science- but also technological contribution is one of the most important aspects to advance. As in nanotechnology, for example advances in microscopy changed how we view and understand small scales. However, when it comes to some technological advancement they can be overlooked [18]. In this context, MBE as a technological advancement mostly overlooked but the impact as a PVD method can be seen in following highly important works clearly.

Allowing relatively low growth temperatures, MBE grown structures appear to have less thermodynamic defects. Control over the composition and/or doping profiles in the growth directions is another noteworthy aspect of the technique and opened the doors for the preparation of new epitaxial structures which led to fabrication of innovative devices resulted Alferov [19] and Kroemer[20] to the Nobel prize in physics. Finally yet importantly, it allowed the development of quantum structures with sizes smaller or comparable to the de Broglie wavelength of carriers. Esaki [21]; von Klitzing [22]; Tsui [23] and Störmer [24].

All the whisker specimens in this work were prepared by MBE. The whisker growth process was carried out in an Ultra High Vacuum (UHV)-MBE system (base pressure ~ 10-10 mbar). Its schematic is shown in Figure 1.1. The evaporation sources include two types: effusion cells and electron beam evaporators, which are located at the bottom of the UHV chamber. In an effusion cell, materials, in their ultrapure form, are subjected to

radiant heating until they slowly begin to evaporate. The vapor of the material is then redirected to the substrate via a small opening at one end of the evaporator. The deposition rate determined as a function of the source temperature or heater power is calibrated with a quartz balance. For some materials, a much higher temperature may be required to obtain a reasonable deposition rate. This is achieved with the electron beam evaporators. An electron gun generates a beam of high kinetic energy electrons, which is then deflected towards the source material by a set of electromagnets. MBE system is usually equipped with real-time structural and chemical characterization capabilities. In our case, the surface reconstruction and thin film growth can be monitored using reflection high-energy electron diffraction (RHEED).

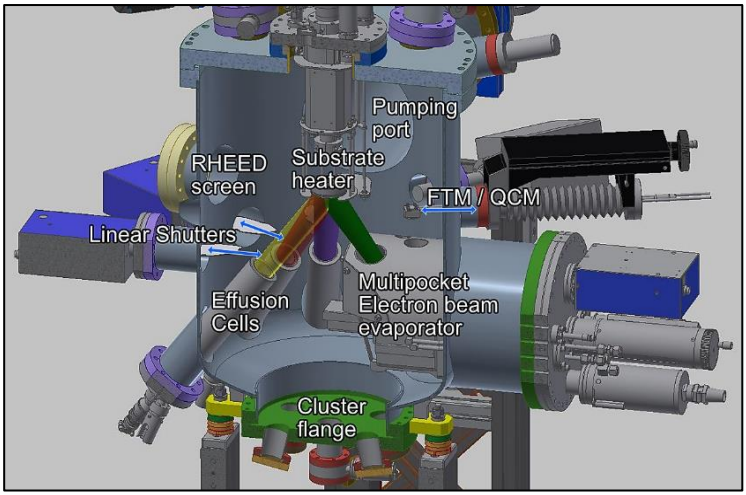

Figure 1.1 Schematics of the UHV-MBE system

When it comes to the metallic nanowhisker growth, using aforementioned parameter control aspects and surface structuring advantages of MBE, Richter et al. [25-28] have been

working intensively on this subject and have developed a reproducible deposition process, which is a reliable method to produce metallic single-crystalline and dislocation-free whiskers.

1.1.1 Fundamentals of Nucleation and Growth on Surfaces

Two approaches are commonly used in the literature to describe the nucleation and growth of adatoms on substrates. First one is the thermodynamic approach, also known as capillarity theory, which is based on a phenomenological description according to Bauer [29-30]. Based on the assumptions that the deposition occurs in thermodynamic equilibrium and it is based on the behavior of liquids; surface and interfacial energies of the layer and substrate are used to describe the growth mode. Second one is the kinetic approach, also known as the rate theory [31, 32] - takes into account various atomic processes occurring during nucleation and growth. In the following both will be briefly summarized.

1.1.2 Capillarity theory

Capillarity theory allows us to understand the important influence of surface and interfacial energies on thin film growth even though it possesses a simple concept for qualitative understanding. Missing details of atomistic assumptions gives the theory a broad generality with the power of creating useful connection between critical film nucleus size.

Atoms, which form a film in the vapor phase, are assumed to impinge on the substrate; creating aggregates that tend to either grow in size or disintegrate into smaller entities through

dissociation processes (Figure 1.2). The free-energy change accompanying the formation of an aggregate of mean dimension $\boldsymbol{r}$ is given by:

$$\Delta G = a_3 r^3 \Delta G_v + a_1 r^2 \gamma_{vf} + a_2 r^2 \gamma_{fs} - a_2 r^2 \gamma_{sv}$$

Eq. 1.1 [33]

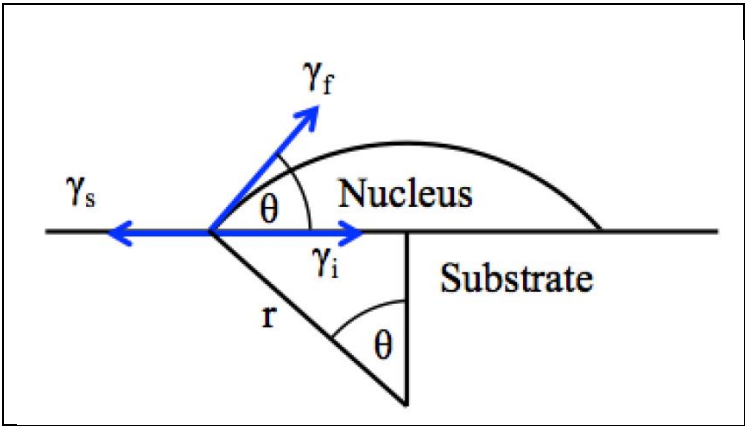

Figure 1.2 Basic atomistic processes on substrate surface during vapor deposition

Equation 1.1 has a maximum, $\boldsymbol{\Delta G}$, which is the nucleus reaches a critical size. Above this size, nuclei is stable and continues to grow with energy minimization due to volume. Below the critical size, the cluster is unstable and will not contribute to the growth of the thin film. According to Volmer and Weber [34] this energy must be expended for the formation of a nucleus of critical size. The critical nucleus size requires a critical nucleus volume $\boldsymbol{V_{crit}}$, from which the formed nucleus lowers the energy of the system, thereby $\boldsymbol{\Delta G}$ in equation 2.1 becomes negative.

$$V_k \sim exp\left(-\frac{\Delta G_0}{kT_s}\right).exp\left(-\frac{E_{diff}}{kT_s}\right).exp\left(\frac{E_{ads}}{kT_s}\right)$$

Eq. 1.2

where E_{diff} is the activation energy of surface diffusion, E_{ads} is the adsorption energy, T_s is the substrate temperature, and k is the Boltzmann constant. Due to the critical nucleation volume, there must be enough atoms in the nucleation site for a nucleus to form. For the nucleation velocity V_k, this means that it depends not only on the required nucleation energy ΔG but also on the thermally activated surface diffusion of the atoms and the desorption rate.

In mechanical equilibrium, the Young equation follows from the equilibrium of forces of the interfacial and surface energies (Figure 1.2).

$$\gamma_{sv} = \gamma_{sf} + \gamma_{vf} \cos\theta$$

Eq. 1.3

These relative surface energies indicate island growth (Volmer-Weber),

when $\theta > 0$, therefore $\gamma_{sf} + \gamma_{vf} > \gamma_{sv}$

Layer growth (Frank-van der Merwe) will be observed,

when $\theta = 0$, therefore $\gamma_{sf} + \gamma_{vf} < \gamma_{sv}$

With Θ being the wetting angle between droplet and substrate. The thermodynamic conditions for layer growth stops after a certain layer thickness. Further growth of the layers is then in competition with growth of the stable islands. This situation can

be seen in many crystal growth systems and can be classified as layer plus island, or Stranski-Krastanov growth. In other words, Frank–van der Merwe, growth mode arises because the atoms of the deposit material are more strongly attracted to the substrate than they are to themselves. In the opposite case, where the deposit atoms are more strongly bound to each other than they are to the substrate, the island, or Volmer–Weber mode results. An intermediate case, the layer-plus-island, or Stranski–Krastanov (SK) growth mode is much more common than one might think. In this case, layers form first, but then for one reason or another the system gets tired of this, and switches to islands [35].

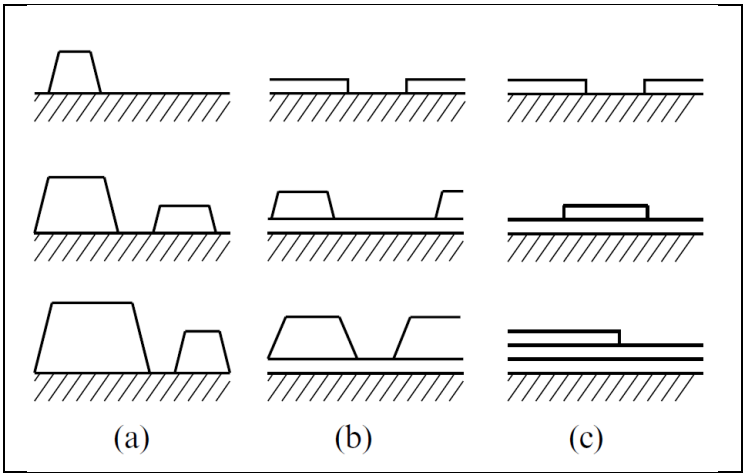

Figure 1.3 Illustration of (a) island, or Volmer–Weber growth; (b) layer-plus-island, or Stranski Krastanov growth; (c) layer-by-layer, or Frank–van der Merwe growth [35].

1.1.3 Atomic Processes in Crystal growth and rate theory

In the following section, the discussion on thermodynamic and kinetic processes will be given. It focuses especially on early stages of crystal growth. Understanding the growth phenomenon and resulting shape of crystals will open a door to discuss the NW growth path we were following in this work.

Capillary theory of vapor deposition were explained briefly during previous chapter. Here we will be focusing on rate and diffusion equations to put in perspective the foundations of atomistic processes of vapor deposition and will continue to some experimental work focusing on crystal shapes. At the end, there will be a comparison and discussion of the experimental findings in order to understand the whisker growth phenomenon.

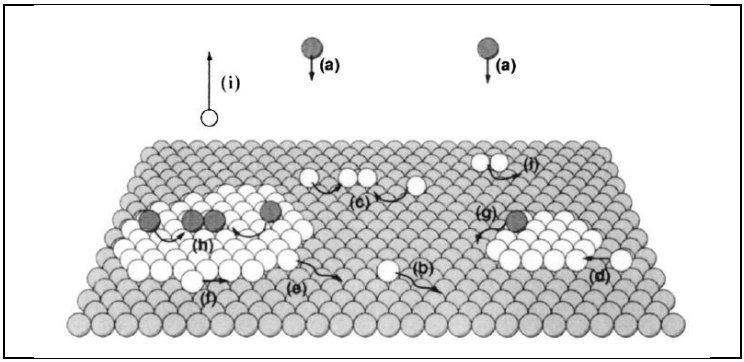

Figure 1.4 Atomistic processes during epitaxial growth [36]

Figure 1.4 shows the typical atomistic processes that occur during vapor phase deposition schematically. Here for the sake of simplification, the deposition is considered to occur onto a perfect substrate surface. They are: (a) Adsorption: atoms sent from the source with a deposition flux or deposition rate measured typically in monolayers per second. (b) Diffusion: once atoms are on the surface as adatoms, they can diffuse with a diffusion constant *D*. (c) Dimer formation/nucleation: adatoms can meet other adatoms to form a dimer. (d) Nucleus growth: attach to existing islands. (e) Decomposition: atoms which are attached to an island, they can detach from the island edge and reform adatoms. (f) Rearrangement of nuclei: or diffuse along the island edge. (g,h), Deposition of adatoms on top of islands and the corresponding processes have to be considered and (i), at high temperatures some adatoms can re-evaporate [36].

Deposition rate;

$$\boldsymbol{R = p/(2\pi mkT)^{1/2}}$$

Eq. 1.4

Where m is the atomic mass, $\boldsymbol{k}$ is the Boltzmann's constant and the $\boldsymbol{T}$ is the temperature of the vapor source. Thus single adatoms areal density $n_1(t)$ initially increases with $Rt = n_1$.

High temperatures will cause adatoms to stay on the surface shorter times. Here for the adsorption to occur there will be a time ($\boldsymbol{\tau_a}$) at a surface diffusion constant D, and this time is determined by the adsorption energy, $\boldsymbol{E_{ads}}$.

$$\boldsymbol{1/\tau_a = \nu_a \, exp\left(-\frac{E_{ads}}{kT}\right)}$$

Eq. 1.5

Here $\boldsymbol{\nu_a}$ is atomic vibration frequency. From here simple expression for the diffusion constant for two-dimensional surface diffusion can be written, in terms of the diffusion energy E_{diff}, and diffusion frequency $\boldsymbol{\nu_d}$ -which is typically less than $\boldsymbol{\nu_a}$-,

$$\boldsymbol{D = \left(\frac{\nu_d \, a^2}{4}\right) exp\left(-\frac{E_{diff}}{kT}\right)}$$

Eq. 1.6

Where a is the jump distance, typically in the order of the surface lattice mesh parameters. [36]
Above $\boldsymbol{E_{ads}}$ describes the activation energy that an adatom must overcome during desorption, $\boldsymbol{\nu_d}$ the diffusion frequency. Nuclei can form within the residence time of the adatoms. The characteristic nucleation time $\boldsymbol{\tau_n}$ [32] is the geometric mean of the monolayer arrival time $\boldsymbol{\tau_m}$ and the mean jump time upon diffusion $\boldsymbol{\tau_d}$,

$$\tau_n = (\tau_m \tau_d)^{1/2} \qquad \textit{Eq. 1.7}$$

τ_m, is calculated from the evaporation rate ϕ and the number of atoms per unit area n_1,

$$\tau_m = \frac{n_1}{\phi} \qquad \textit{Eq. 1.8}$$

And the following applies to the mean jump time for surface diffusion,

$$\tau_d = \tau_0 \, exp\left(\frac{E_{diff}}{kT}\right) = \frac{1}{v_d} \, exp\left(\frac{E_{diff}}{kT}\right)$$

$$\textit{Eq. 1.9}$$

τ_0 is the jump time of an adatom and corresponds to the inverse diffusion frequency of an adatom. Surface diffusion occurs by undirected, so-called "random-walk" motions of the adatoms on the substrate surface, where they must overcome the activation energy E_{diff} [35]. Here we can see why that D depends on the distance a between two sites, in addition to the activation energy and the absolute temperature T.

The diffusion frequency approximated by the Debye frequency and can be calculated from the Debye temperature Θ_D and Planck's quantum of action h [37].

$$\boldsymbol{v_D = \frac{\theta_D 2k\pi}{h}} \qquad \textbf{\textit{Eq. 1.10}}$$

Considering the described processes as time-dependent, the rate theory proposed by Venables and Frankl is derived [31, 32]. It describes the individual atomic processes in nucleation and growth with rate equations, where each process is defined by only one physical quantity. In this work, only the rate for the particle density of adatoms on the surface ***(n_1)*** is considered. The differential equation for the simplest case which assumes that only the desorption reduces the number of adatoms is as follows;

$$\boldsymbol{\frac{dn_1}{dt} = \phi - \frac{n_1}{\tau_a}} \qquad \textbf{\textit{Eq. 1.11}}$$

If we consider that time ***(t)*** of the process is long enough $\boldsymbol{t >> \tau_a}$ solution for the equation;

$$\boldsymbol{n_1 = \phi \tau_a} \qquad \textbf{\textit{Eq. 1.12}}$$

1.2 Crystal Shapes – Thermodynamic versus Kinetic

Gibbs [38] is the one credited with being the first to recognize that the equilibrium shape of a material, which, for a fixed volume, minimizes the surface free energy, integrated over the entire surface. Here bulk free energy is insignificant because of the volume conservation, so a constant volume of a material will minimize the surface free energy defined for that surface. The formulation of the problem also was carried out separately by Curie [39]. The solution of this is the equilibrium shape of the crystals (ECS) – also known as thermodynamic shape in literature. In the context of this thesis the term "Equilibrium shape of crystals will be used. Solution to the problem was introduced by Wulff [40] (Wulff construction) but proof was incorrect. Correct proofs came later from Hilton (1903), Liebmann (1914), and by von Laue (1943).

Even though these proofs were plausible for the theorem, they had their limitations. They were not general and applied only to T=0 for example. Dinghas [41] showed that any shape differing from the Wulff construction has a higher surface free energy. Although Dinghas again considered only a special class of polyhedral shapes.

Herring [42-43] completed the proof by showing that Dinghas′ method can be easily extended to random shapes, since the inequality is true for convex bodies in general. In their seminal paper on crystal growth, Burton, Cabrera, and Frank [44] present a novel proof of the theorem in two dimensions (2D).

1.2.1 Equilibrium and Kinetic Wulff Shapes

When ECS is formulized bulk properties such as thermal conductivity and chemical diffusivity are considered as second rank tensors, the reason comes from bulk material behavior. In bulk, a certain number of the cubic structures show isotropic behavior. Although an entire chapter of this thesis is devoted to anisotropic diffusion behavior of cubic crystals that discussion is in the nanoscale. Therefore not concerning the bulk.

Anisotropy of $(\boldsymbol{\gamma})$ creates the concept of an equilibrium shape, known as the Wulff shape; while, the anisotropy of $(\boldsymbol{\mu})$ gives rise to an analogous growth shape which is called the "Kinetic Wulff Shape" [45].

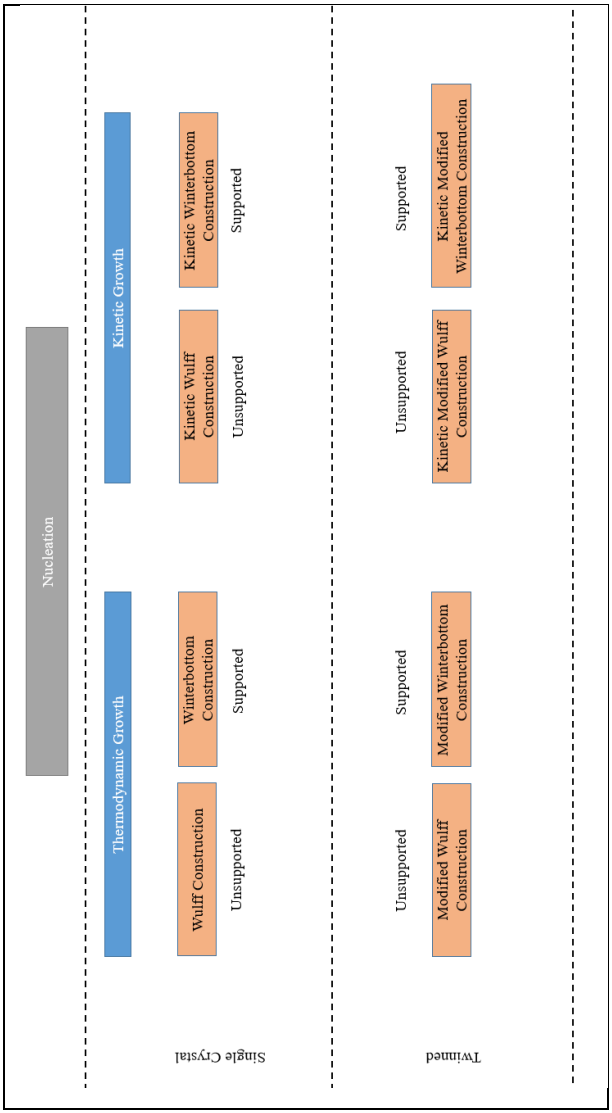

Figure 1.5 Growth paths of crystals after nucleation.

Figure 1.5 is a brief look at the crystal shape construction mechanisms. Thermodynamic branch is driven by surface energy (the surface energy here comes from the crystal plane surfaces it is not the surface energy of so called substrate from previous chapter), kinetic branch is driven by growth velocity and supported and unsupported indicates the growth medium.

Since our work is focused on flat substrates, our explanations will be focused on supported sections. However, some short general insights for unsupported structures is given. In so many works, which we can find in the literature, focus is how the shapes are constructed. Rather than explaining all this valuable information, I will be using these theories to be able to understand the growth of NWs. Reader is highly encouraged to check some of the references from this chapter to understand the vast mathematical and physical research which is going on for five decades.

1.2.2 Thermodynamic Wulff construction

Thermodynamic Wulff construction applies to the case of a single crystal in thermodynamic equilibrium. It states that the normal vector length to any external crystal facet will be proportional to the surface free energy of that facet, expressed as follows:

$$\gamma_i = h_i/\lambda \qquad \textit{Eq. 1.13}$$

where γ_i is the orientation-dependent surface free energy of a crystal facet i, h_i is the normal distance from the center of the particle to the facet i (Wulff Point), and λ is a constant related to volume.

Since equilibrium implies minimum free energy for a given volume, and since the bulk, free energy is actually independent

of shape; the goal is to determine the shape that minimizes the integrated surface free energy of the crystal. Therefore, the Wulff construction begins by creating a polar plot of the surface free energy as a function of the surface normal direction. This forms an energy surface for all crystallographic directions. Low surface energies are depicted as cups in the plot. The Wulff shape is the inner envelope which is formed by drawing a perpendicular plane through the tip of each vector attributed with the cusp direction (Figure 1.6).

Equivalently, a vector definition of surface energy can be used to produce a set of points (S_w) defining the crystal's thermodynamic equilibrium shape:

$$\boldsymbol{S_w = \{x : x.\hat{n} \leq \lambda_{\gamma(\hat{n})} \text{ for all unit vectors } \hat{n}\}}$$

Eq. 1.14

where $\hat{\boldsymbol{n}}$ is a unit vector defined by the crystallographic orientation of a facet (hkl) where $\boldsymbol{\gamma(\hat{n})}$ is the orientation dependent surface energy vector [46].

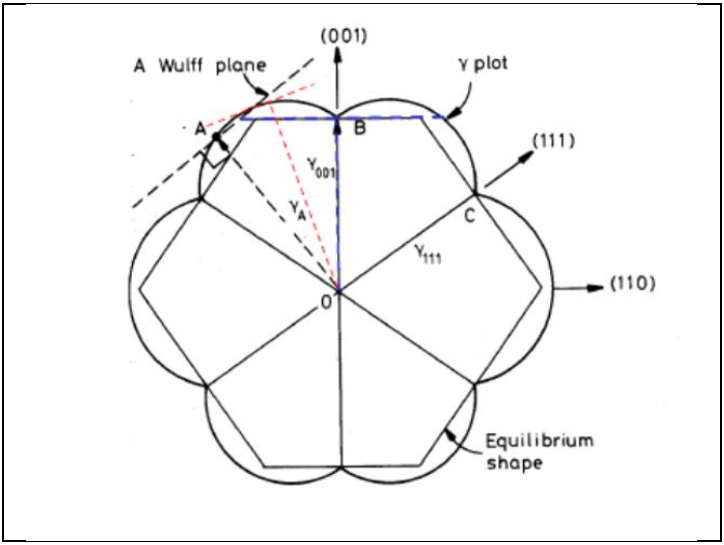

Figure 1.6 Thermodynamic Wulff Construction (Gamma Plot)

1.2.3 Kinetic Wulff Construction

General assumption we make is, given sufficient time and energy, a crystal will reach thermodynamic equilibrium. But because of the kinetic effects, many crystals have non-equilibrium shapes. The kinetic Wulff construction aims to include these effects; it was first formally used by Frank et al. in 1958 [47]. Difference in between thermodynamic and kinetic construction for single crystals is that growth velocities $\boldsymbol{v_i}$ are used rather than surface free energies ($\boldsymbol{\gamma}$i) to determine the crystal shape:

$$\boldsymbol{v_i = h_{i(t)}/\lambda_{(t)}} \qquad \textit{Eq. 1.15}$$

The facet distance from the center $\boldsymbol{h_{i(t)}}$ and the Wulff constant $\boldsymbol{\lambda_{(t)}}$ are now function of time. As a vector definition;

$$\boldsymbol{S_w = \{x : x.\hat{n} \leq \lambda_{(t)} v_{(\hat{n})} \text{ for all unit vectors } \hat{n}\}}$$

Eq. 1.16

$\boldsymbol{v_{(\hat{n})}}$ is the orientation-dependent growth velocity.

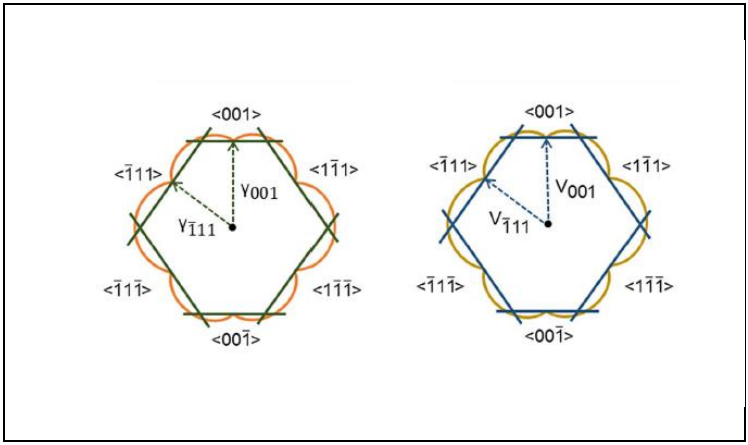

Figure 1.7 Thermodynamic and kinetic Wulff constructions. [46]

1.2.4 Modified Wulff Constructions

Unsupported particle shape construction models will be closed with this last two modified Wulff construction models. Modified here indicates the consideration of twin planes which we mostly observe at the nanoparticles (NPs) grown via MBE.

Obtaining the twinned particle shapes the modified Wulff construction can be defined for each individual single crystal sub unit of the twinned shape S_m,

$$\boldsymbol{S_m = \{x : (x - o_m).\hat{n} \leq \lambda_m \gamma_m(\hat{n}) \text{ for all unit vectors } \hat{n}\}}$$

Eq. 1.17

Here, $\boldsymbol{o_m}$ is the origin for each single crystal unit and $\boldsymbol{\gamma_m(\hat{n})}$ is the surface free energy of that unit, the surface free energy term here includes a twin facet energy $\boldsymbol{\alpha_{mn}\gamma_t}$ for each $\boldsymbol{m}$ segment neighboring a segment $\boldsymbol{n}$. Further conditions which we consider here;

$$\boldsymbol{S^t_{mn} = S^t_{nm}\ ,\ \alpha_{mn} + \alpha_{nm} = 1}$$

Eq. 1.18

$\boldsymbol{S^t_{mn}}$ is the neighboring twin surface of segment "$\boldsymbol{m}$" where it joins to segment "$\boldsymbol{n}$". Geometrically, this can be written as the following sequence of steps:

(1) Construct a Wulff polyhedron as per the standard Wulff construction for each single crystal subunit "$\boldsymbol{m}$", including the twin boundaries as facets of free energy per unit area $\boldsymbol{\alpha_{mn}\gamma_t}$, where $\boldsymbol{\gamma_t}$ is the twin boundary energy per unit area.

(2) Find the values of $\boldsymbol{\alpha_{mn}}$ and the related segments such that the twin facet has identical geometry for adjacent units and the total twin-boundary energy is correctly counted.

(3) Assemble the segments to form a space-filling structure.

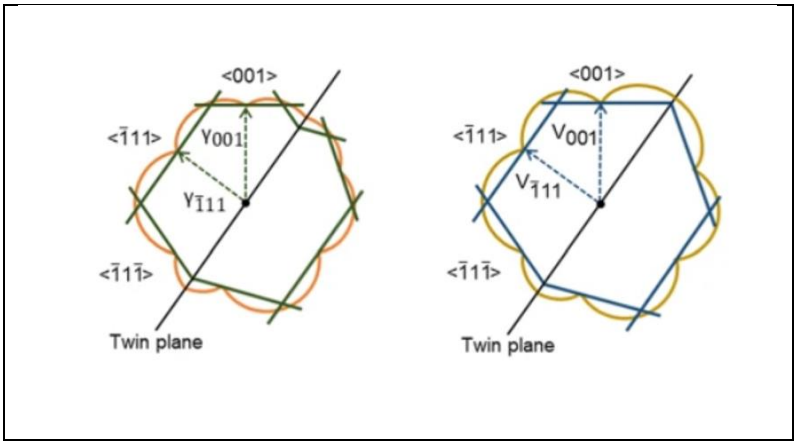

Figure 1.8 Modified thermodynamic and kinetic Wulff constructions. [46]

The simplest version is with $\boldsymbol{\alpha_{mn}}$ **= 1/2** and all $\boldsymbol{\lambda_m}$ is the same of the symmetric solution; results with a single twinned particle, while combining segments with parallel twin boundaries gives a family of laterally twinned particles (LTPs) [48](Figure 1.9).

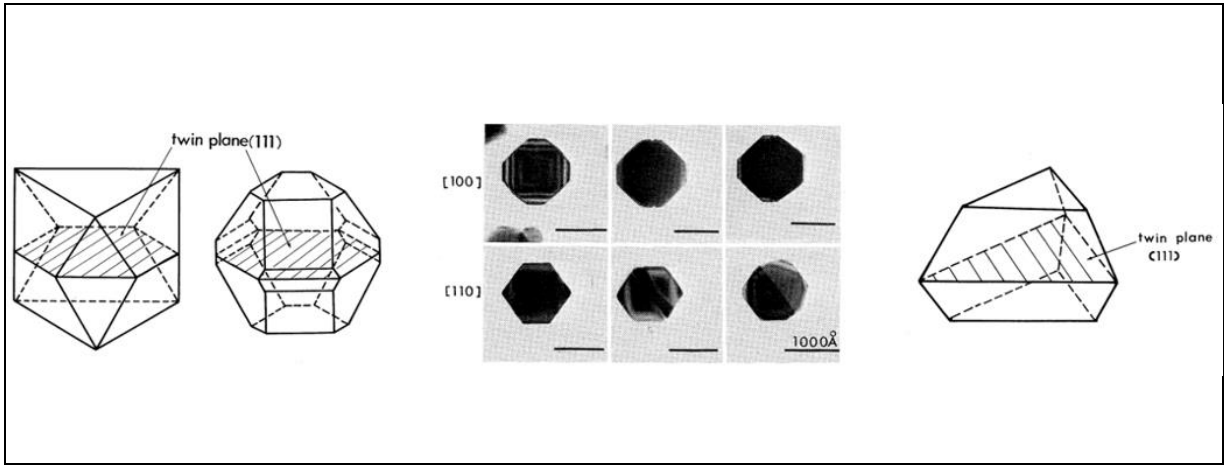

Figure 1.9 First observation of kinetic effect as single twinned particles. [48]

Using five segments each bounded by two nonparallel planes gives a decahedron (Dh); 20 segments bounded by three nonparallel boundaries, an icosahedron (Ic). These structures defined by the number of twinned segments, not the external surface. For instance, a regular icosahedron is obtained if only {111} and {100} facets are present; more complicated yet related structures arise if the {110} facets are the low energy surfaces. Asymmetric partitioning of the twin boundary ($\boldsymbol{\alpha_{mn} \neq 1/2}$) is also possible, in this case the scaling term $\boldsymbol{\lambda_m}$ for each segment will be different. When these conditions are met, asymmetric crystal shape can be observed [49].

The most common example of the modified Wulff construction for face centered cubic (FCC) materials occurs when only the {111} and {100} surfaces are the low energy surfaces, in which case one obtains the shape. (Figure 1.9).

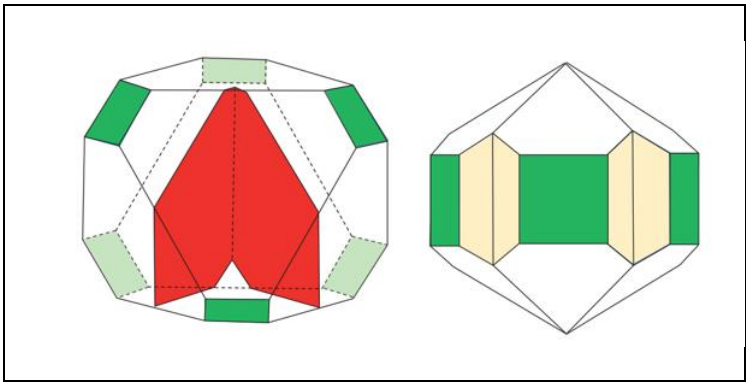

Figure 1.10 Modified Wulff construction illustrated. [50]

One feature which makes this shape different from most shapes is the presence of a re-entrant surface (Figure 1.10 Yellow marked surfaces) at the twin boundaries. On the other hand, we can see at the not twinned single crystal particles shape is

convex. This specific decahedral shape is referred at as *Marks Decahedra (Dh)*.

Even though, Marks Dh is common in literature it is just one of the shapes related to the {100}/{111} surface energy relations. If the free energy of the {100} facets is decreased such that $\gamma_{111}/\gamma_{100} = 2/\sqrt{3}$ these facets disappear and particle shape looks more like a rod. This shape first defined by Ino [51 - 53]. Note that this is a constraint thermodynamic shape and not a global minimum, in case of the {100} energy is much higher than {111} we reach the global minimum.(Figure 1.11).

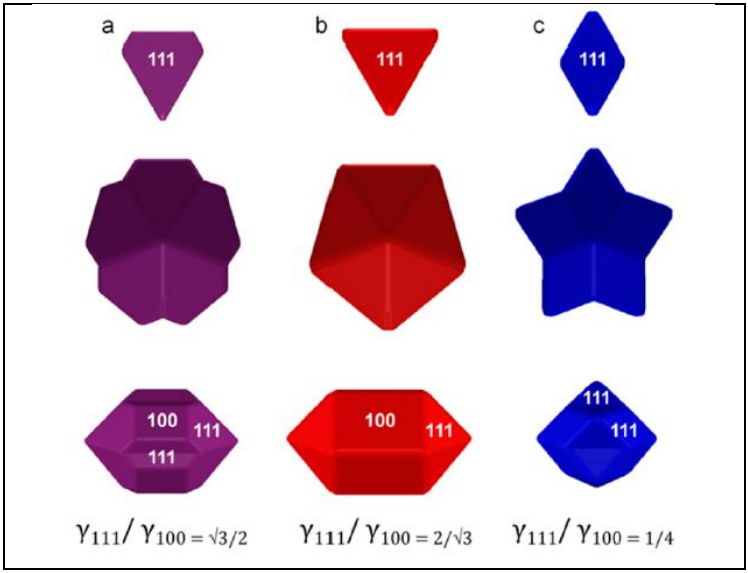

Figure 1.11 Thermodynamic Dh shapes and subunits as a function of the relative surface free energy of {100} and {111} facets.(a) Marks decahedron (b) Ino decahedron (c) Star decahedron. [54]

From here appearance of the {110} facets leads to rounded structures and lead to the icosahedral (Ic) crystals. Since the Ic

shapes are more of a thermodynamically favorable structures also their possibilities are more limited (Figure 1.12).

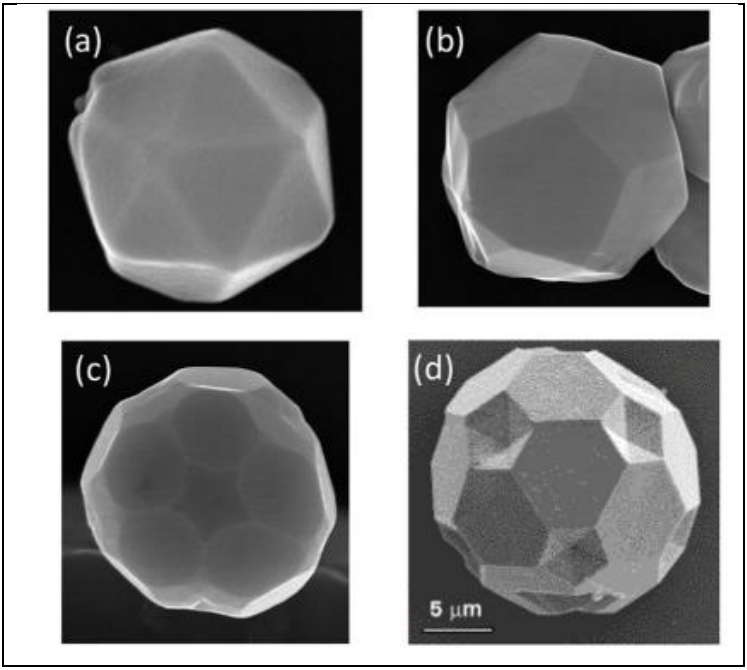

Figure 1.12 SEM images, in (a)–(c) and d) in B_6O, showing different types of Ic, a regular icosahedron with {111} facets in a), a dodecahedron with {110} in (b) and a combination of {111} and {110} in (c). In (d) the re-entrant surfaces at the twins are evident, indicating that the twin boundary energy is relatively large. [50]

1.2.5 Modified Kinetic Wulff Construction

Kinetically dominated crystals shapes as discussed above somehow related but are mostly different to the thermodynamic shapes. We can conclude from the above-mentioned constructions it is related to growth kinetics of different facets as well as mean curvature of the shape. With all these taken into account, kinetic modified Wulff construction's difference from thermodynamic equivalent is instead of surface free energies growth velocities ($\boldsymbol{v_i}$ ***as in Eq.*** $\mathbf{15}$) are used in formulation;

$$S_k = \{x : x.\hat{n} \leq \lambda_{(t)} v_{(\hat{n})} \textit{ for all unit vectors } \hat{n}\}$$

Eq. 1.19

Where $v_{(\hat{n})}$ is the orientation-dependent growth velocity.

The following rules can be summarized for the construction of the kinetic Wulff shape:

(1) Construct a kinetic Wulff polyhedron as per the standard kinetic Wulff construction by using growth velocities and taking into account the enhanced growth for concave surfaces and facets adjacent to twin boundaries or other defects such as the disclination line in a Dh.

(2) Extract the appropriate volume for each segment bounded by twin boundaries, treating these as external facets of zero growth velocity.

(3) Assemble the segments to form a space-filling structure.

An example of kinetic growth is that of a Dh; as previously mentioned, the thermodynamic growth model fails to predict the sharp particles observed experimentally. However, the kinetic model succeeds in doing so. Indeed, if the growth rate of {100} facets is fast and there is enhanced growth at the re-entrant surfaces, a sharp, slightly elongated decahedron is formed (Figure 13b) instead of the thermodynamic Marks decahedron (Figure 13a). If, in addition to re-entrant growth enhancement, the {111} facet growth is slowed down (due to surfactants, for example), sharp pentagonal bipyramids are formed, similar to that commonly obtained experimentally (Figure 13c).

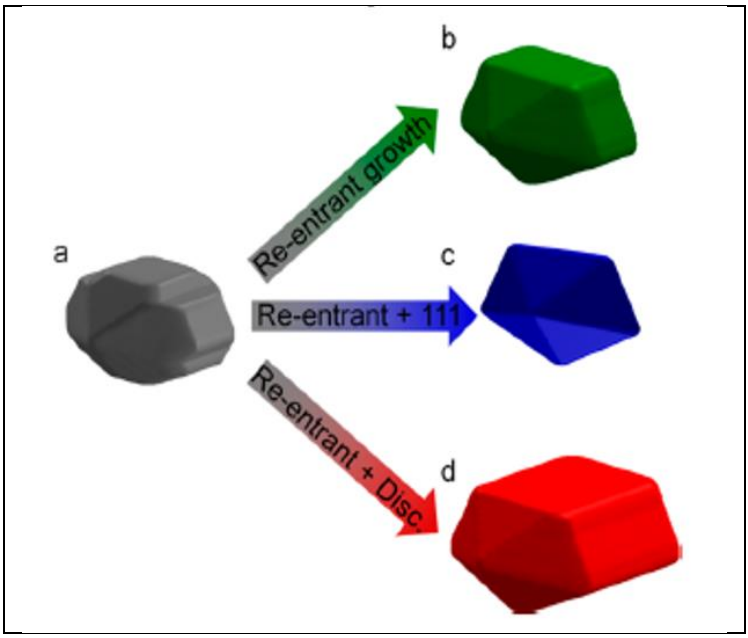

Figure 1.13 Effect of kinetic growth on Dh nanoparticles

With enhanced re-entrant and disclination growth, rods will be formed (Figure 12d) and the final result will be depending on

which faces grow fast or slow. At the end we should consider the fact that these particles are not different particles but related particles whom the shapes differ from each other because of different growth kinetics.

Kinetic model also applies to the LTPs particles at the same way as of multiple twinned particles (MTPs) (Figure 1.14).

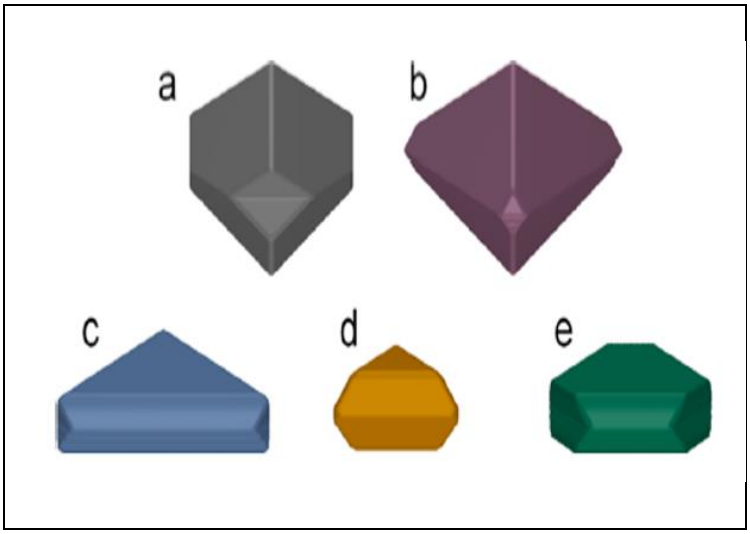

Figure 1.14 Singly twinned particle shapes obtained by varying the relative surface growth velocities and kinetic growth enhancements.

As a concluding schema we can consider the shapes we find at nanocrystals as seen at Figure 1.15. And consider three general routes to be followed.

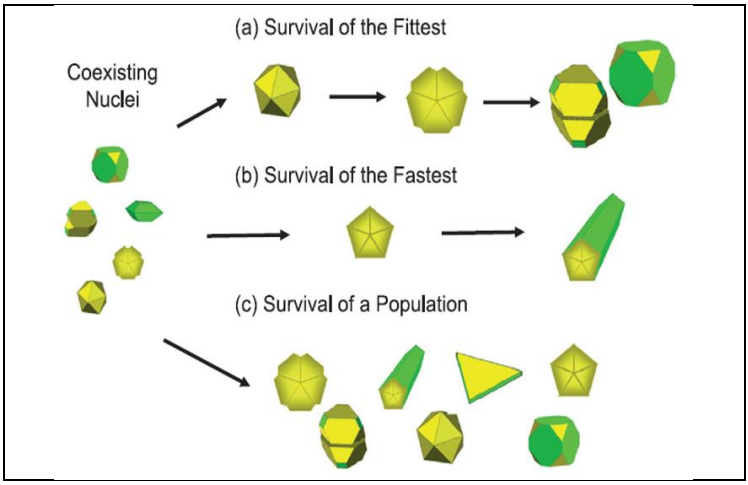

Figure 1.15 Three general routes for nanoparticle shape and structure as a function of growth.

1.3 Constructions for supported nanocrystals

1.3.1 Winterbottom construction

Wulff construction theory applies to the not supported particles and mostly nanomaterials growth is designed on a support (substrate) like in this work. In 1967 Winterbottom [55] introduced his version of growth construction which defines the crystal growth over a flat surface. Growing nanoparticles on a substrate is done for the reason, which can be observed in so many catalysis applications. When different substrate used for the same NP type the catalytic behavior of the resulting structure changes [56]. Table 1.1 shows several works done especially with gold nanoparticles which were grown over different substrates.

Table1.1 Typical metal oxide supports and typical reactions catalyzed by gold nanoparticles on them

Substrate	Electrical Properties	Reactions
Al_2O_3	insulator	aerobic oxidation of amines hydrogenation of alkenes and alkenes
SiO_2	insulator	selective oxidation of ethanol hydrogenation of nitrobenzene to aniline
TiO_2	n-type semiconductor	CO oxidation propylene epoxidation with H_2 and O_2 hydrogenation of nitrobenzene to aniline
MnO_2	p-type semiconductor	ammoxidation of alcohols to amide aerobic oxidation of sulphide
Fe_2O_3	n-type semiconductor	CO oxidation crotonaldehyde hydrogenation to crotylalcohol commercial application to odor eater (1992)
Co_3O_4	p-type semiconductor	ethylene combustion hydroformylation of alkenes
NiO	p-type semiconductor	liquid phase ethanol oxidation to acetic acid liquid phase 1-octanol to 1-octanal commercial application to MAA synthesis
ZnO	n-type semiconductor	hydrogenation of CO and CO2 hydrogenation of α, β-unsaturated aldehydes
ZrO_2	insulator	Aerobic oxidation of glucose Glycerol oxidation 5-hydroxymethyl furfural N-alkylation for secondary amine synthesis
CeO_2	insulator	water gas shift reaction Mannich reaction glucose oxidation to gluconic acid hydrogenation of crotonaldehyde

In many of these works, we can see the focus on how important is the nanoparticle shape, interface interaction and the kind of the substrate on the catalytic activity/selectivity.

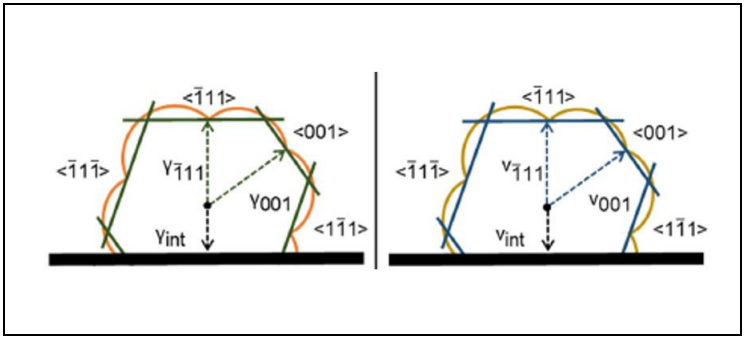

Figure 1.16 Winterbottom and kinetic Winterbottom constructions.

The Winterbottom construction (Figure 1.16) introduces a solution to determine the crystal shape grown directly over a flat surface. We do that via adding an interface to the structure, which has positive or negative adhesion energy. Together with the surface free energy, this adhesion energy defines the effective interface energy.

$$\gamma_{int} = \gamma_i + \gamma_A \qquad \textit{Eq. 1.20}$$

Here the interfacial energy (γ_{int}) replaces the surface energy term from the Wulff construction and γ_i represents surface free energy and γ_A is the adhesion energy.

If γ_A is greater than zero we have the equivalent of dewetting; if it is the negative of the surface free energy we have the equivalent of wetting with a full range in between (Figure 1.17).

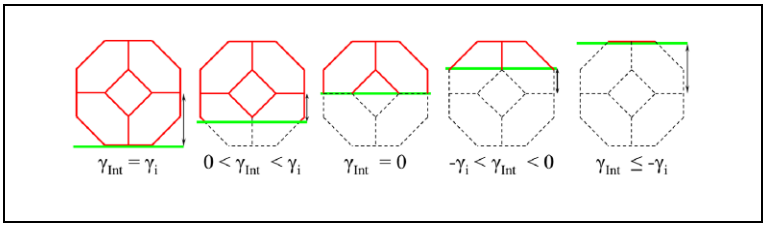

Figure 1.17 From left to right is the solid analogue of dewetting to wetting.

1.3.2 Kinetic Winterbottom Construction

This is a more recent construction, which developed to include the twin boundaries on the nanocrystals grown on a substrate. Similar to Winterbottom construction it includes an effective interfacial energy term (γ_{eff}) introduced at the crystal and substrate interface. This term is a replacement for the γ_{int} term for the single crystalline particles. With this replacement consideration of different single crystalline sub units can be modelled [57]. When the truncation height ***(h)*** changes for a crystal on a support, the areal contribution of the sub unit will change. This will directly change the contribution of effective interface energy (Figure 1.18).

$$\gamma_{eff}(h) = \sum \gamma_{int\,(\hat{n})} f_j(h) \qquad \textit{Eq.1.21}$$

Where $\gamma_{int\,(\hat{n})}$ is the orientation dependent local interfacial energy between subunit j and the substrate and $f_j$is the proportion of the total interfacial area taken up by each individual subunit.

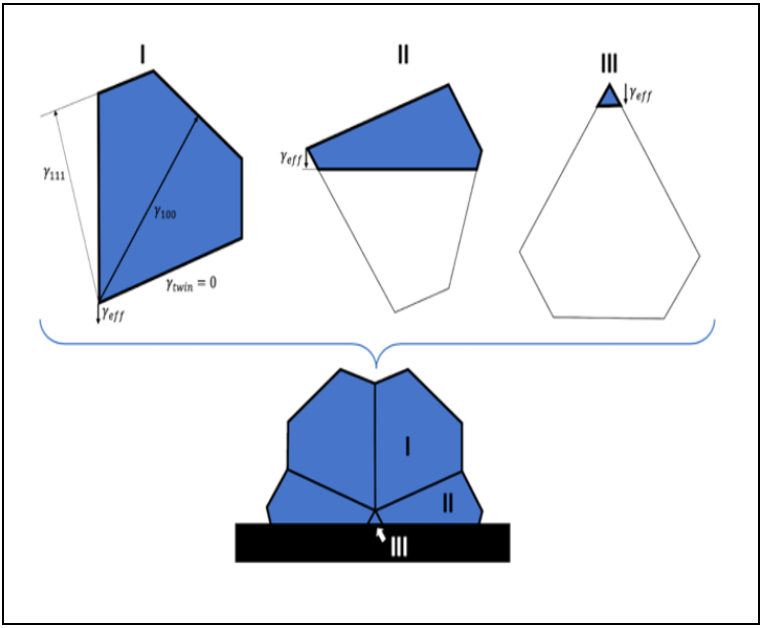

Figure 1.18 Winterbottom construction for an MTP. [57]

Thus, the minimum energy shape can be determined with the same approach for the single crystal Winterbottom construction via using γ_{eff}along the interface, resulting with a truncated height (Figure 15). A sufficient condition for a local minimum is the minimization of surface energies, which can be expressed as:

$$S = \{x : x.\hat{n} \leq \lambda_{(\hat{n})}\} \qquad Eq.1.22$$

where S represents the set of points that make up the shape of the particle and encompasses all points in a given normal

direction that are less than the product of the surface energy in that direction and a volumetric constant λ [57].

1.3.3 Particles Attached to Deformable Substrates

While Wulff construction applies to isolated particles in homogeneous mediums, as we know in many application a particle attached to a surface has practicality as mentioned before in this chapter. Winterbottom construction designs the shape of a crystal on a support material. While describing the construction with Winterbottom we for the easy solution we assume the support material as a rigid body.

However, as we will see at the NW production later in this work, particles often nucleate at the defect zones of substrates and mainly this helps elimination of the energy associated to the defects. In this case determining the crystal shape gets more complicated because a particle can distort the boundary, defect or a triple point, which is not confined to a plane. Double Winterbottom construction can be used to construct the crystal shape on a soft substrate or a grain boundary [58].

With all of these crystal shape constructions Hofmeister [59] discussed the defect-mediated growth with twin boundaries in 1D materials focused on twinned particles. His assumptions for the fivefold twinned particles growth can be associated with the ‘survival of the fastest’ (Figure 1.15) and his work directly makes a connection ‘from nanoparticles to nanowires’ supported by experimental examples.

A short summary of all Wulff shape related constructions can be seen at figure 1.19.

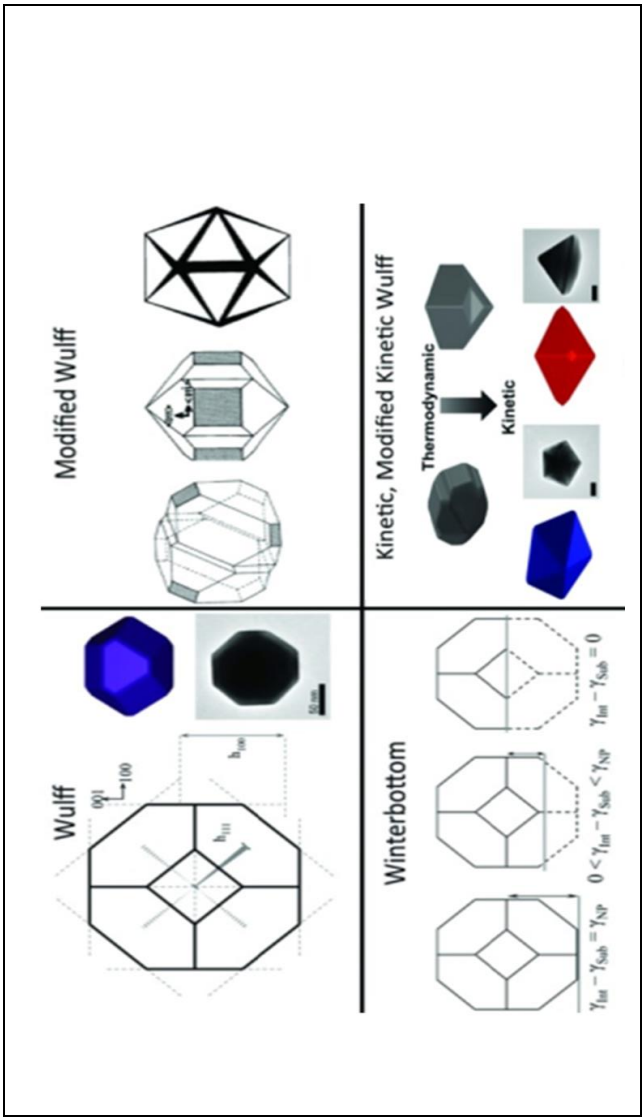

Figure 1.19 Models related to Wulff construction. [60]

2. NANOWIRE GROWTH EXPERIMENTS

In this Chapter, the experiments and observations for understanding and optimizing the growth of nanowires (NWs) are presented. While trying to define the growth mechanism and the effects of the growth parameters, the top-down approach for dissection the NW growth was implemented. In this particular context top-down method is a method of breaking a problem down into smaller, less complex pieces from the initial overall problem. Since NW growth has more than one causes to be taken into consideration, explaining those in one step is not possible. Therefore, we will break the problem into smaller pieces, explaining each piece and then bring everything back together again to connect the pieces of observations. At the beginning, we will look at the film-substrate material system and explain why this system is selected to investigate the growth. Then production process and parameters of Au NWs with a first look at the microstructural features will be described. Growth will be explained on the basis of Au NWs and the findings will be generalized for other metals at the end.

The content of this Chapter is organized as follows. Section 2.1 focuses on the description of Au-Mo NWs and the experimental setup specifically designed to understand the time effect on NWs growth. After discussing the time effect on growth, we will continue our research by studying the substrate in Sections 2.2 and 2.3. While examining the substrate we will be using different substrates to answer essential questions, like effect of surface roughness, surface energy, polycrystallinity and strain-stress on NW growth. While discussing the experiments, attention is drawn to the similarities and differences to the literature. After the summary of the results in Section 2.4, we will apply the outcomes to different metallic materials to test the

hypothesizes (Section 2.5). The Chapter ends with the characterization of some bimetallic systems that we produced to act as model systems for different aspects like diffusion, deformation and sensing capabilities at nanoscale in Section 2.6.

2.1 Au – Mo System

The main substrates in this work are cold rolled Mo sheets. They are usually used in their as-rolled state, which show a polycrystalline microstructure, without further cleaning or preparation step. Polished Mo substrates were used in comparison to the as-rolled Mo sheets as control substrate to investigate the effect of the substrate surface topography and microstructure on growth. The morphology of the NWs on the two substrates were similar, but as shown later, the density (number of NWs per area) of the NWs were different. In addition, the morphology of the islands surrounding the NWs showed differences.

Mo was chosen as main standard substrate for this work due to the following physical and chemical reasons. The physical reasons are: (i) high temperature resistivity, (ii) easy to be formed in the wanted shape, (iii) good heat conductivity. The main chemical reason is the low solubility (~ 0.9 at. %) of Au in Mo (see the Au-Mo phase diagram in Figure 2.1). Temperature resistance and conductivity is essential to our experiments, because it was already shown in previous studies [25,26,27,28] that sufficient diffusion has to occur on the substrate surface for NWs to grow. A low solubility also reduces the risk of alloy formation at the interface between film and substrate.

Detailed characterization of the substrate along with different control substrates will be given later in this chapter.

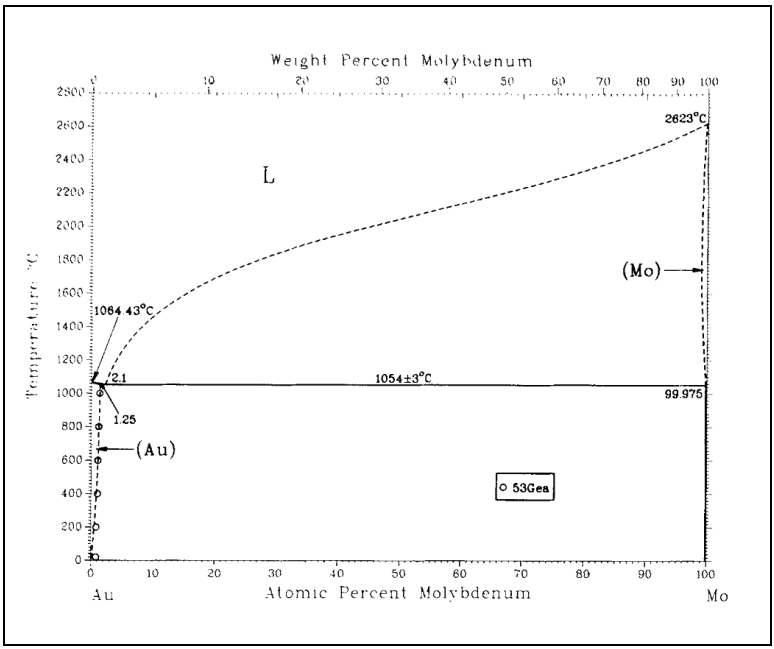

Figure 2.1 Au – Mo Binary phase diagram. [61]

2.1.1 Production process to obtain Au nanowires

The synthesis of the metal NWs with target metal Au on Mo substrate was carried out in the UHV-MBE chamber. An elevated substrate temperature is required to activate surface diffusion, which is crucial for the nucleation and subsequent growth of the NWs. In general, the growth temperature has to be above 60% of the homologous melting temperature of the film metal. For Au the substrate temperature was 760°C, which is 77% of the melting temperature. The deposition rate was 0.5 Å/s for all deposition experiments in this thesis. The deposition

rate was measured with a quartz balance. Constant rotation of the specimen plate around its surface normal was applied during the entire process to ensure the homogeneity of the deposition.

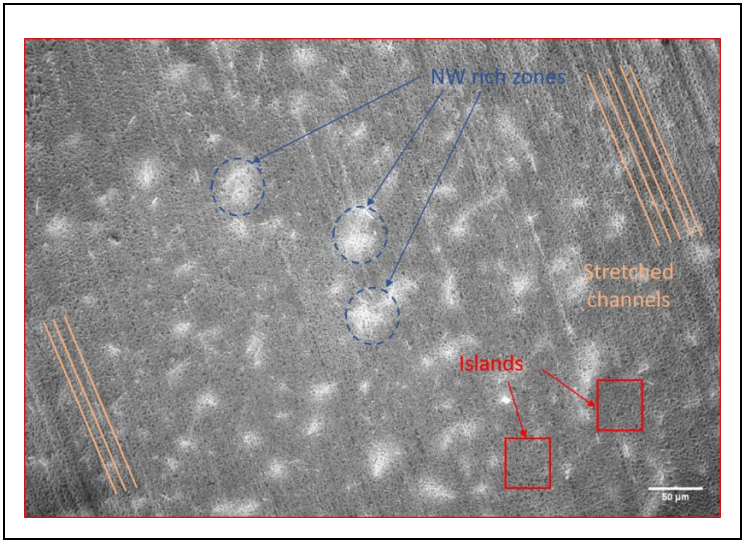

Figure 2.2 Overview SEM image after 2h Au deposition at 0.5 Å/s. SEM image.

Figure 2.2 depicts the initial low-resolution scanning electron microscope (SEM) image after 2h deposition of Au under the given growth parameters. For all Mo substrates used in this thesis, the same characteristic features can be found on the surface. The first feature are NW rich zones, which are dominant over the surface, marked in yellow in fig. 2.2. The second characteristic are clear stretched channels similar to light-colored lines on the dark background, indicated by orange lines in fig. 2.2. The third feature is the island structure, marked in green in fig. 2.2.

The phenomenological observations from SEM micrographs can be summarized as follows: NWs can be found everywhere on the substrate surface. NW rich zones are the zones where the NWs grow dominantly and they are seen as bright areas in SEM micrographs. Here, the microscope signal (secondary electrons, SE) is similar to the one obtained while observing sharp edges. Since the NWs have a show sharp edges and a prismatic body, it can be deduced, that the NW density is higher bright areas in comparison to the darker areas. Where NWs are scarce, contrast is darker. Au islands are the dominant structure at the dark areas as well as in the overall structure. The islands show flat surface facets parallel to the substrate surface. The contrast in SE-SEM imaging is formed again by the edges of the islands, which have for islands a lower density in comparison with the NWs, therefore the image appears darker. The constant material flow (deposition rate) for 2h at high substrate temperatures allow long surface diffusion distances for Au atoms. Under the given parameters, islands are the most expected structures. It can be concluded that Au growth in Volmer-Weber mode on Mo. The observed lines stem from the substrate itself because of the cold rolling production method, in which grains of the Mo metal stretch to form elongated structures as a result of milling process [62].

Figure 2.3 Side view of Au NWs on Mo substrate after a deposition time of 2 hours. Scale bar is 10 µm. SEM image.

Figure 2.3 shows side view of the sample. Here, NWs are clearly visible against the black contract of the vacuum. NWs have various lengths up to 30 µm, thickness around 100 nm and show various densities in different parts of the substrate. Additionally, islands and wavy surface of the cold rolled substrate are observable. The occurrence of all three before mentioned features is in agreement with the plain view SEM images. The islands are seemingly more homogenously distributed than the NWs, this might be an effect of the projection effect when the edge of the substrate is investigated.

Figure 2.4 depicts high resolution SE-SEM micrographs after 2 h growth, NWs and their growth origin points are shown on higher magnification. The deposition time was 2h. Various NW dimensions and lengths are visible. One of the main

observations here is that the NWs grow between the islands not from islands. However, the nature of the NW nucleation site cannot be deduced from the images. The different lengths of the NWs indicate that the NWs nucleate at different times and not all at the same time. This would be in accordance with classical nucleation theories where the nucleation is a function of the activation energies for diffusion and adhesion. It can be reasoned that technical Mo will have a variation of those energies on its surface. However, the observations raise the following important questions:

- At what deposition stage do NWs start to grow?
- And how does this relate to the island formation and growth?

Islands in the context of this thesis are three-dimensional structures on the surface which are not similar to either kinetic or thermodynamic shapes of Wulff related constructions

The assumption made in this work is that nano-particles (NPs) (see chapter 1) form first on the surface. Some of the NPs will evolve into NWs grow first and then the islands are formed from the remaining. Islands will also form on non-favored nucleation sites later in the deposition process. While islands are forming, NWs also continue their radial and axial growth therefore increase radius and length. In the 1960s, experiments were carried out by direct condensation of metals on tungsten wires at low supersaturation conditions [63, 64]. In these experiments metal was evaporated from crucibles in, at least, high vacuum and condensed on wires kept at elevated temperatures. Melmed established boundaries for growth parameters to fabricate whiskers on W field ion microscopy tips, i.e. approximate substrate temperatures and supersaturation. However, no special conditioning of the W-wire substrate was carried out and no further whisker formation mechanism was discussed. Ruth

and Hirth formulated a more general growth theory for whisker in 1964 [64]. They did a careful theoretical analysis of diffusion processes necessary for whisker lengthening. They concluded that atoms originating from two different sources are incorporated into the whiskers. First, atoms from the metal vapor impinge on the whisker side facets, diffuse to either tip or root of the whisker and are incorporated there. Second, the adatoms on the substrate formed by atoms from the vapor have, due to the elevated substrate temperature, a certain diffusion length before adhering to the substrate or desorbing. Adatoms within an area defined by the adatom diffusion length around the whisker root have a certain probability to diffuse to the root and to make a transition step from the substrate to the whisker side facets. These atoms then also could diffuse either to the tip or to the root to be incorporated. For whisker lengths below the atom diffusion length, a linear lengthening rate of the whisker is expected and observed [25]. Only at the onset of whisker growth does the contribution of adatoms diffusion on the substrate play an important role. To summarize: it is assumed, that lengthening occurs via surface diffusion, radial growth by direct impingement. These assumptions were corroborated by recent observations [37, 68].

An experimental setup was designed to confirm this assumption and extend the understanding on the NW growth process. In the next section, the experimental setup and the corresponding results are described.

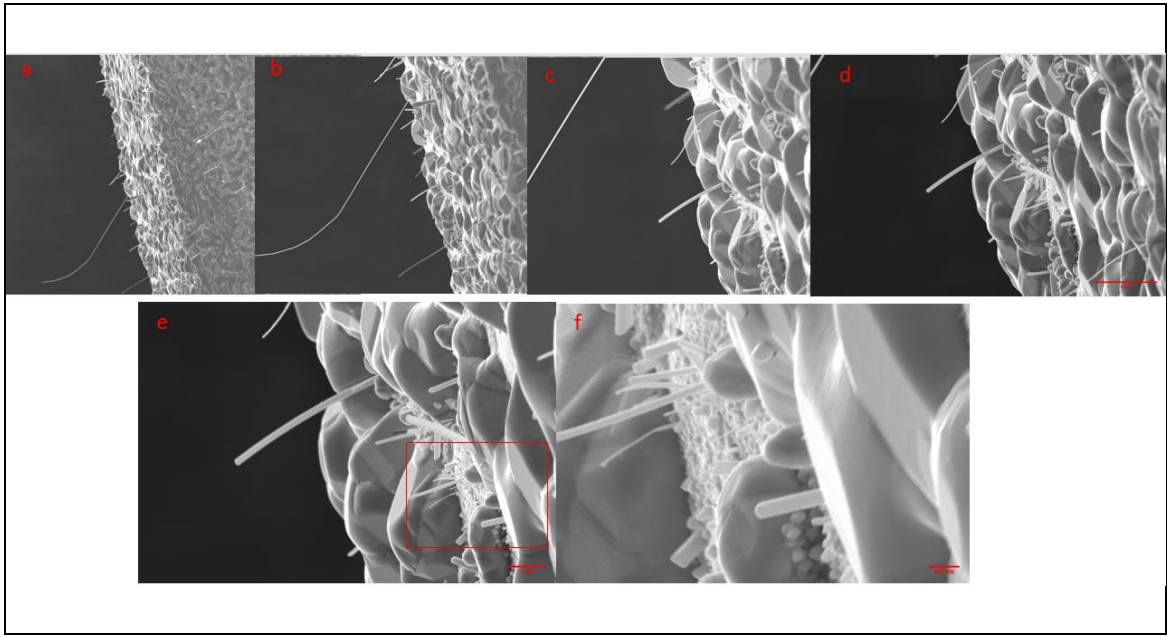

Figure 2.4 Close view of a NW rich zone of the Au NWs over a Mo substrate. The scale is decreasing from 5 µm (a), to 3 µm (b-c), 1 µm (d) and 300 nm (e-f). SEM image

2.1.2 Growth – Time experiments

To gain insight in the time sequence of NP, NW and island formation, deposition time was varied from 5 minutes to 2 hours,. The other deposition parameters and substrate temperatures were kept constant in order to understand the evolution of the growth over time. Standard, cold-rolled Mo sheets were used as substrates. Table 2.1 summarizes the parameters of the experimental setup.

Table 2.1 Experimental setup for growth-time experiments of Au NWs on Mo substrate.

Target	Deposition rate (Å/s)	Substrate (as-rolled sheet)	Substrate Temperature (ºC)	Deposition Time (min.)
Au	0.5	Mo	760	5
Au	0.5	Mo	760	10
Au	0.5	Mo	760	15
Au	0.5	Mo	760	120

Figure 2.5 shows two SEM images of the Au deposition of 5 minutes. After such a short time, both NWs and nanoparticles (NPs) are already nucleated and have been grown to a certain size. It is remarkable, that NWs grow after such a short deposition time (5 minutes). The length is already in the single µm range, diameters are below 100 nm. Apart from the NWs NPs are found. The NPs show geometrical shapes which are similar to kinetic shapes. Kinetic shapes are discussed in Chapter 1 [xx]. The absence of islands has to be pointed out. Therefore, it can be inferred that before island form

simultaneous growth of NPs and NWs occurs. The size distribution is not monodisperse.

This mechanism fits the works done on crystal shapes by Marks et.al Thermodynamics is a fundamental physical principle that governs the behavior of matter at the macroscopic and microscopic level. The goal of thermodynamics is to minimize the energy in a system and reach an energetically favorable state. In the context of nanoparticle growth, thermodynamics plays a crucial role in determining the final size and shape of the particles. The surface energy of the particles is a thermodynamic quantity that must be minimized in order to reach an energetically favorable state. This leads to the formation of nanoparticles with a spherical shape and flat facets, as described in the "Survival of the Fittest" scenario[49, 50]. In the case of kinetic growth with the rate of change of a chemical reaction. It deals with how fast or slow a reaction takes place, and how this rate depends on various factors such as temperature, pressure, and concentration of reactants. In the case of nanoparticle growth, the kinetics of the system will determine the rate at which the particles grow and their final size and shape. If the growth rate is fast, the particles will have a sharper and more defined faceted structure, as described in the "Survival of the Fastest" scenario. On the other hand, if the growth rate is slow, the particles will have a more rounded and less defined faceted structure.

In vapor phase growth, mostly we will witness this two fundamental growth mechanisms creating more complex structures. The interplay between thermodynamics and kinetics is complex and can lead to a variety of outcomes depending on the specific growth conditions. For example, if the growth conditions are such that both thermodynamics and kinetics play a significant role, the final size and shape of the particles may be a combination of both spherical and faceted structures, as

described in the "Survival of a Population" scenario. It is important to note that the relative importance of thermodynamics and kinetics can vary depending on the specific growth conditions, such as temperature, pressure, and concentration of reactants. Understanding the interplay between thermodynamics and kinetics is crucial for controlling the growth of nanoparticles [46, 50, 54, 57]. Any of these growth models can theoretically create nanowires, although the "Survival of the Fastest" scenario, where kinetic growth dominates, is often favored for the growth of nanowires. In this scenario, the fast growth rate leads to the formation of sharp, well-defined facets and rounded corners and edges, which can provide a template for the growth of nanowires with a high aspect ratio. However, it is important to note that the growth conditions and conditions for the creation of nanowires are complex and can vary depending on the specific application, and that a combination of different growth models may be involved in the formation of nanowires.

From various coexisting nuclei the fast growing NPs evolve to NWs (*survival of the fastest*, see Figure 1.15). Since not all the NPs are evolving towards NWs, we can refer to *survival of the population* for those. The surviving population will develop into islands.

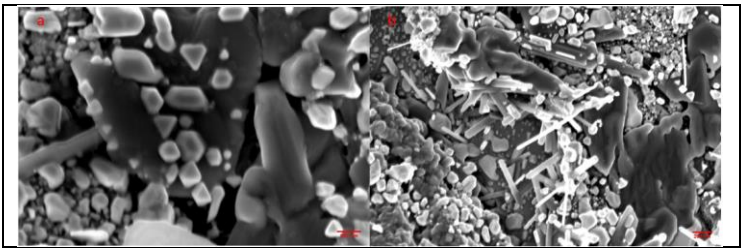

Figure 2.5 Results of the Au deposition on Mo substrate after 5 minutes. NPs similar to kinetic shapes are visible at scale bar of 100 nm (a). NWs are visible at a scale bar of 200 nm (b). SEM images.

Figure 2.6 shows three SEM micrographs of the Mo surface after 10 minutes Au deposition. Island structures are observable. Islands are more defined compared to the previous sample but NPs can still be identified. Additionally, NWs lengths and radius has increased compared to the results of the 5 minutes deposition. This is in agreement with the assumptions from Ruth and the observations from Weissmayer and Huang [37, 64, 68].

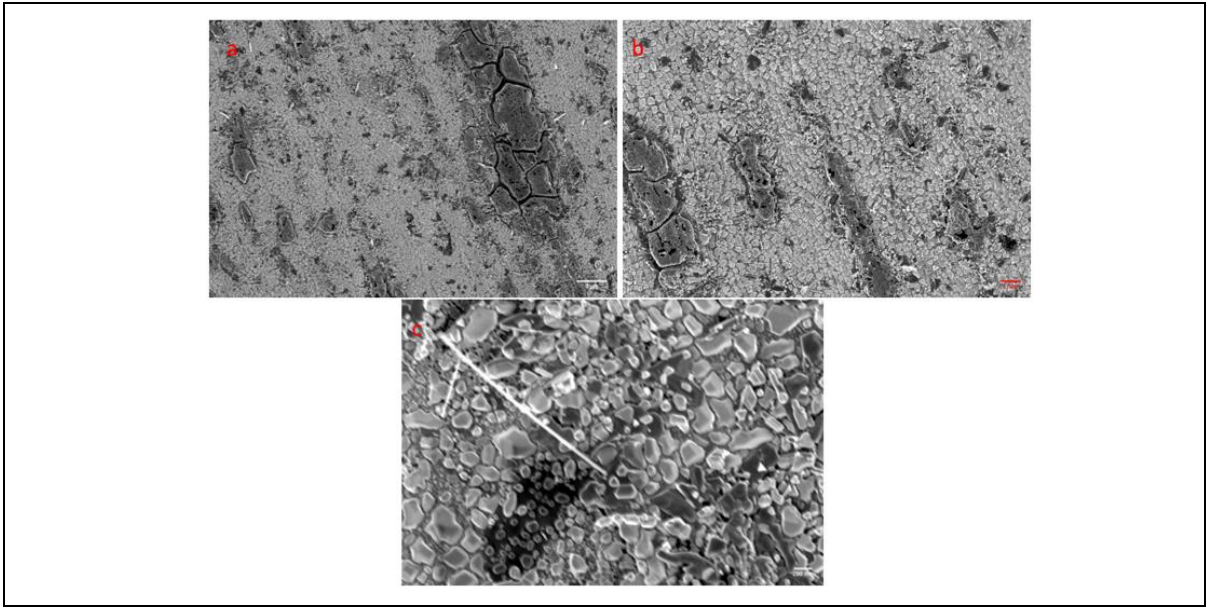

Figure 2.6 Results of Au deposition on Mo substrate after 10 minutes. Overview of the start of island structures is shown with scale bar of 3μm (a). Longer NWs alongside island are visible at a scale bar of 1μm (b). NWs, islands and NPs are visible at a scale bar of 200nm (c). SEM images.

Figure 2.7 show the results of 15 min depositions. The images do not show significant difference compared to the previous case (10 min depositions). The main differences are the island sizes and the NW lengths. With increasing size, the distinction between NPs and islands is easier to define. NPs show Wulff related shapes and whereas islands larger size particles which are result of various coalescence mechanisms like Ostwald ripening and sintering. Island structure from ~200 nm to ~400 nm alongside the NW lengths increased. This can be observed comparing Figure 2.6c and Figure 2.7c: on the latter the scale bar is double the scale of the former, indicating that the island increased roughly by a factor of 2 in size. The island morphology remain similar. At the same time, NPs with their kinetic shapes are not longer observed. Therefore, it can be assumed, that the only presence of larger islands and the absence of NPs is the result of the coalescence.

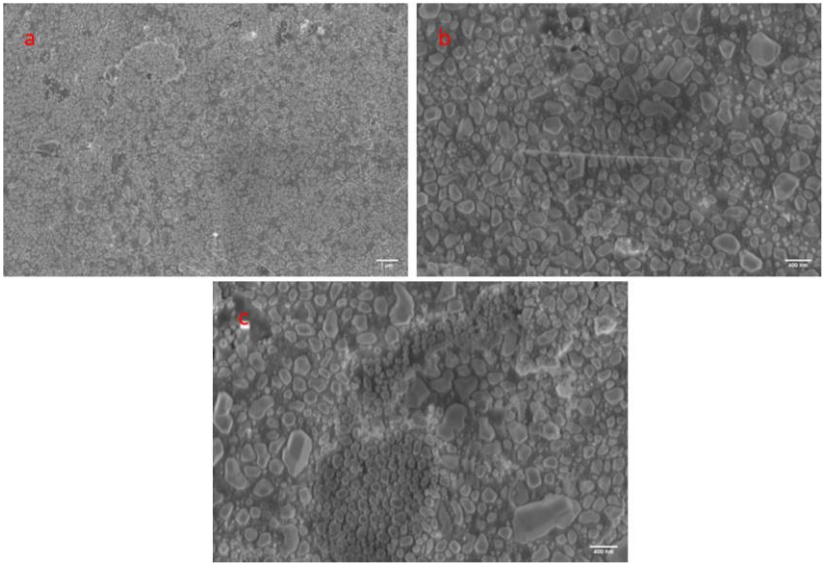

Figure 2.7 Results of the Au deposition on Mo substrate after 15 minutes. Overview of island structures is shown, scale bar is 1µm (a). NWs and islands are visible, scale bar is 400 nm (b). Island coalescence, scale bar is 400nm (c). SEM images

.

Figure 2.8 shows the results of the deposition time of two hours under identical conditions as before. As previously described in Figure 2.2, NW rich zones are visible as well as the other patterns presented in Section 2.1.1. The islands start to form a percolated structure and start to form typical growth channels.

Referencing back the two questions asked in the previous subchapter, NWs are among the first featured to be nucleated and be grown on the surface. Wulff shaped NPs nucleate at the same time. During coalescence processes island form and increase in density on the expanse of the NPs density. The NW density seems not to be affected by coalescence of island and NPs. It hast to be pointed out that not all nuclei form NPs or NW. It can be speculated that the nucleation sites of NPs and NWs differ.

The difference of the nucleation sites for NPs and NWs is still elusive. Therefore, after the characterization of the time-growth of NWs, a detailed characterization of the Mo substrate is needed. This might bring insight and more detailed information of NWs, island and cluster growth. In the next Section, the characterization of Mo substrate is introduced and in Section 2.3 the deposition results on different substrate surfaces are shown.

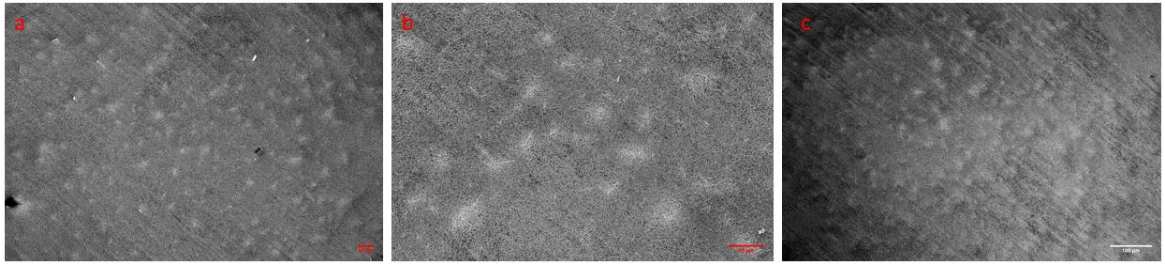

Figure 2.8 NW rich zones in different 2h deposition samples. In pictures (a) and (b) scale bar is 30µm. In picture (c) scale bar is 100µm. SEM images.

.

2.2 Substrate

Nucleation is affected by the surface morphology due to local variations of surface, diffusion and adhesion energies. Therefore, a characterization of the Mo substrate surfaces was carried out by scanning electron and laser microscopy. Figure 2.9 depicts as-rolled Mo substrates (a) and polished Mo substrates (b). The insets provide 3D surface mapping and roughness measurements. The polished Mo sheets act as control sample to separate the influence of roughness on growth. The latter samples were obtained by metallurgical sample preparation.

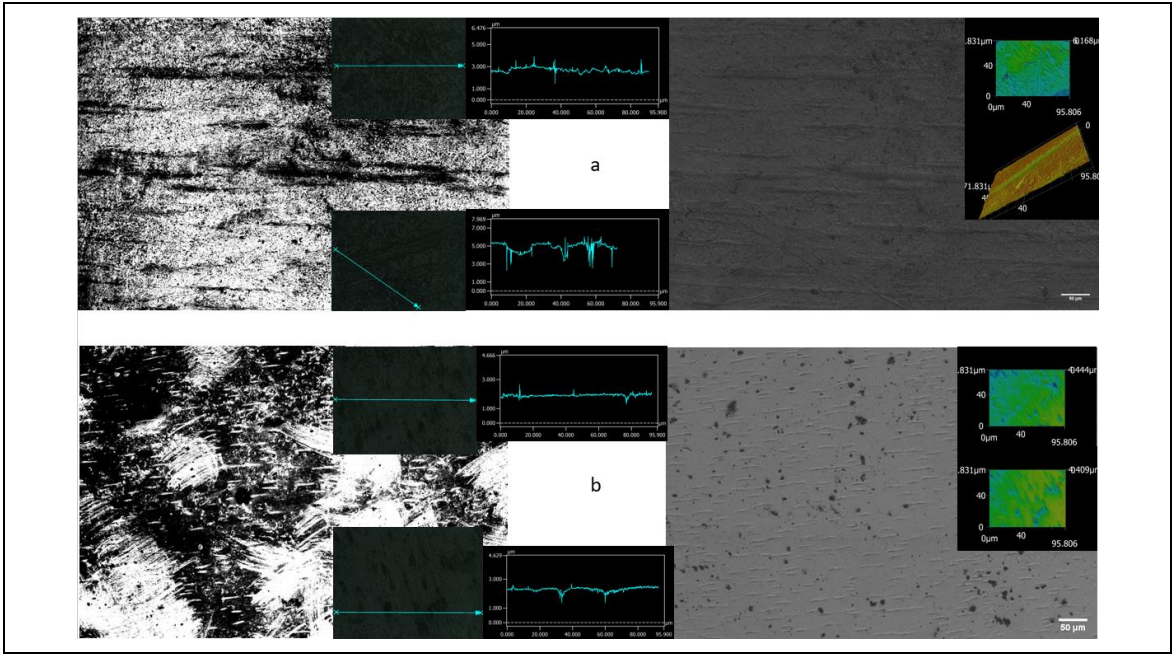

Figure 2.9 SEM images of Mo substrates, left In-lens and right SE2. Roughness measurements and laser microscope 3D surface mapping of the surface also included. (a) Mo substrate as-rolled. (b) Mo substrate polished. Scale bars are 50µm

The effect of polishing can be clearly seen in the roughness measurements. For as-rolled substrates roughness is in between 1,5 µm to 5 µm . It decreases to 0,5 µm to 1,5 µm on polished substrate. The as-rolled Mo substrate has a continuous surface roughness due to the nature of the cold-rolling process. This surface roughness is distributed uniformly across the substrate surface, and it can be observed under a microscope as a series of parallel lines or grooves. On the other hand, the polished Mo substrate has a more localized roughness, meaning that the surface irregularities are concentrated in specific areas rather than distributed uniformly. These localized irregularities are often caused by polishing scratches, which create micro cavities on the substrate surface.. The polishing process resulted not in a perfect mirror finish. A closer look revealed surface irregularities for both as-rolled and polished samples (Figure 2.10). Surface irregularities might be important aspect for the nucleation process. Surface irregularities of as-rolled substrate samples are seen as valleys, small particles and channels. On the polished samples the valley structure is almost eliminated, as shown by the roughness measurements (Figure 2.9). However, some micro cavities have been created during the polishing process. These are not homogenously distributed and exhibit a rather local occurrence (Figure 2.10). Micrographs of higher magnification show the dominant surface structures for both as-rolled and polished samples. For as rolled Mo, protrusions, particles and irregularities are seen; for polished Mo grooves from polishing are dominant (Figure 2.11).

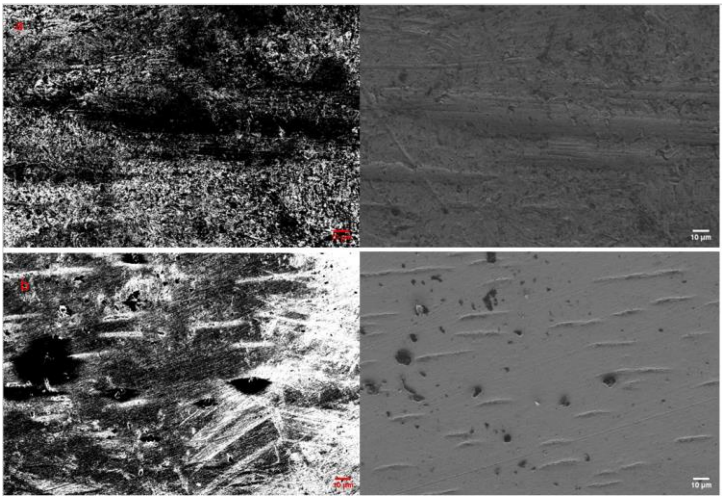

Figure 2.10 SEM images of Mo substrates, left In-lens and right SE2. (a) a closer look Mo as-rolled substrate surface . (b) a closer look to Mo polished sample some local microcracks over the polished samples can be observed. Scale bars are 10µm.

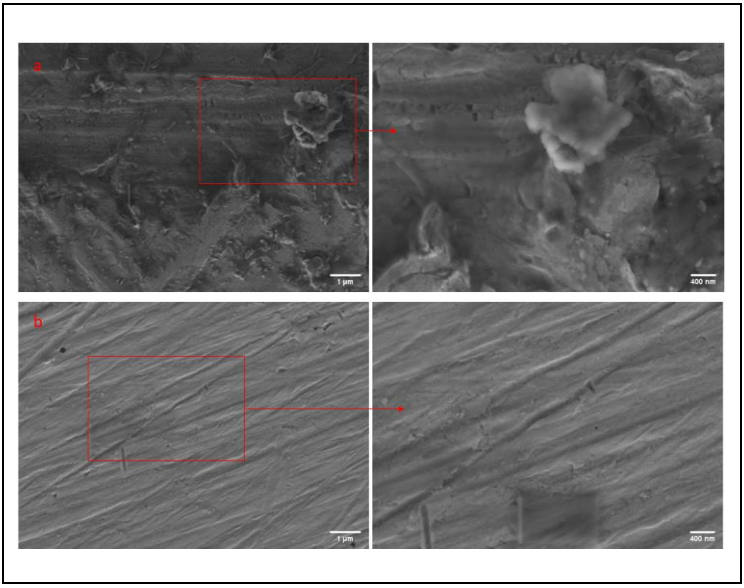

Figure 2.11 SEM images of Mo substrates. (a) Mo as-rolled sample, surface irregularities and single particle. (b) In-lens Mo polished sample, surface trails of polishing. Scale bar is 1 µm (left) and 400 nm (right).

A second set of substrates, α-Al_3O_3; sapphire, was chosen to investigate the role of roughness on growth. However, by changing the substrate material the macroscopic substrate surface energy is also changed. Also adhesion and diffusion will be different on sapphire compared to Mo. Similar to Mo, rough sapphire and polished sapphire were chosen. Therefore, the influence of two main macroscopic surface characteristics parameters is investigated in this Section: (i) surface roughness and (ii) surface energy. The atomistic energies still remain elusive under these investigations. The already established

growth parameters for NWs growth (see Section 2.1) and are kept and are presented in table 2.2.

Table 2.2 Experimental setup for investigating the effect of roughness on Au NW growth on Mo substrate.

Target	**Deposition rate (Å/s)**	**Substrate (as-rolled sheet)**	**Substrate Temperature (ºC)**	**Deposition Time (min.)**
Au	0,5	Mo as-rolled	760	120
Au	0,5	Mo polished	760	120
Au	0,5	Sapphire rough	760	120
Au	0,5	Sapphire polished	760	120

The sapphire is single-crystalline, therefore this set of experiment will additionally determine the effect of the polycrystalline nature of the Mo substrates on NW growth. Using the regular polished sapphire samples we aimed to understand the NP shape evaluation. By using the rough surface of the sapphire substrates we were able to determine the effect of surface irregularities (microcracks, roughness, etc.) without any underlying polycrystalline structure. Additionally, the influence of the chemical activity of the substrate surface is investigated.

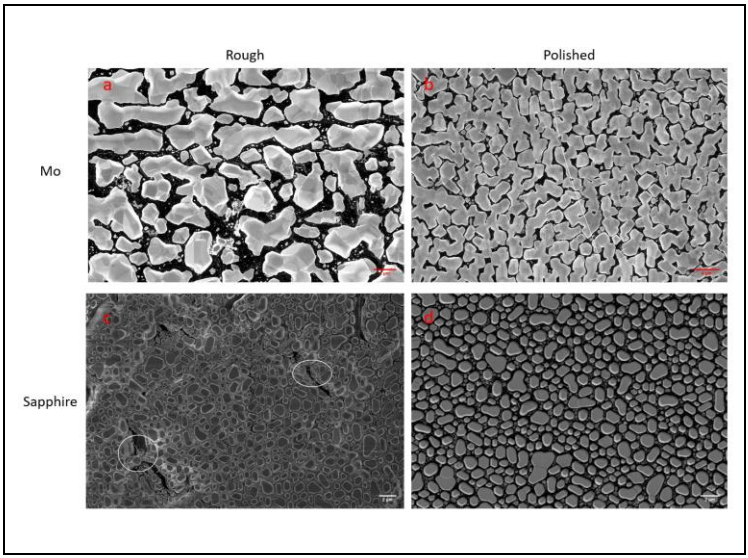

Figure 2.12 SEM micrographs. Comparison of 2h Au deposition on Mo substrate. (a) Mo as-rolled substrate, scale bar is 2µm. (b) Polished Mo, scale bar is 4µm. (c) Sapphire rough surface, scale bar is 2µm. (d) Polished sapphire, scale bar is 2µm.

Figure 2.12 shows an overview of the Au microstructure and morphology after applying the standard deposition parameters. Mo substrates show a similar morphology (Figure 2.12, a and b). The rough surface shows an island structure which can be described as percolated, the flat surface shows separated flat islands. Even though islands structure of same substrate samples is similar, rough substrates, Mo as-rolled and rough sapphire, both show similar structures for NPs and NWs (submicron structures).Sapphire substrates show similar island structure (Figure 2.12, c and d). The islands are of comparable size. Whereas the rough substrate shows a percolated island structure, the Au growth in isolated island on the flat surface. Both island structures are surrounded by smaller island due to

secondary nucleation. Both substrates with surface irregularities have higher count of NWs. Here we can infer that the surface roughness affects the NW growth. Yet, on rough sapphire NW rich zones (shiny clusters) are not visible, even that NWs grow. It can be speculated that the polycrystallinity of the Mo substrates play a role on NW growth.

2.3.1 Effect of surface roughness

Surface roughness is known to affect macroscopic surface energy of a material. Substrate surface energies were measured via contact angle measurements and were calculated using Fowkes Model. The Fowkes model is related to the contact angle test, which is a method for measuring the wetting behavior of liquids on solid surfaces. The contact angle is defined as the angle formed between the liquid-vapor interface and the solid surface at the three-phase contact line. The Fowkes model predicts the contact angle of a liquid on a solid surface based on the surface energies of the solid and liquid, as well as the surface tension of the liquid-vapor interface. The model takes into account both the dispersive and polar components of the solid surface energy, and predicts the contact angle as a function of these parameters.

In practice, the contact angle test is performed by measuring the angle formed between the liquid-vapor interface and the solid surface, and then comparing the measured angle to the prediction of the Fowkes model. This can provide information about the wetting behavior of the liquid on the solid surface, and can be used to optimize the surface energy of the solid for specific applications. [63]. For contact angle measurements for each substrate, six contact angles were measured for DI water (polar liquid) and six for diiodomethane (non-polar liquid). Table 2.3 shows the corresponding surface energies. It has to be

pointed out, that this type of measurement results in a surface energy of the macroscopic surface.

Table 2.3 Surface energies of the considered substrates.

Substrate	Surface energy of solid
Mo as rolled	45.50 ± 0.91 mN/m
Mo polished	53.80 ± 1.07 mN/m
Sapphire rough	45.25 ± 0.90 mN/m
Sapphire polished	50.61± 1.01 mN/m

From the surface energy measurements, it is seens that the original Mo as-rolled substrate shows the same macroscopic surface energy as the rough sapphire substrate. The surface energy of the substrate affects the final size and shape of the islands, NPs and NWs. The surface energy is a thermodynamic quantity that reflects the interaction between the surface and the surrounding environment, including the substrate surface. When NPs or NWs grow on a substrate, they interact with the substrate surface and its surface energy. The thermodynamic goal of the NPs and NWs is to minimize their own surface energy and reach an energetically favorable state.

Since the macroscopic surface energies are in a similar value range, but the growth morphologies differ, it has to be concluded, that the macroscopic surface energy is a to averaging parameter to describe NW and NP formation. In the case of nanoparticle (NP) and nanowire (NW) growth on a substrate surface, the surface irregularities and corresponding microscopic surface energy play an important role in determining the final size and shape of the NPs and NWs. Additionally, the surface irregularities of the substrate can

influence the growth kinetics of NPs and NWs, affecting the rate at which they grow and the final size and shape.

If the substrate surface is irregular, the NPs and NWs will experience different surface energies at different locations, which will affect their growth kinetics. These localized surface energies can be defined as microscopic surface energies and should not mixed with the macroscopic measurements on table 2.3. This will lead to the formation of NPs and NWs with a more complex, faceted structure, as opposed to a spherical structure. This is because the irregular substrate surface provides a kinetic pathway for the NPs and NWs to grow along, resulting in a final size and shape determined by the interplay between the microscopic substrate surface and the NPs or NWs.

The density and the shape of the nuclei is determined by surface and interface energies [33, 69]. Interface energy governs orientation. Comparing the growth morphologies on the different substrates, gives the first important points explaining the NW growth. We were never able to observe NWs on polished sapphire substrate. When we look at the Au island structure on polished sapphire (Figure 2.12c, Figure 13) islands are relatively homogeneous and showing mostly flat surfaces (wetting behavior) Wetting behavior in vapor phase deposition refers to the interaction between the deposited material and the substrate surface. Depending on the surface energy of the substrate and the deposited material, the wetting behavior can be either wetting or non-wetting. If the surface energy of the deposited material is greater than that of the substrate, the material will spread out and wet the substrate, forming a continuous film. On the other hand, if the surface energy of the substrate is greater than that of the deposited material, the material will not spread out and form isolated droplets. The wetting behavior in vapor phase deposition can be influenced by various factors, including the substrate temperature, the

deposition rate, and the chemical composition of the deposited material. [35].

Edges of the islands are less defined compared to all other substrates. It is known, that Au growth epitaxial on Sapphire and our observations shows that when epitaxial growth is observed NW growth is not observered (Figure 2.12d). The overall shape of the islands, which is not close to the Wulff shape, indicates that coalescence process already occurred and that surface diffusion on the substrate and the island is active.

The standard Mo substrate has within the error bars the same macroscopic surface energy, however the growth morphology is completely different to the flat sapphire substrate.

Surface irregularities together with corresponding surface energy result in kinetic-shaped NPs and NWs.

In the case of nanoparticle (NP) and nanowire (NW) growth on a substrate surface, the surface irregularities and corresponding surface energy play an important role in determining the final size and shape of the NPs and NWs. The surface irregularities of the substrate can influence the growth kinetics of NPs and NWs, affecting the rate at which they grow and the final size and shape.

The surface energy of the substrate also affects the final size and shape of the NPs and NWs. The surface energy is a thermodynamic quantity that reflects the interaction between the surface and the surrounding environment, including the substrate surface. When NPs or NWs grow on a substrate, they interact with the substrate surface and its surface energy. The

goal of the NPs and NWs is to minimize their own surface energy and reach an energetically favorable state.

If the substrate surface is irregular, the NPs and NWs will experience different surface energies at different locations, which will affect their growth kinetics. This will lead to the formation of NPs and NWs with a more complex, faceted structure, as opposed to a spherical structure. This is because the irregular substrate surface provides a kinetic pathway for the NPs and NWs to grow along, resulting in a final size and shape determined by the interplay between the substrate surface and the NPs or NWs.

In summary, the surface irregularities and corresponding surface energy of the substrate play a crucial role in determining the final size and shape of NPs and NWs when they grow on a substrate surface. The surface irregularities provide a kinetic pathway for the NPs and NWs to grow along, while the surface energy influences the energetics of the system, leading to a final size and shape that balances both kinetic and thermodynamic considerations.

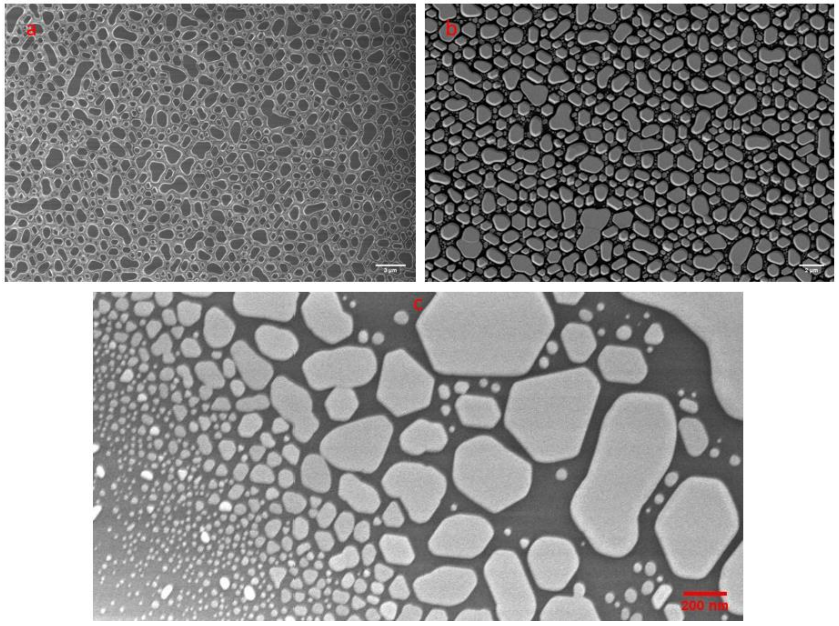

Figure 2.13 An overview of Au islands on polished sapphire substrate. (a) scale bar is 3µm. (b) scale bar is 2µm. (c) close up to smaller islands in between the larger ones, scale bar is 200nm. SEM images.

On the other hand, the surface of rough sapphire is an assembly of different sapphire surface plans. Therefore different interfaces and orientation relationships between Au and sapphire are formed. This leads to the observations, that on rough sapphire Au shows consistently crystal shapes similar, as discussed in the introduction. In addition to more defined Wulff construction related shapes, we can also see the NW growth. Although NW growth compared to as rolled Mo substrate does not show dense clustered areas, NW formation happens in the areas characterized by surface irregularities (Figure 2.12b, Figure 2.14). The observed NWs size (various diameter and length) is consistent with the distribution of NWs sizes on the original Mo substrates.

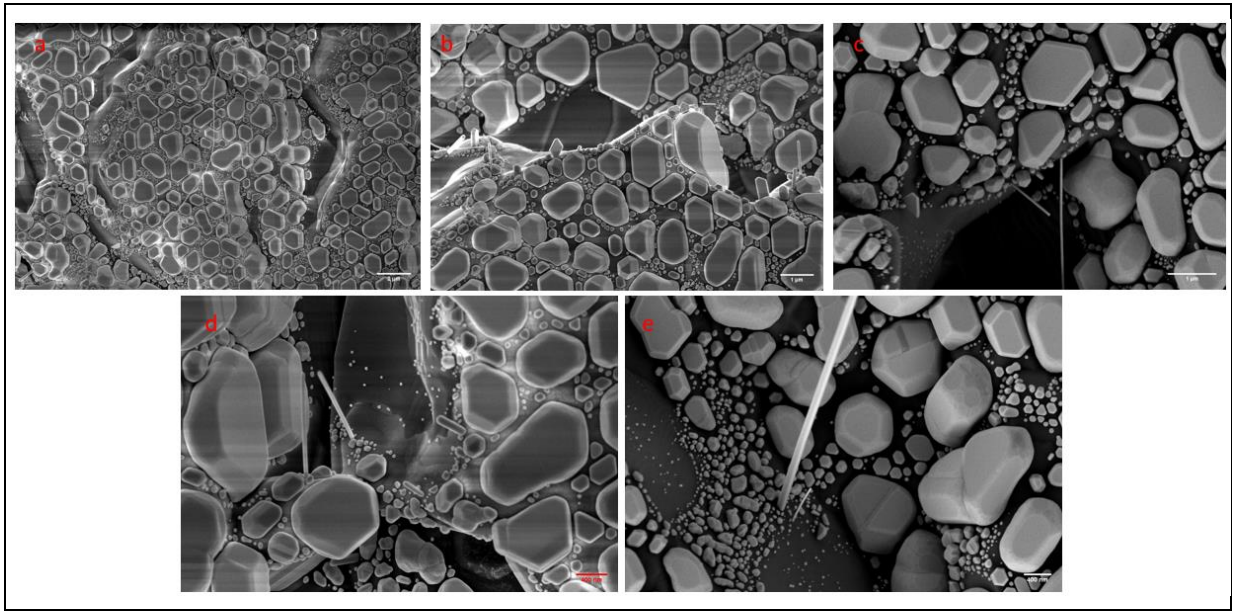

Figure 2.14 Au deposition on rough sapphire substrates. (a) Surface irregularities alongside with a long NW, scale bar is 4µm. (b) Short NWs at the edge of a microcrack step, scale bar is 1µm. (c) Longer NWs at the edge of another microcrack, scale bar is 1µm. (d-e) closer look at the roots of various sized NWs, scale bars are 400nm. SEM images

In the context of surface irregularities affecting NW growth, Boston *et.al.* observed the metal oxide NW growth *in –situ* using TEM. On the basis of direct observation, they suggested that rough surface of the porous matrix act as microcrucibles and thus provide insights into the mechanisms that drive metal oxide NW growth at high temperatures [64]. The morphologies of the NWs growth – time intervals (see Section 2.1.2) and crystal structure observed in this work are similar to the NWs observed by Boston et al. (Figure 2.15).

On polished Mo substrates we see the NW growth on and close to microcracks (Figure 2.12d, Figure 2.16). Density of the NWs is less than on as-rolled Mo substrates and again the sizes of the NWs are various.

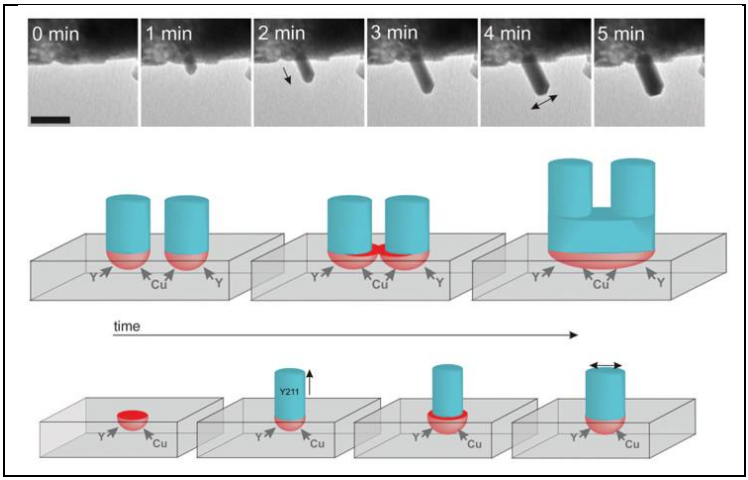

Figure 2.15 NW growth and expansion via microcrucibles (TEM images) and schematic illustrations. [64]

On the polished Mo substrate we can also observe the NW rich areas, which were clearly visible on as-rolled Mo substrate, but here they are barely visible. These NW rich areas are scarce on the surface, they can be found close to cracks with NPs and NWs (Figure 2.17).

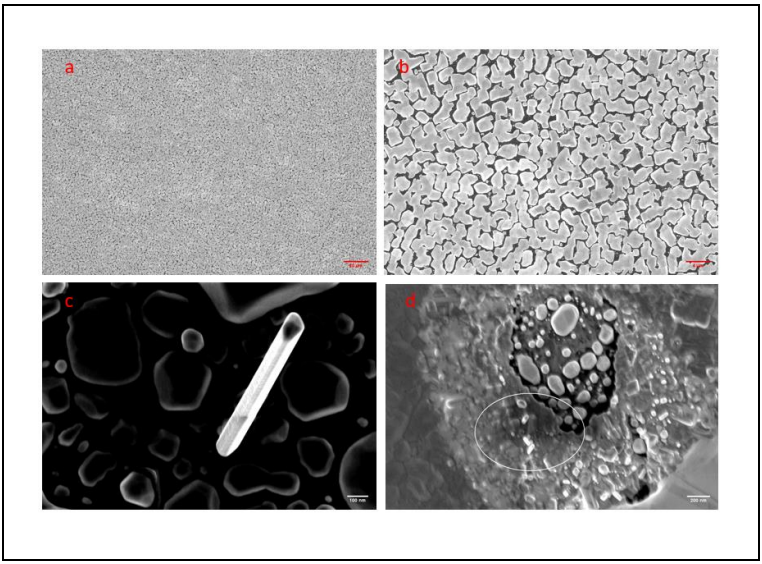

Figure 2.16 Au deposition on polished Mo substrates. (a-b) General formation of Au islands, scale bars are 20µm and 4µm respectively. (c) NW growth, scale bar is 100nm. (d) Start of e NW growth in the vicinity of a microcrack, scale bar is 200nm. SEM images.

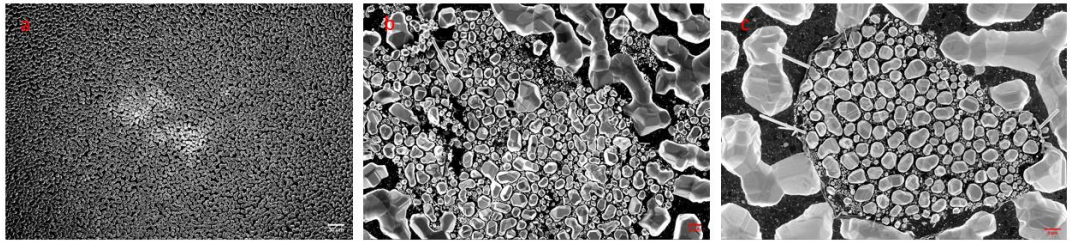

Figure 2.17 Closer look at Au NPs and NW rich areas on polished Mo substrate. (a) Overview of shiny cluster zone, scale bar is 20µm. (b) and (c) close up to the NP/NW cluster, scale bars are 2µm. SEM images

2.2.1 Effect of polycrystallinity

The polycrystallinity of the Mo substrate has an effect on NW density and structure of islands. XRD measurements on both as-rolled and polished substrates before and after Au deposition shows the correlation in between Mo grain orientations and Au islands (Figure 2.18). The result of XRD measurements raises other two questions: do the grains have an effect on growth of NW? If they have, how dominant are grains on creating large number of free standing NWs?

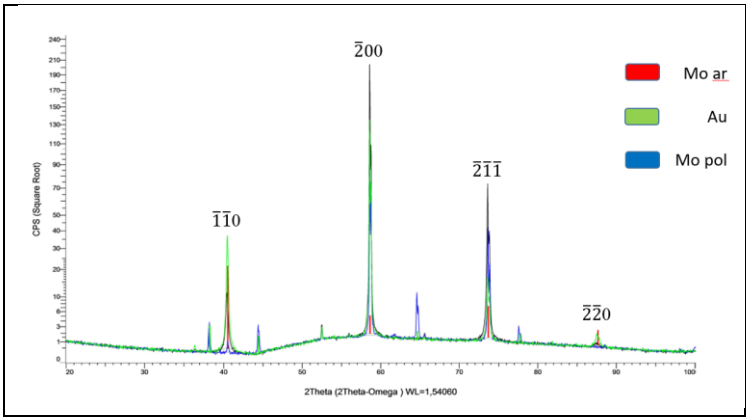

Figure 2.18 XRD peaks of Mo substrates before and after Au deposition. Peaks complement each other.

It is clear that the fit visible from XRD measurements comes from the same orientation of grain (Mo) and island (Au). Figure 2.2 and Figure 2.3 give the impression that NWs and NPs, and eventually islands, are placed randomly over the substrate. This is partially true for this case, since we saw that surface irregularities play a big role on growth of NWs and NPs and

these irregularities are randomly distributed over the surface. However, we see the starting point of nucleation in Figure 2.19 after 1 to 3 minutes of deposition, which is not randomly distributed but starts selectively in grain boundaries. According the explanations in Chapter 1, ones nucleated the crystal growth follow different growth paths, which causes the variety on our samples.

The number of NWs per substrate area is higher on as-rolled Mo substrates compared to rough sapphire under the same growth parameters, macroscopic surface energy and activation conditions (susbtrate temperature and deposition time). The only difference between these substrates is the crystallinity. At the last part of this section we will focus on how the polycrystalline grain structure is contributing to the NW growth.

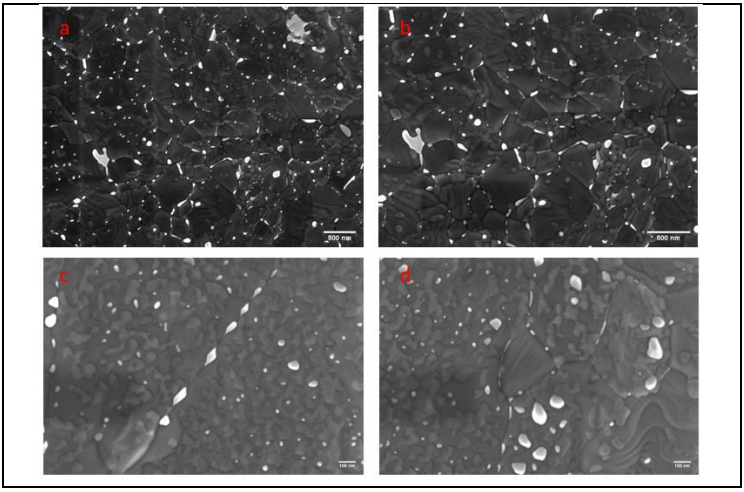

Figure 2.19 Mo grains and grain boundaries as selective areas for Au for nucleation. (a-b), scale bars are 500nm, (c-d) closer look at the grain boundaries, scale bars are 100nm. SEM images.

As defined above, NWs are originating from NPs, which follow the Wulff related constructions. Crystals follow the thermodynamic growth paths discussed in Chapter 1. Three elements contribute to the total energy of a crystal supported on a lattice mismatched substrate: the formation energy, the surface-interface energy, and the strain energy due to the lattice mismatch. Lattice mismatch strain is one of the driving forces for the crystal to increase in height. This increase is strongly affected by the substrate.

Chen *et al.* discussed the NP increase in height due lattice mismatch in details using different sizes of $SrTiO_3$ substrates and Au targets. The lattice mismatch and the crystal structure of $SrTiO_3$ are similar (3.2Å for Mo and 3.9Å for $SrTiO_3$) to the reference system used in this work. The authors also discussed strain relaxation realized via an edge dislocation introduction to the interface (Figure 2.20) [63]. On the other hand, for the NW case strain is an important driving force.

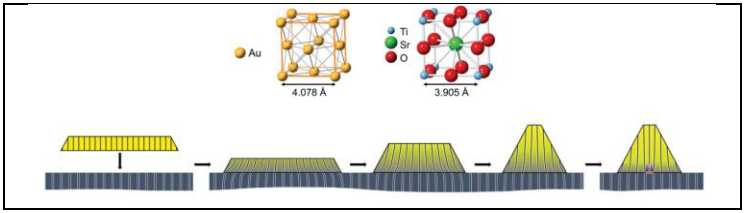

Figure 2.20 Lattice parameters, lattice mismatch strain and increase in crystal height. [65]

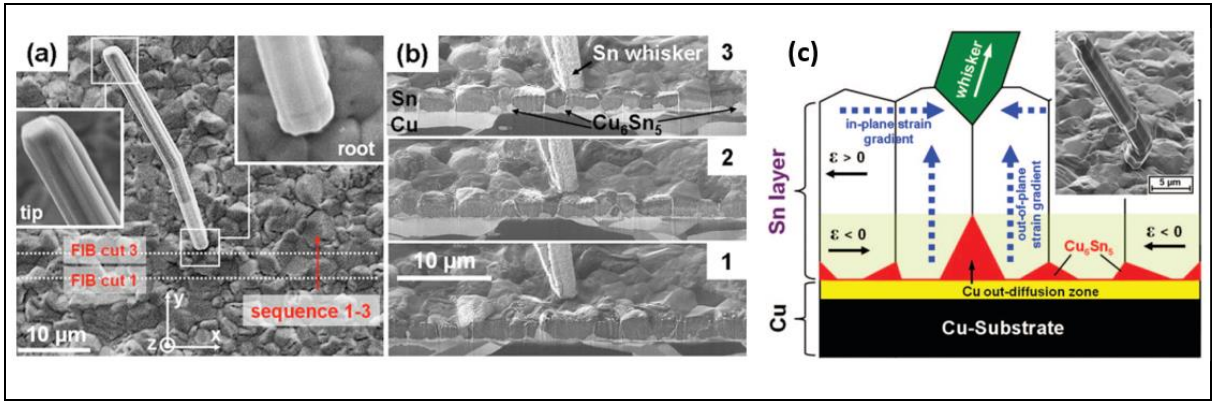

Figure 2.21 (a) SEM images of Sn NW and its surroundings. (b) FIB prepared interface. (c) Growth morphology and schematic model of the NW formation process in Sn thin films. [66]

Sobiech *et al.* showed that local, submicron strain gradients are the cause of spontaneous formation and growth of Sn whiskers [66]. Resemblance between NW formation in this work and Figure 2.21a is immense. This brings us the first observation: shiny, NW rich areas on our as-rolled Mo substrate. Plastic deformation of the metals is one of the most strain forming methods out there and cold rolling Mo down to 0.4mm thickness has its toll. We observe this on the elongation of the grains and channels on the substrate surface (section 2.2). When we mechanically introduce strain to our substrates NW rich areas significantly increase. Mechanically introducing strain to substrates affects the growth of nanowires (NWs) by altering the surface morphology of the substrate. Strain can be introduced through various methods such as bending, twisting, or compressing the substrate. The introduction of strain can also cause changes in the lattice constant and surface energy of the substrate, which in turn can affect the nucleation and growth of NWs. In particular, the introduction of strain can lead to the formation of NW-rich areas on the substrate surface. This is because the strain can create localized areas of increased surface energy, which promotes growth of NWs in those regions in similar fashion of Sobiech's work.

Overall, the introduction of strain can be a useful technique for controlling the growth of NWs on substrates and creating localized regions of high NW density.

Samples shown in Figure 2.22a-b were mechanically bended perpendicular to the rolling direction and in Figure 2.22c, they were bended parallel to the rolling direction. In addition, in Figure 2.22c we can observe that some channels started deforming and sheared along the rolling direction for the

parallel bent substrate. Samples that were bended perpendicular to rolling direction show a great increase of NW rich zones.

Strain effect explains the NW number difference that we see in between Mo substrates and sapphire substrates (no strain).

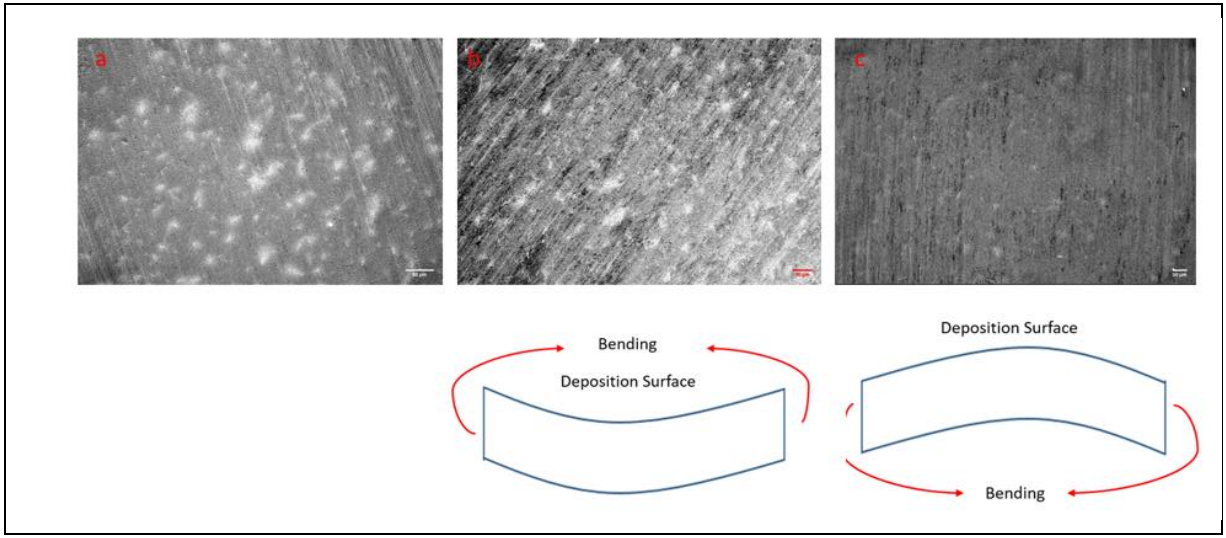

Figure 2.22 NW rich areas on strained substrates. (a-b) Samples mechanically bended perpendicular to the rolling direction, scale bars are 50 and 30µm respectively. (c) Samples bended parallel to the rolling direction, which decreases the number of NW rich areas, scale bar is 30µm.

2.3 Results, summary and discussion

In this chapter we discuss our hypothesis on NW growth. The most peculiar observation is, that micro level surface irregularities are necessary for the NW growth. If the substrate surface is homogeneous, then we do not have NWs growth but only islands form. We can ask what is the role of the surface irregularities? The nucleation rate in thin film growth is mainly governed by the activation energies of diffusion and adsorption [67]. If those energies are not invariant to translation, sites with higher nucleation rate will form the first nuclei. Then, subsequently random, statistical nucleation is followed on homogeneous substrate surface areas. The later nucleation leads to the growth of equiaxed island/particles. Whereas initially, probably at in the assumed holes/irregularities, the NWs and NPs are nucleated. The assumed situation for polycrystalline Mo is sketched in figure 2.23. The first function of the roughness on Mo as-rolled substrate is, to provide preferred nucleation sites for NW and NP growth, indicated as a hole in Figure 2.23a. Secondly, it it surrounding has allows for enhanced surface diffusion. Both are functions are similar to the thin C layer for the already published growth of Au, Ag or Cu NW [28].

The nucleation site has to allow for the transformation of a NP ito a NW. We assume that the interface between nucleated NP and substrate is responsible for NW formation. Two Au adatom diffusion paths can be envisioned to transport atoms into the interface. The first would be grain boundary diffusion and then outward diffusion of Au into the NP/Mo interface from the

depth of the polycrystal. The second is surface diffusion and the inward atom diffusion into the interface from the surface. Both will lead to the formation of at the same time a supersaturated zone for Au nucleus to form (Figure 2.23b). The diffusion of Au atoms into the interface by both paths requires a high density of vacancies. This density is probably the selection mechanism which allows the transformation of NPs to NWs. At places where nucleation occurs later, or the density of interface vacancies is low, Au islands forms an epitaxial orientation relationship with Mo grains (XRD).

After the nucleation of Au NPs and its transformation into a NW, the axial and radial growth of the whiskers has to be considered (Figure 2.23c), Ruth and Hirth [64] studied the sources of adatoms contributing to the axial growth of whiskers. Following their arguments, the source of Au adatoms is twofold: Au atoms condensate from the vapor phase either on the substrate surface and then diffuse to the whisker or impinge direct on the side facets of the whisker. Then adatoms from both sources diffuse to the incorporation site and contribute to the axial growth. Therefore, the axial growth of the NWs was mostly attributed to the aggregation of Au adatoms and diffusion of the atoms in the whisker-substrate interface. Since the growth occurs at the NW-substrate interface, it is called root growth mode. The incorporation of Au adatoms in the interface and it is kinetically much more effective compare to the radial growth process, resulting in the one-dimensional growth of the NWs. Radial growth can only occur by secondary nucleation on the side facets by the condensation and diffusion of Au adatoms on the whisker sidewalls together with the diffusion of Au atoms from the micro crucible towards the NW surface.

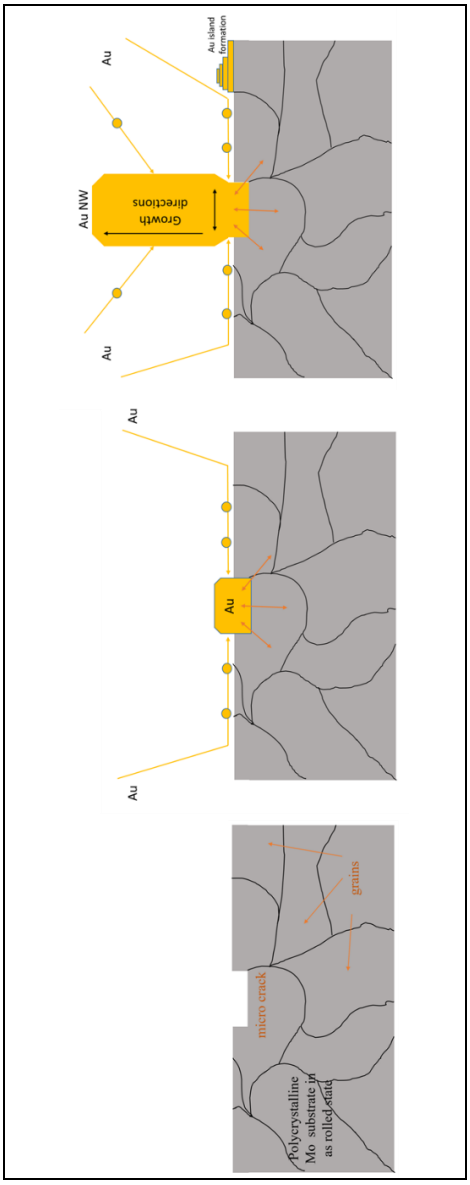

Figure 2.23 NW formation hypothesis schematic.

comparison of as-rolled Mo substrate and rough sapphire substrate has to be discussed, since only those substrate yield NWs. Two features are important: (i) similarities on (macroscopic) surface energy measurements and (ii) surface roughness. The first feature is directly related to the crystal constructions and atomic processes, which are largely discussed in the first chapter based on a significant number of research literature. The second feature, on the other hand, has less amount of literature back up related to NW growth, although it is theoretically and experimentally known that the surface irregularities are the selective nucleation sites for atoms during deposition [32, 33, 34, and 37].

These are the most important parameters to be able to obtain NWs using UHV-MBE system

- Substrate temperature, deposition rate and substrate material directly effecting NW growth:

Substrate temperature is one of the main parameters to obtain NWs via of the activation of surface diffusion. Higher surface diffusion rates create more nucleation zones. Another positive addition of high substrate temperature is keeping high-energy zones at the micro crucibles. With this said a constant material flow is another aspect of NW growth. Hence second main parameter can be defined is a constant deposition rate which is defined at a point to give the diffusing atoms time to find this high-energy zones. Last main parameter is the substrate material. Substrates, which has high surface energies, tend to have thin film structures rather than NPs or NWs. Here, by looking at the experiments done over different substrates we can

conclude that polycrystalline materials tend to have more NWs compared to single crystalline ones.

- Final morphology of the NWs is strongly depended on nucleated NPs growth path:

According to the discussions over nucleation and growth of a NPs and their crystal shapes (Chapter 1) we can observe the end morphology of NWs are identical even with the twins which is observed in many of the NWs. This also can be backed up with the cross section images we have in following section of this chapter. We can slice a NP out of a NW that will represent one of the kinetic shapes defined at chapter 1.

- Density (number of) the NWs in direct relation with the stress – strain over the substrate:

Strain presence not only backed up via mechanically adding stress over as-rolled substrates but also can explain the different NW density over polycrystalline Mo substrates compared to single crystalline sapphire ones.

With all above points “perfect NW growth” needs:

- Internal strain at the substrate material.
- Micro – level roughness on substrate surface.
- Optimized substrate temperature.
- Non-epitaxial growth

Having control on and understanding the growth helps optimizing the desired fabrication of the NWs. With the knowhow explained during previous sections, we obtained

structures of NWs, which might find application in various areas.

2.4 Other metallic nanowires

In this work, other metallic NW growth trials using as-rolled Mo substrates have been conducted. In this Section, the main results and current research are summarized. In previous works, carried out in the research group, Ag, Co, Ni NWs were grown. In this work, other target metal NWs (Cu, Pt and Mn) were successfully grown using the MBE (Figure 2.24). Parameter optimization is still ongoing.

Substrate temperatures for the NW growth were around 60% of the respective materials homologous melting temperatures, as discussed previously. For all the growth processes, deposition rate of 0.5Å/s is kept constant to have a comparative result with the Au NW experiments.

Cu NWs density was the highest. In addition, Cu NWs were the only one showing NPs characterized by Wulff like constructions. Experiments aiming to have consistent number of NWs per sample area over all metallic NWs are still continuing. Once the growth consistency is reached, extensive SEM and TEM characterizations will start to have the morphological comparison. Overall, first round of the growth experiments for every tested target metal (Cu, Pt and Mn) gave successful results without having any inconsistency with the theories we laid in this work about the growth mechanism.

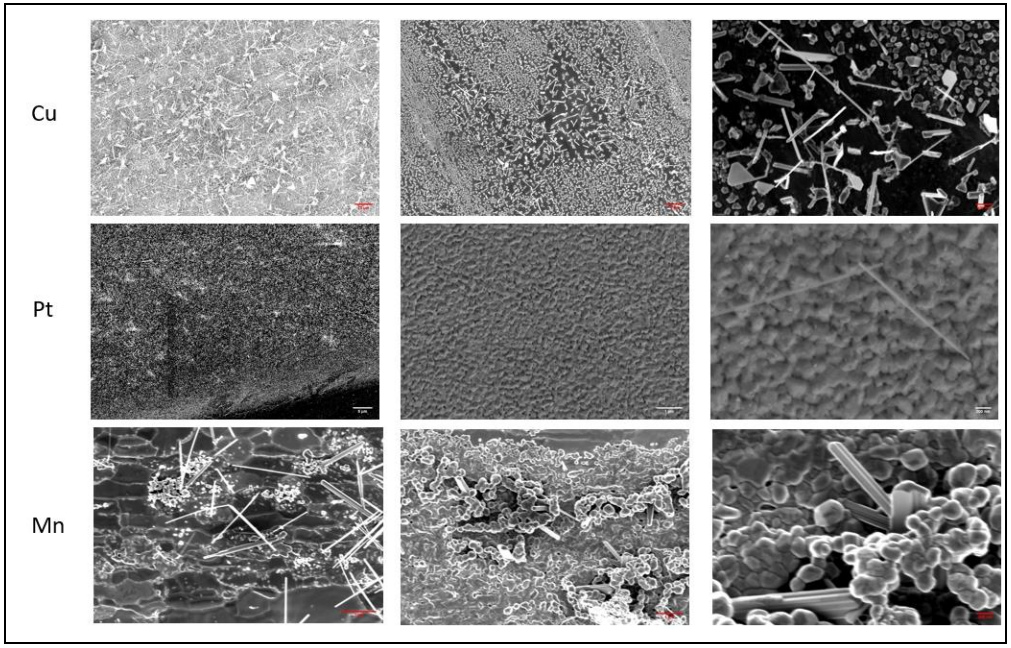

Figure 2.24 Cu, Pt and Mn NWs on as-rolled Mo substrate: Cu (left to right) scale bar is 10µm, 3µm, 400nm, Pt (left to right) scale bar is 5µm, 1µm, 200nm, Mn (left to right) scale bar is 1µm, 1µm, 200nm. SEM images

[1] Graham, T., Philos. Trans. Royal Soc. (1861).

[2] Zsigmondy, R., Justus Liebig Annalen der Chemie, 301 (1898).

[3] Barber, D., Freestone I.C, Archaeometry 32 (1990)

[4] Harden, D.B., Toynbee, J.M.C., Archaeologia 97 (1959).

[5] Webster, J., Metallographia or history of metals. 1671, London: Walter Kittelby.

[6] Agricola, G., De natura fossilium libri X. 1546, Chemnitz: VEB Deutscher Verlag der Wissenschaften.

[7] Ercker, L., Beschreibung allerfürnemisten Mineralischen Ertzt und Bergwercks arten, wie dieselbigen, unnd eine jene in Sonderheit der Natur und Eigenschafft nach, auff alle Metale Probirt. In fünf Bücher verfast. 1574, Prag: Georg Schwartz.

[8] Ostwald, W., Die Welt der vernachlässigten Dimensionen, Steinkopff Verlag, Dresden-Leipzig (1915).

[9] Bischof, G., Einige Bemerkungen über die Bildung der Gangmassen. Annalen der Physik Leipzig, (1843).

[10] Kohlschütter, V. Eydmann, E., Über Bildungsformen des Silbers. II) Das Haarsilber. Justus Liebigs Annalen Der Chemie, (1912).

[11] Friedrich, K., Leroux, A., Silber und Schwefelsilber. Metallurgie, (1906).

[12] Kohlschütter, H.W., Über den Mechanismus der Haarsilberbildung auf Silbersulfig. 5. Mitteilung über

topochemische Umsetzungen. Zeitschrift für Elektrochemie und angewandte physikalische Chemie, (1932).

[13] Brenner, S.S., The growth of whiskers by the reduction of metal salts. Acta Metallurgica, (1956).

[14] Brenner, S.S., Tensile strength of whiskers. Journal of Applied Physics, (1956).

[15] Brenner, S.S. and Sears, G.W., Mechanism of whisker growth. 3. Nature of growth sites. Acta Metallurgica, (1956).

[16] Brenner, S.S., Growth and properties of whiskers. Science, (1958).

[17] Brenner, S.S., Metal whiskers. Scientific American, (1960).

[18] McCray, W., MBE deserves a place in the history books. Nature Nanotech 2, (2007).

[19] Alferov, ZhI, Double heterostructure concept and its applications in physics, electronics and technology. Nobel lecture, http://nobelprize.org/nobel_prizes/physics/laureates/2000/alferov-lecture.html; 2000.

[20] Kroemer, H., Quasi-electric fields and band-offsets: teaching electrons new tricks. Nobel lecture, http://nobelprize.org/nobel_prizes/physics/laureates/2000/kroemer-lecture.html; 2000.

[21] Esaki, L., Long journey into tunneling. Nobel lecture, http://www.nobelprize.org/nobel_prizes/physics/laureates/1973/esaki-lecture.html; 1973.

[22] Von Klitzing, K., The quantized Hall Effect. Nobel lecture, http://www.nobelprize.org/nobel_prizes/physics/laureates/1985/klitzinglecture.html; 1985.

[23] Tsui, DC., Interplay of disorder and interaction in two-dimensional electron gas in intense magnetic fields. Nobel lecture, http://www.nobelprize.org/nobel_prizes/physics/laureates/1998/tsui-lecture.html; 1998.

[24] Störmer, HL., The fractional quantum hall effect. Nobel lecture, http://www.nobelprize.org/nobel_prizes/physics/laureates/1998/stormer-lecture.html; 1998.

[25] Richter, G., Hillerich, K., Gianola, D.S., Mönig, R., Kraft, O. and Volkert, C.A., Ultrahigh strength single crystalline nanowhiskers grown by physical vapor deposition. Nano Letters, (2009).

[26] Kolb, M. and Richter G., Growth of single crystalline copper nanowhiskers in: Stress-Induced Phenomena in Metallization Vol. 1300. (2010).

[27] Richter, G., Fabrication of freestanding gold nanotubes. Scripta Materialia, (2010).

[28] Schamel, M., Schopf, C., Linsler, D., Haag, S.T., Hofacker, L., Kappel, C., Strunk, H.P. and Richter, G., The filamentary growth of metals. International Journal of Materials Research, (2011).

[29] Bauer, E., Phänomenologische Theorie der Kristallabscheidung an Oberflächen. I. Zeitschrift für Kristallographie, (1958).

[30] Bauer, E., Phänomenologische Theorie der Kristallabscheidung an Oberflächen. II. Zeitschrift für Kristallographie, (1958).

[31] Venables, J.A., Rate equation approaches to thin-film nucleation kinetics. Philosophical Magazine, (1973).

[32] Frankl, D.R. and Venables, J.A., Nucleation on substrates from vapour phase. Advances in Physics, (1970).

[33] Ohring, M., Materials science of thin films, Academic press, (1992).

[34] Volmer, M. and Weber, A., Nucleus formation in oversaturated figures. Zeitschrift für Physikalische Chemie - Stöchiometrie und Verwandtschaftslehre, (1926).

[35] Venables, J.A., Introduction to Surface and Thin Film Processes, Cambridge University Press, (2003).

[36] Ratsch, C. and Venables, J. A., Nucleation theory and the early stages of thin film growth, Journal of Vacuum Science & Technology, (2003).

[37] Weissmayer, L., Keimbildung und Wachstum metallischer Whisker, Dissertation an der Universität Stuttgart, (2013).

[38] Gibbs J. W., The Collected Works of J. Willard Gibbs, edited by W. R. Longley and R. G. Van Name Yale University Press, New Haven, (1957).

[39] Curie P., Bull. Soc. Min. de France 8 (1885).

[40] Wulff G., Zur Frage der Geschwindigkeit des Wachstums und der Auflösung von Krystallflächen. (1901).

[41] Dinghas, A., ¨über einen Gcometrischen Satz von Wulff für die Gleichgewichtsform von Kristallen, Z. Kristallog. (1944).

[42] Herring, C., Some Theorems on the Free Energies of Crystal Surfaces, Phys. Rev. 82 (1951).

[43] Herring, C., The use of classical macroscopic concepts in surface energy problems, in: Structure and Properties of Solid Surfaces, edited by R. Gomer and C. S.Smith , University of Chicago Press, (1953).

[44] Burton, W. K., Cabrera, N. and F. C. Frank, The growth of crystals and the equilibrium structure of their surfaces, Phil. Trans. Roy. Soc. A, (1951).

[45] Sekerka, R. F., Theory of Crystal Growth Morphology, in: Crystal Growth - From Fundamentals to Technology, edited by G. Müller, J.J. Metois, and P. Rudolph (2004).

[46] Boukouvala, C., Daniel, J. & Ringe, E. Approaches to modelling the shape of nanocrystals. Nano Convergence 8, (2021).

[47] Frank, F. C., in Growth and Perfection of Crystals, edited by R. H. Doremus, B. W. Roberts, and D. Tumbull, (1958).

[48] Takayoshi Hayashi et al 1977 Jpn. J. Appl. Phys. 16 705, (1977).

[49] Marks, L. D. Modified Wulff Constructions for Twinned Particles. J. Cryst. Growth, (1983).

[50] Marks L. D. and Peng L., J. Phys.: Condens. Matter, (2016)

[51] Ino, S., Epitaxial growth of metals on rocksalt faces cleaved in vacuum.2. Orientation and structure of gold particles formed in ultrahigh vacuum J. Phys. Soc. Japan, (1966)

[52] Ino, S., Ogawa, S., Multiply Twinned Particles at Earlier Stages of Gold Film Formation on Alkalihalide Crystals. J. Phys. Soc. Jpn., (1967).

[53] Ino, S., Stability of Multiply-Twinned Particles. J. Phys. Soc. Jpn., (1969).

[54] Ringe, E., Van Duyne, R. P., Marks, L. D., Kinetic and Thermodynamic Modified Wulff Constructions for Twinned Nanoparticles. J. Phys. Chem., (2013).

[55] Winterbottom, W. L., Equilibrium shape of a small particle in contact with a foreign substrate Acta Metal., (1967).

[56] Akita, T., Kohyama, M. and Haruta, M. Acc. Chem. Res., (2013).

[57] Mansley, Z.R., Marks, L.D., J. Phys. Chem. C 124, (2020).

[58] Zucker, R.V., Chatain, D., Dahmen, U. et al. New software tools for the calculation and display of isolated and attached interfacial-energy minimizing particle shapes. J. Mater Sci., (2012).

[59] Hofmeister, H., From Nanoparticles to Nanorods and Nanowires, A. Vaseashta et al. (eds), Nanostructured and Advanced Materials (2005).

[60] Baletto F., Structural properties of sub-nanometer metallic clusters J. Phys. Condens. Matter., (2019).

[61] Massalski, T.B., Okamoto, H. Brewer, L. The Au – Mo System, Bulletin of Alloy Phase Diagrams, (1986).

[62] ASM Handbook Volume 14, Forming and Forging, Volume chair: S.L. Semiatin, ASM International, (1996).

[63] Melmed, A.J., Gomer, R., J. Chem. Phys. 34, (1960).

[64] Ruth, V., Hirth, J.P., J. Chem. Phys. 41, (1964) 3139.

[63] Fowkes, F. M., Attractive Forces at Interfaces. In: Industrial and Engineering Chemistry 56,12 (1964).

[64] Boston R., Schnepp Z., Nemoto Y., Sakka Y., Hall S.R., in Situ TEM Observation of a Microcrucible Mechanism of Nanowire Growth, Science 344, (2014).

[65] Chen P., Murugappan K., Castell M.R., Shapes of epitaxial gold nanocrystals on $SrTiO_3$ substrates, Phys. Chem. Chem. Phys., (2020).

[66] Sobiech M., Wohlschlögel M., Welzel U., Mittemeijer E.J., Hügel W., Seekamp A., Liu W., Ice G.E., Local, submicron, strain gradients as the cause of Sn whisker growth, Applied Physics Letters, (2009).

[67] Walton,D., Rhodin, T. R., Rollins, W., Nucleation of Silver on Sodium Chloride, (1963).

[68] Huang, W., Whiskers of IB, VIII Metals and Their Alloys: Synthesis and Microscopic Studies, Dissertation, Karlsruher Institut für Technologie (KIT), (2013).

[69] Handbook of Thin Film Technology, Ed. Maissel, L.I, Glang, R., McGraw Hill, (1983).

3. NANO - DIFFUSION

Diffusion in solids is a fundamental topic in materials science, solid-state physics, physical chemistry and physical metallurgy. The Latin word 'diffundere' means 'to spread out' [1], diffusion process can be defined as thermally stimulated random motion of atoms or molecules in gases, liquids and solids. Diffusion process related with the random motion of particles, this motion results in redistribution of particles moving from regions of high concentration to regions of low concentration. The diffusion is one of the best-understood topics in physics. However, research and understanding on nanoscale diffusion is not well understood especially when the diffusion couple has low- or non-vacancies.

The deviation of diffusion behavior at the nanoscale from what is known for bulk systems can be especially significant in the case of multiphase interdiffusion in solid-solid phase transformations and intermixing between multilayers. While in bulk diffusion couples the local thermodynamic equilibrium at the interphase boundaries in the interdiffusion zone is preserved, for the steep concentration gradients at the nanoscale the rate of atoms transfer across the interface can be comparable to the rate of diffusion-controlled removal of atoms from the interface zone. In this case, the compositions of the two phases at the interphase boundary will deviate from the equilibrium. The corresponding "interface-controlled kinetics" has been widely discussed in the context of solid-solid phase transformations, yet it has not been directly observed in nanoscale multiphase interdiffusion experiments. In this chapter using the Au-Fe bimetallic NW system, which we produced (see Chapter 2) a demonstration of nanoscale diffusion will be presented.

Here we demonstrate that nanoscale diffusion of Fe atoms in single crystalline, defect-free Au NWs is kinetically controlled by the Au-Fe interfaces mobility. Greater penetration depth of Fe into Au is observed at the interfaces with higher mobility, resulting in anisotropic intermixing in the cubic crystal (Au). This is the first experimental proof that the nanoscale multiphase interdiffusion is controlled by the interface mobility[60].

Fick's diffusion laws formulated more than 150 years ago and have been successfully employed for describing the mass transport in solids on macroscopic scale for more than a century. Recently, it has been demonstrated that the classical continuum approximation based on Fick's laws fails to describe diffusion at the nanoscale, when the concentration of the diffuser changes significantly over the length scales comparable to the interatomic distance. For example, Erdélyi et al. [2, 3] have demonstrated that diffusion intermixing at the nanoscale in the planar diffusion couples with strong diffusion asymmetry can lead to compositional sharpening, rather than broadening of the interfacial region. In another study, Haag et al. have employed coherent Bragg X-ray diffraction imaging to study the intermixing in heteroepitaxial single crystalline Au-Ag core-shell nanowhiskers (NWs) [4]. It was found that the Au-Ag intermixing in these NWs at elevated temperatures is significantly slower than predicted based on the literature data on interdiffusion in the bulk Au-Ag system. This slowdown of intermixing was interpreted in terms of scarcity of vacancy sources and increase of vacancy formation energy in perfect single crystals of small dimensions [4, 5].

The deviation of diffusion behavior at the nanoscale from what is known for bulk systems can be especially significant in the case of multiphase interdiffusion in solid-solid phase transformations and intermixing between multilayers. While in

bulk diffusion couples the local thermodynamic equilibrium at the interphase boundaries in the interdiffusion zone is usually preserved [6], for the steep concentration gradients at the nanoscale, the rate of atoms transfer across the interface can be comparable to the rate of diffusion-controlled removal of atoms from the interface zone. In this case, the compositions of the two phases contacting each other at the interphase boundary will deviate from the equilibrium. The corresponding "interface-controlled kinetics" has been widely discussed in the context of solid-solid phase transformations [7–10], yet it has rarely been directly observed in nanoscale multiphase interdiffusion experiments.

Aaronson and co-workers [11] considered the interface-controlled kinetics of interface migration about half a century ago. They observed that the overall thickening kinetics of plate-like precipitates (Widmanstätten microstructure) were much slower than allowed by volume diffusion of the solute. It was also hypothesized that the attachment of solute atoms to the wide coherent facets is associated with a high energy barrier [7, 8]. Therefore, it has been postulated that the sluggish heterophase interface migration kinetics is the reason for the limited diffusion of solute atoms to the precipitates. However, since no quantitative information on interface kinetics was available at the time, this interface-controlled phase transformation model could not be directly proved. We designed a unique experimental system the diffusion couples in the form of bimetallic NWs to study the influence of heterophase interface kinetics on nanoscale diffusion. It has been widely accepted that metallic NWs grown by molecular beam epitaxy (MBE) exhibit high crystalline quality and a scarcity of defects in the NW interior, and atomic-level flatness of the well-defined faceted surfaces. The absence of interior crystal lattice defects and surface ledges or steps are evidenced

by their high mechanical strengths approaching its upper theoretical limit [12–16].

This chapter will demonstrate that nanoscale diffusion of Fe atoms in single crystalline, defect-free Au NWs is kinetically controlled by the Au–Fe interfaces mobility. Greater penetration depth of Fe into Au is observed at the incoherent interfaces with higher mobility than that of their coherent counterparts, resulting in anisotropic intermixing in the cubic crystal (Au). This is a direct experimental proof that the nanoscale multiphase interdiffusion is controlled by the interface mobility.

3.1 Diffusion Experiments

3.1.1 Preparation, annealing and characterization of the nanowhiskers

The Au/Fe bimetallic NWs were prepared by physical vapor deposition onto Mo and W substrates using MBE, under a near-equilibrium growth condition. The Au NWs with a cross-section width of ~360nm and length of several micrometers were grown along < 011 > direction at 800 °C; followed by the deposition of Fe layers with a thickness of ~200 nm at room temperature. Both depositions were carried out in the same chamber without breaking the ultra-high vacuum of $5x10^{-10}$ mbar**.** The estimation of the NW diameter and Fe layer thickness was based on the reading of a quartz balance measuring the deposition rate. Rates were 0.05 nm/s and 0.01 nm/s for Au and Fe, respectively. The deposition angle of the Fe is 30° relative to the substrate normal. The topological features of the Fe layer varied depending on the inclination angle of the Au nanowhiskers. Moreover, due to the

shadowing effect, cavities in the Fe layers could form at the intersection of Au facets. The Au/Fe diffusion couple is chosen because these two metals do not form intermetallic compounds; Fe exhibits high solubility in Au, and little Au is soluble in Fe at the temperatures below 700 °C, so that the diffusion occurs only on the Au side of the diffusion couple [17]. It is worth noting that coherent twin boundary (TB) running parallel to the NW axis was found in some of Au NWs. Such twins are often observed in the NWs of face centered cubic metals with low stacking fault energy [18] , and they are known to have a negligible effect on diffusion [19].

The Au/Fe bimetallic NWs were harvested using an easy-lift system in a dual beam focused ion beam (FIB) - scanning electron microscope (SEM), (FEI Helios Nanolab Dualbeam G^3). Then they were mounted on Mo foil substrates using Pt deposition for further interdiffusion annealing experiments. Mo foils were used as substrates due to their high oxidation resistance, thermal conductivity, and strength [20]. The NWs can be cut into several segments for the comparison of the cross-section microstructures after different annealing treatments. To avoid Ga ion beam damage of the NWs, very low ion beam currents, short dwell time (50-100 nano seconds), and small pixel number (738 × 512 or 1536 × 1024) were used for imaging (30 kV, 1.1 pA) and cutting (30 kV; 7 pA), respectively.

Annealing treatments were conducted in a rapid thermal annealing furnace (RTA; ULVAC-RIKO MILA 50 0 0 P-N) under the reducing gas flow (Ar-10% H_2, 6N purity). A heating rate of 40 °C s^{-1} was used,

and fast cooling was performed by simply switching off the heating. To avoid contaminations, the Mo foil with mounted NW was placed on a sapphire plate, which in turn was placed on the quartz holder.

SEM characterization of the as-grown NWs was carried out in a Zeiss Ultra Plus high-resolution SEM. The in-lens mode operated at 4 keV was used for collecting the secondary electrons for imaging. The microstructure of the NWs and the composition profiles at the Au–Fe interfaces were examined in a scanning transmission electron microscope (STEM). The NW cross-section TEM lamellas were prepared by FIB using standard procedures. STEM was performed on a dual-C s - corrected Themis G^2 60–300, FEI/Thermo Fisher, operated at 300 kV. A 21 mrad beam convergence semi-angle was used and the resolution better than 0.9 Å was achieved. In high-angle annular dark-field (HAADF-) STEM imaging mode, the camera length was set to 94 mm, and gave an inner collection semi-angle of 119 mrad and an outer collection semi-angle of 200 mrad. The bright-field (BF) STEM images were also collected and in the semi-angle range of 0~11 mrad. Electron energy loss spectroscopy (EELS) spectra were acquired by a high-resolution energy filter system (Gatan Quantum ER965) with Dual-EELS. EELS was used instead of energy-dispersive X-ray spectroscopy (EDS) to eliminate the spurious and system-related Fe X-rays [21]; EELS also enables slightly better spatial resolution than EDS [22]. EEL spectra were recorded in the STEM mode with an entrance aperture size of 5 mm, a collection semi-angle of 57 mrad and an energy dispersion of 0.25 eV/channel. The energy resolution better than 1.5 eV was achieved. EEL spectra were recorded in the STEM mode with an entrance aperture size of 5mm, a collection semi-angle of 57 mrad and an energy dispersion of 0.25 eV/channel. The energy resolution better than 1.5 eV was achieved. Image-drift correction procedure was implemented in all EELS acquisitions. All the characterizations including STEM imaging and EELS mapping, were taken under an edge-on condition, with the < 011 > direction of Au crystal parallel to the optical axis. The thickness of the lamellas in the edge-on conditions, t ,

was controlled to keep the mean number of scattering events per incident electron, t / λ, in the range of 0.8~1.2. The absolute thickness of the lamellas was estimated to be in the range of 52~80 nm using the log-ratio method [23]. Since the Au $M_{4,5}$ -edges are located at high energies (2291 eV and 2206 eV, respectively), and because of the large energy separation (~1500 eV) between the Au $M_{4,5}$ -edges and the Fe $L_{2,3}$ -edges (at 721 eV and 708 eV, respectively), the quantitative information (such as Fe concentration in Au NWs), and the exact detection limit of Fe in Au cannot be estimated from the high-loss spectra with confidence. Therefore, we used a typical compositional sensitivity of 0.1 at% of EELS technique as the detection limit [24 , 25] . Geometric phase analysis (GPA) was performed on atomic resolution HAADF-STEM images using a free FRWR tools plugin for Digital Micrograph [26] based on the original work by Hÿtch et al. [27] . The ($\bar{1}$11) and (111) lattice reflections were used for the analysis, and Au lattice far away from the interface was used for the reference. Selected area diffraction patterns (SADPs) were taken on a FEI Tecnai T20 TEM operated at 200 kV.

3.2 Results of diffusion experiments

3.2.1 As grown Au/Fe NWs characterization

The closest packed {111} and second closest packed {100} planes of the FCC lattice form the side facets of Au NWs. The Fe layers deposited on the {100} and {111} facets were found to be single-crystalline (SX) and poly-crystalline (PX), respectively. Two representative as-grown bimetallic NWs with SX and PX Fe layers are presented in Figure 3.1. The SX Fe

layer on Au (100) facet has a relatively smooth surface (Figure 3.1a), and exhibits a clear Bain orientation relationship with Au NW, e.g.[0 $\bar{1}$1]Au//[001]Fe, (011)Au//(010)Fe and (10 0)Au//(10 0)Fe. The SX Fe-Au interface is without any misfit dislocations, as can be seen in the HAADF-STEM image (Figure 3.1e) and the geometrical phase analysis, see Figure 3.2. This is because the lattice mismatch between (011)Au//(010)Fe is only 0.59%, indicating the SX Fe-Au interfaces are coherent.

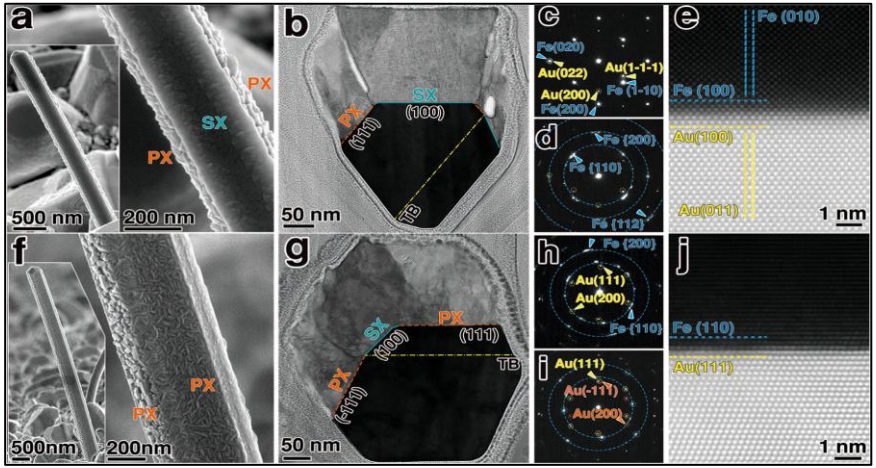

Figure 3.1 Au–Fe NWs with the single- and poly- crystalline Fe layers. SX Fe on Au (100) facet (a-e) and PX Fe on Au (111) facets (f-j). SEM (a, f) and BF-STEM cross-section micrographs acquired in the edge-on condition (b, g) demonstrate the smooth and rough surfaces of SX and PX Fe layers on Au {100} and {111} facets, respectively. SADPs demonstrate the orientation relationship between SX Fe and Au (c); for PX Fe and Au, diffuse diffraction streaks highlighted by arrows indicate low angle misorientation between Fe nanocrystals (d, h); a coherent twin boundary (TB) running parallel to the NW axis (i). Atomic-resolution HAADF-STEM images (e, j) demonstrate coherent SX and incoherent PX interfaces at the (100) Au and (111) Au facets,

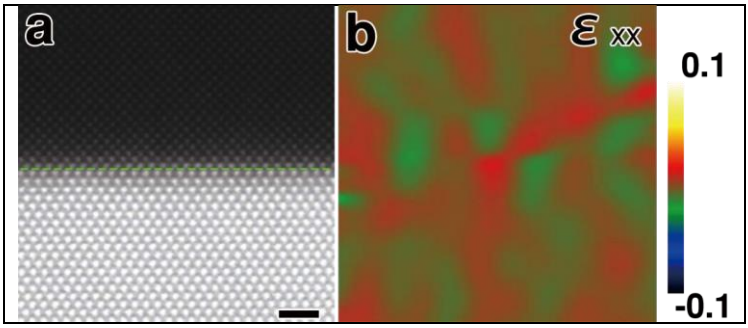

Figure 3.2 Coherent SX Fe – (100) Au interface in as-grown condition. Atomic resolution HAADF-STEM image (a) and the lattice strain εxx from GPA analysis (b) show that the SX coherent interface in as-grown condition possesses neither misfit dislocations nor disconnections. Scale bar indicates 1nm.

The PX Fe layer is composed of Fe nano-grains with low misorientation angles, as indicated by its rough surface (Figure 3.1f) and diffuse diffraction streaks in the diffraction patterns (Figure 3.1 d, h). Moreover, even though in some regions (110)Fe was found to be nearly parallel to (111)Au, neither Nishiyama-Wasserman ($[0\bar{1}1]$Au//[001]Fe) nor Kurdjumov-Sachs ($[0\bar{1}1]$Au//$[11\bar{1}]$Fe) orientation relationships were observed (Figure 1j). Therefore, we can conclude that the PX Fe-Au interfaces are of incoherent type. The fact that SX coherent interface and PX incoherent interface were formed on {100} and {111} Au facets, respectively, was possibly due to the energy of the coherent interface is significantly lower than that of its incoherent counterpart [28]. This resulted in Frank-van-der-Merwe growth of Fe on {100} facets, and in Volmer-Weber growth on {111} facets of Au NW [29].

3.2.2 Annealing treatments and diffusion measurements

The Au/Fe bimetallic NWs attached to Mo foil substrates were heat treated in an RTA furnace under the flow of forming gas, followed by fast cooling. During the isothermal diffusion, the Au-rich phase grew at the expense of Fe, and the Au–Fe interfaces moved in the Fe direction, due to high solubility of Fe in Au and negligible solubility of Au in Fe [17]. After heat treatments, the cross-sections of the NWs were prepared by FIB, and the atomic structure and chemical composition of Fe-Au interfaces were characterized by HAADF-STEM imaging and STEM- EELS mapping.

Figure 3.3 illustrates the penetration of Fe at both SX and PX Fe-Au interfaces in a typical NW. Here the penetration depth is defined as a distance between the Fe-Au interface and the site on the Au side of the interface where the Fe concentration decreases below the EELS detection limit (about 0.1 at.% of Fe, as indicated by the EELS edges of Fe disappearing in the background noise, Figure 3.3 b, d). It can be clearly seen that the penetration depth of Fe at SX interface after annealing at 350 °C for 30 min (4.8 ±0.8 nm) is much shallower than both the one at PX interface (13.0 ±1.0 nm), and the depth estimated based on bulk diffusivity of Fe atoms in Au. This is in a good agreement with the observations that both the thickening and lengthening of plate-shape precipitates occur at lower rates than those allowed by bulk diffusion [7]. The NWs annealed at 310, 330, 375, 400, 425, and 450°C also exhibit anisotropic intermixing, see Table 3.1 and Figures 3.4, 3.5. Finally, it should be noted that each investigated NW contained both the SX and PX interfaces, and thus the anisotropy of Fe penetration at the coherent and incoherent interfaces uncovered here represents an intrinsic property of each individual NW. This

eliminates the errors associated with measurements on different samples due to the variations of the experimental conditions.

Table 3.1 The annealing parameters, solubilities of Fe in Au, and estimated and measured Fe penetration depths at the coherent and incoherent interfaces. The errors in the penetration depth are one-half of the pixel sizes.

Annealing temperature (°C)	Heat treatment time (s)	Solubility of Fe in Au (at%)	Estimated* penetration depth of Fe in Au (nm)	Coherent interface penetration depth (nm)	Incoherent interface penetration depth (nm)
310	7200	11	15.0	2.6 ±0.3	6.7 ±0.8
330	3600	12.5	19.7	4.2 ±0.8	11.1 ±0.8
350	1800	14	24.8	4.8 ±0.8	13.0 ±1.0
375	900	16	34.3	6.0 ±0.5	14.0 ±1.5
400	720	17.7	57.0	11.1 ±1.0	22.2 ±1.0
425	480	19.6	82.9	16.9 ±1.3	26.0 ±2.0
450	300	21.4	111.0	25.1 ±1.0	36.2 ±3.0

* Arrhenius equation for bulk tracer diffusion of Fe into Au [30]: $D_{Fe/Au} = 8.2 \times 10^{-6}.exp\ (-174.2\ kJ \cdot mol^{-1}/RT)\ m^2/s$

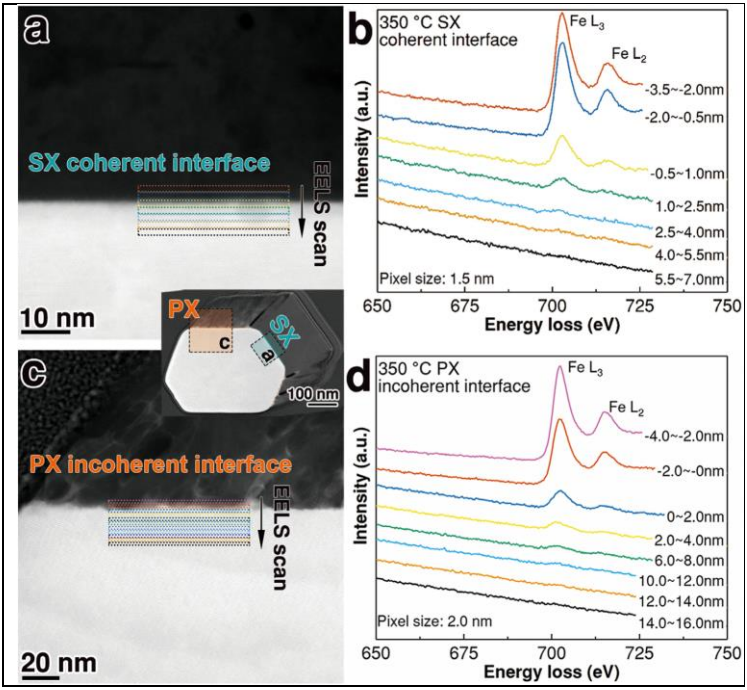

Figure 3.3 Anisotropic diffusional penetration of Fe into Au. EELS composition mappings at both coherent (a, b) and incoherent Fe-Au (c, d) interfaces in a NW that was heat treated at 350 °C for 30 min. The penetration depth of Fe at SX coherent interface and PX incoherent interface were 4.8 ±0.8 nm and 13.0 ±1.0 nm, respectively. The errors in penetration depth measurements result from the uncertainty of locating the site where Fe $L_{2,3}$ -edges disappear, and is estimated as one-half of the pixel size of the EELS map. Insert shows the cross-section overview and the EELS acquisition locations.

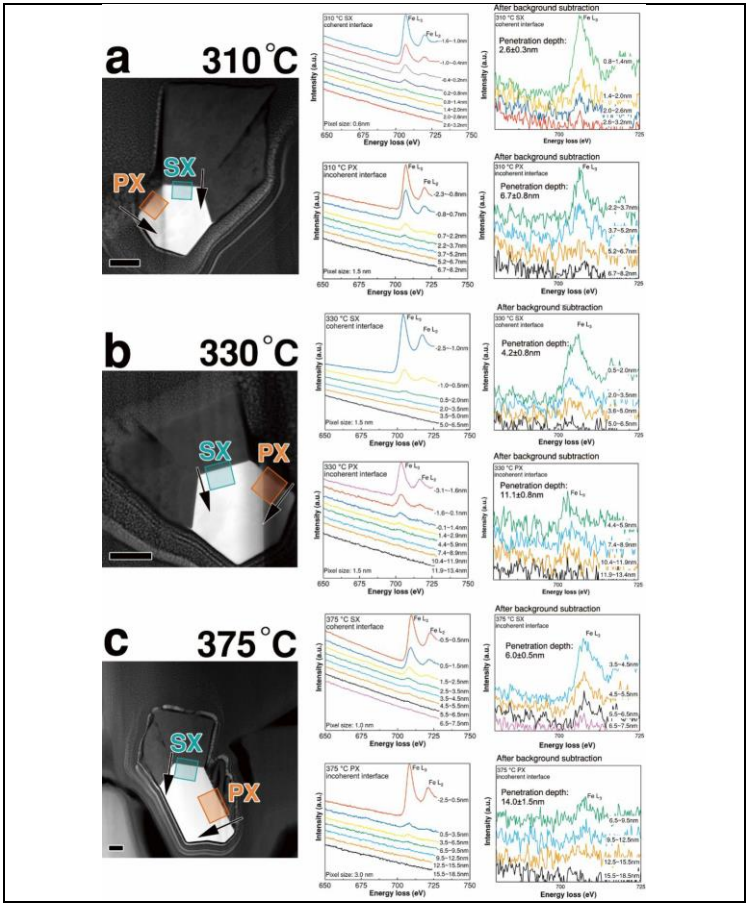

Figure 3.4 Anisotropic Fe penetration distance at Fe-Au interfaces. Samples annealed at 310 ºC for 120 min (a), 330 ºC for 60 min (b), and 375 ºC for 15 min (c). HAADF-STEM images showing the analyzed areas and the corresponding EELS spectra (before (middle column) and after (right column) background subtraction). The measurements of Fe distribution at the SX and PX interfaces at each temperature were performed in the same NW to avoid thickness differences. Scale bars indicate 50 nm.

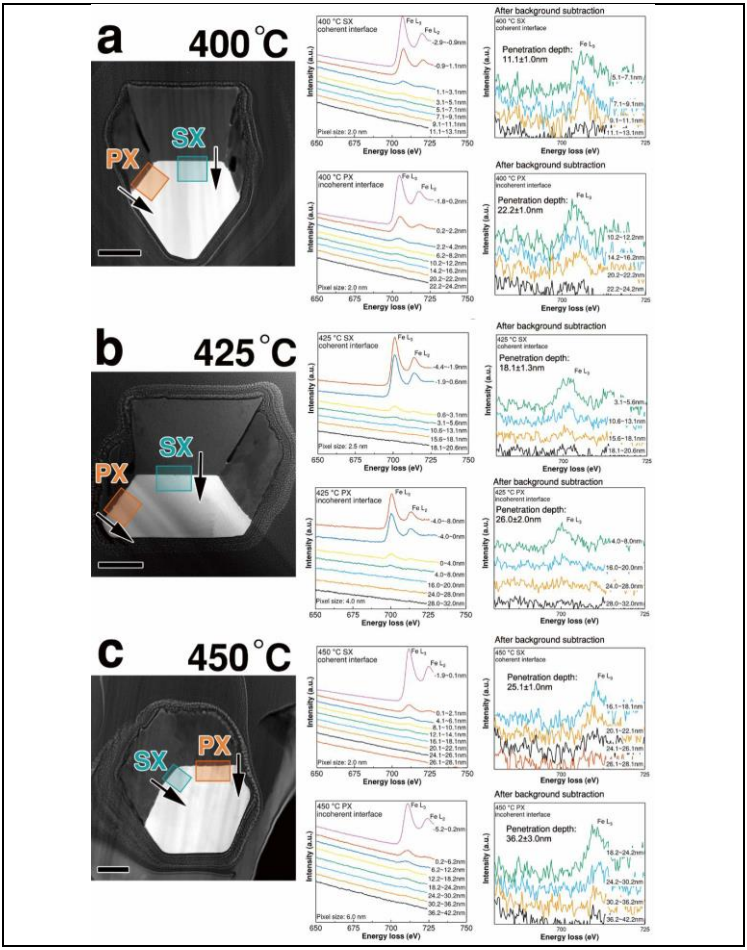

Figure 3.5 Anisotropic Fe penetration distance at Fe-Au interfaces. Samples annealed at 400 ºC for 12 min (a), 425 ºC for 8 min (b), and 450 ºC for 5 min (c). HAADF-STEM images showing the analyzed areas and the corresponding EEL spectra (before (middle column) and after (right column) background subtraction). The measurements of Fe distribution at the SX and PX interfaces at each temperature were performed in the same NW to avoid thickness differences. Scale bars indicate 100 nm.

3.3 Anisotropic diffusion

We would like to highlight that our direct observation of anisotropic diffusional penetration of Fe into a single crystalline defect-free Au nanowhisker is in apparent contradiction with a fundamental postulate of crystal physics - Neumann's principle [31]. This fundamental law of nature formulated more than a century ago states that for crystalline material, the symmetry of physical properties must include the symmetry elements of the point group of the material. This means that in cubic crystals (such as Au and Fe studied in our work) the diffusion is isotropic [32]. However, it is also important to emphasize that the Neumann principle does not consider interfaces or any other defects breaking crystal symmetry, and does not take into account possible interactions between the diffusing atoms. In this study, the apparent violation of Neumann's principle may be due to the difference in the atomic structures of the Fe-Au interfaces formed at the {100} Au and {111} Au facets and breaking the crystal symmetry. In the search of possible physical reasons for the observed diffusion anisotropy, we considered the following factors, which two of them can be safely excluded. i) the variation of vacancy concentration in the vicinity of the interfaces; ii) different magnitude of the coherency strain developed in the interdiffusion zone; iii) the anisotropy of interface mobility.

3.3.1 Differences of vacancy concentration in the vicinity of the interfaces

The structures created by annealing cubic nanocrystallites can be complex and usually have different interfaces. The first assumption is that the diffusion in direction of the incoherent

interface is more preferable because the concentration of thermal vacancies is higher. This is a reasonable statement, because coherent interfaces have high degree of order, which makes the formation of vacancies problematic [33]. To disprove this hypothesis let us use the *equation 4.1* to calculate the diffusion coefficient of vacancies.

$$\boldsymbol{D_{vac} = \frac{D}{f c_{vac}}} \qquad \textbf{Eq 4.1}$$

Here $\boldsymbol{D}$ is the self-diffusion coefficient, $\boldsymbol{f}$ is the correlation factor and $\boldsymbol{c_{vac}}$ is the mole fraction of the vacancies. Since, in this work the gold iron diffusion is investigated, let us calculate the diffusion coefficient of vacancies for the gold. The diffusion coefficient of the gold can be found in the following way [34]:

$$\boldsymbol{D_{vac} = D = (0.091 + 0.001) e^{\frac{41700+300}{RT}} \frac{cm^2}{sec}}$$

$$\textbf{Eq 4.2}$$

The self-diffusion coefficient in Au is $f \approx 0.7815$ [6]. The mole fraction of the vacancies $\boldsymbol{c_{vac}}$ is calculated considering that the vacancy formation energy for gold is $E_v \approx 0.97eV$ [35]. Similar to the one-dimension diffusion, the mean squared displacement of particles can be calculated using Equation 4.3.

$$\boldsymbol{MSD = 2\sqrt{D_{vac} t}} \qquad \textbf{Eq 4.3}$$

Therefore, for annealing at 350°C for 30 minutes the mean squared displacement is 146 micrometers. This means that a single source of vacancies at the PX Fe-Au interface can ensure the homogeneous distribution of vacancies through the NW, and the anisotropy of diffusion cannot be caused by the local variation of vacancy concentration.

3.3.2 Differences of the coherency strains developed in the interdiffusion zone

Let's look whether the anisotropy of coherency strains developing in the interdiffusion zone can cause the observed anisotropy of Fe penetration in the Au NW These strains arise due to the strong dependence of the lattice parameter of the Au–Fe solid solution on composition, and high elastic anisotropy of Au single crystals. By neglecting the non-liner contribution of the gradient terms, the diffusion coefficient in the presence of compositional coherency strain, D_v', is renormalized according to the relationship proposed by J.W. Cahn:

$$\boldsymbol{D_v' = D_v\left(1 + \frac{2\eta^2 Y_{hkl}}{\frac{\partial^2 G}{\partial c^2}}\right)} \qquad \textit{Eq 4.4}$$

where $\boldsymbol{\eta}$ and $\boldsymbol{Y_{hkl}}$ are the linear expansion per unit composition change and biaxial elastic modulus in the < *hkl* > direction, respectively. $\boldsymbol{G}$ is the Gibbs free energy of the alloy of composition c, and it will be approximated here by the expression for ideal solid solutions. The biaxial moduli calculated employing Cahn's relationships for cubic crystals [36, 37] and elastic constants of Au are $Y_{100} \approx 78.7$GPa and $Y_{111} \approx 190$ GPa. With the parameter, $\eta \approx -0.054$ estimated from the X-ray data on lattice parameters of the Au–Fe solid solutions [38], the equation 4.4 yields the re-normalization factors of 1.263 and 1.11 for the diffusion at the PX Fe-{111} Au and SX Fe-{100} Au interfaces, respectively, at the temperature of 350 °C. This difference of diffusivities, though in qualitative agreement with our experimental observations, would result in the difference of only 7% of the penetration depths, much smaller than the difference of a factor of around four measured in the

experiment. Moreover, the conditions of thermodynamic equilibrium change in the presence of coherency strain, and the solubility of Fe in Au is expected to be lower than the equilibrium solubility determined from the Fe-Au phase diagram [36]. This will increase the denominator in equation 4.4 and further reduce the strain-induced anisotropy of diffusivity.

Based on the above estimates, we safely excluded two possible reasons for causing the anisotropic Fe penetration: i) the deviations of vacancy concentration in the vicinity of the interfaces from its equilibrium value; ii) the anisotropy of coherency strains developing in the interdiffusion zone. The only remaining physical reason for the intermixing anisotropy is the limited mobility of the coherent SX Fe-{100} Au interface. To demonstrate the higher mobility of the incoherent Au interfaces as compared to their coherent Au counterparts, one NW was heat treated at 700°C for 120 min. As can be seen in Figure 3.6b, the migration distance of SX interface (40~60 nm) is much shorter than that of PX interfaces (60–250 nm).

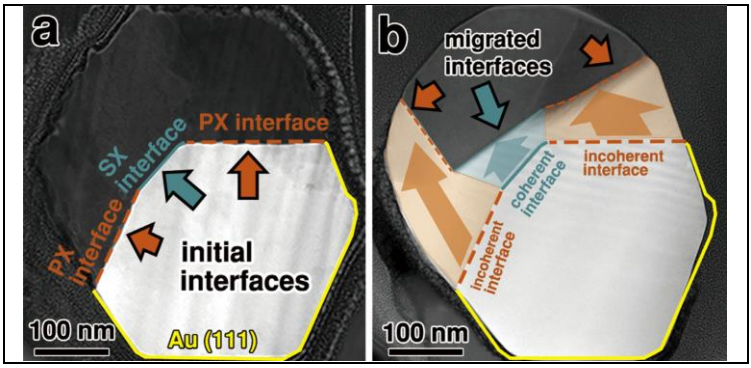

Figure 3.6 Anisotropic Au–Fe interface mobility demonstrated by interface migration distances. HAADF-STEM images showing the cross-section of a NW (a) before and (b) after annealing at 700°C for 120 min. The coherent SX Fe – {100}

Au interface migrated shorter distance than the two incoherent PX Fe – {111} Au interfaces.

3.3.3 Influence of Fe–Au interface mobility on Fe penetration

We developed a simple phenomenological model of interface-controlled intermixing in the Fe-Au diffusion couple. Let us consider a one-dimensional interdiffusion of two pure components A and B along the *x* -axis. Furthermore, to mimic the Fe-Au system, we will assume a finite solubility of B in A (C_{eq}), but zero solubility of A in B, where C stands for the mole fraction of B - atoms. Assuming that $x = X$ s is the position of the interphase boundary, the initial conditions can be formulated in the following way: $X_s = 0$, $C = C_B = 1$ for $x < X$ s and $C = 0$ for $x > X_s$. We will assume that the penetration of B in A, and thus the displacement of the interphase boundary is controlled by the finite boundary mobility:

$$\frac{dX_s}{dt} = \frac{Mkt}{\Omega} ln\left(\frac{C_{eq}}{C_s}\right) \qquad Eq\ 4.5$$

where M and Ω are the interface mobility and atomic volume, respectively, $kT\ ln(C_{eq}/C_s)$ is the thermodynamic driving force for interface migration, and C s is the concentration of *B* at the interface $C\ (x = X_s + , t) = C_s$, with $C_s < C_{eq}$). Here, we employed an ideal solution approximation for the solid solution of Fe in Au, with C_{eq} and C_s being the equilibrium solubility of Fe in Au and the actual mole fraction of Fe at the interface, respectively. Equation 4.5 should be complemented by the diffusion equation in the Au NW, and by Stefan's condition of the matter conservation at the interface. We will describe the A-

B interdiffusion in the Au NW by diffusion equation with concentration-independent interdiffusion coefficient, *D*:

$$\frac{\partial C}{\partial t} = D\frac{\partial^2 C}{\partial x^2}, \quad x > X_s \qquad \textit{Eq 4.6}$$

The concentration of B at the interface, C_s, can be calculated employing the condition of mass balance:

$$D\frac{\partial C}{\partial x}\Big|_{x=X_s} = (C_B - C_s)\frac{dX_s}{dt} \qquad \textit{Eq 4.7}$$

The Equations (4.5) – (4.7) fully describe the concentration profile of B in the A phase and the migration of the interphase boundary. They were solved numerically with the values of C_{eq} and *D* taken from Refs [17] and [30], respectively. The value of M was selected in a way resulting in penetration depth equal to the one observed in the experiment. The resulting values of M and of interface velocities are shown in Table 3.2. The value of Fe penetration depth for purely diffusion-controlled interface motion was obtained numerically by formally assigning a very large value to mobility *M* (Table 3.2).

Table 3.2. The annealing parameters, and calculated SX coherent and PX incoherent interface mobilities and velocities at various temperatures. The interface velocity and mobility estimations are based on the lower and upper bounds of penetration depths. The PX incoherent interfaces exhibit higher mobilities and velocities than their coherent counterparts

Annealing temperature (°C)	Coherent interface mobility (m^4/sJ)	Incoherent interface mobility (m^4/sJ)	Coherent interface velocity (nm/s)	Incoherent interface velocity (nm/s)
310	(6.7-8.0) • 10^{-25}	(3.2-5.3) • 10^{-24}	(3.2-3.8) • 10^{-7}	(1.5-2.5) • 10^{-6}
330	(2.1-2.8) • 10^{-24}	(1.4-2.6) • 10^{-23}	(1.0-1.3) • 10^{-6}	(7.0-13.0) • 10^{-6}
350	(4.3-5.9) • 10^{-24}	(2.7-6.7) • 10^{-23}	(2.2-3.0) • 10^{-6}	(1.3-3.4) • 10^{-5}
375	(1.2-1.4) • 10^{-23}	(2.7-7.8) • 10^{-23}	(6.2-7.2) • 10^{-6}	(1.4-4.1) • 10^{-5}
400	(2.6-2.9) • 10^{-23}	(8.2-11.9) • 10^{-23}	(1.4-1.6) • 10^{-5}	(4.5-6.5) • 10^{-5}
425	(5.6-6.7) • 10^{-23}	(1.0-1.4) • 10^{-22}	(3.2-3.8) • 10^{-5}	(5.7-8.1) • 10^{-5}
450	(1.3-1.5) • 10^{-22}	(2.4-3.2) • 10^{-22}	(7.9-8.7) • 10^{-5}	(1.4-1.9) • 10^{-4}

The temperature dependence of the interface mobilities calculated by fitting the experimentally measured Fe penetration depths in the range of temperatures between 310 and 450°C is shown in Figure 3.7. The dependence of the mobility on temperature follows Arrhenius' law, with the activation energies of 127.0 ±2 and 90.0 ±6 kJ/mol for the coherent and incoherent interfaces, respectively. The former is in a good agreement with the activation energy for the grain boundary migration in Au doped with 20 ppm of Fe, 128kJ/mol, measured at the temperatures below 290°C, when the migrating grain boundary drags the segregated Fe atoms [39]. This means that the atomistic mechanisms of interface migration are similar in both cases, and are controlled by an exchange of a Fe atom at the interface with a vacancy in Au. It is worth noting that at the lowest studied temperatures the mobility of coherent interface is by one order of magnitude lower than that of its incoherent counterpart.

The concentration profiles of Fe in the Au NW calculated in the framework of our model are presented in Figure 3.8a. It is remarkable that Fe concentration at the coherent Fe-{100} Au interface is significantly lower than the equilibrium solubility limit of Fe in Au, which changes from 11 at% to 21.4 at% in the temperature range of 310-450°C. This observation confirms that the coherent interface mobility is very low, and its movement is a kinetic "bottleneck" determining the rate of intermixing. To underline this point, we simulated the concentration profiles of Fe in Au at the temperature of 425°C for different values of mobility *M*, see Figure 3.8b.

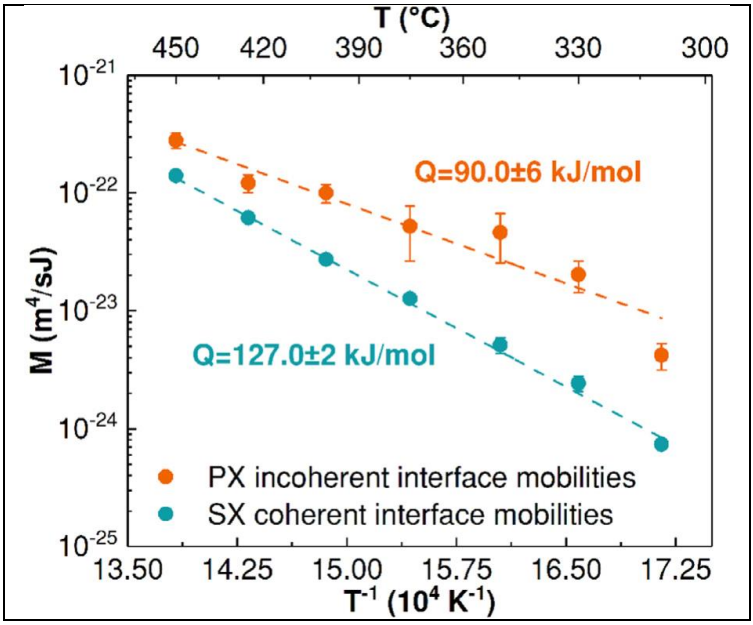

Figure 3.7 The Arrhenius plot of the coherent and incoherent Au–Fe interface mobilities. The error bars are determined based on the uncertainty in penetration depth measurements.

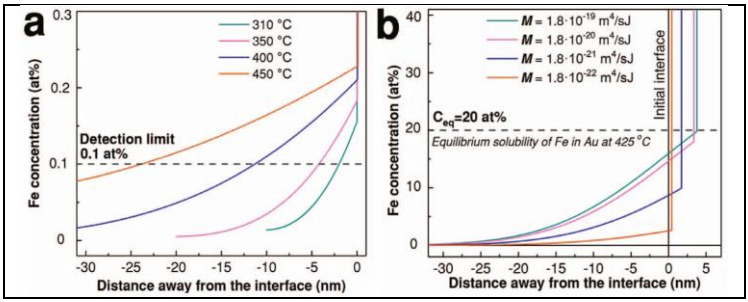

Figure 3.8 The influence of Au–Fe interface mobilities on Fe penetration depths. (a) Calculated Fe concentration profiles in Au NW at coherent interfaces at various temperatures. (b) Calculated Fe concentration profiles for various interface mobilities at the temperature of 425 °C.

One can see how the concentration of Fe at the interface increases and approaches the solubility limit with increasing *M*. Therefore, we conclude that the low mobility of SX coherent interface is the main kinetic factor that limits the diffusional penetration of Fe into Au.

It should be noted that low interface mobility results in non-parabolic (usually, mixed linear-parabolic) dependence of the interface displacement on annealing time. Such non-parabolic dependence was observed in experimental study of the dissolution of a PX Ni layer in the (111)-oriented single crystal of Au [40]. These experimental observations were discussed by *Erdélyi et al*. in terms of strong dependence of the chemical interdiffusion coefficient in the Ni-Au system on composition [41]. There is a deep conceptual similarity of our approach to interface-controlled diffusion outlined above, and the approach of Erdélyi et al. Indeed, in the model of Erdélyi et al., the atomic jump frequency in the interface region is very different from those in the rest of diffusion zone because of the combination of

steep concentration gradient and strong dependence of the diffusion coefficient on composition. Formally, this high difference in jump frequencies can be described by assigning the interface region its own mobility. For longer annealing times, as the concentration gradient in the interface region is reduced, the difference in jump frequencies decreases and interface movements can be again described by a parabolic law. The main difference between the works [2, 40, 41] and the present work is that the former have considered isostructural interfaces (either BCC/BCC [2] or FCC/FCC [40, 41]), while our work is focused on the heterostructural BCC/FCC interfaces. In the case of isostructural interfaces, a continuous description of the interface region in the spirit of Cahn-Hilliard "diffuse interface" model is legitimate, and distinct interface kinetics can be described in terms of strong concentration dependence of the interdiffusion coefficient in the whole range of concentrations (including those within the miscibility gap). In our case of heterostructural interface a continuous transition between the phases is impossible, and the interface can be well identified at the atomic resolution in STEM micrographs. Therefore, we treated the interface as a well defined planar object with its own mobility, *M*, and correlated this mobility with the atomic structure of the migrating interfaces.

3.3.4 Atomic structures of the migrating Fe–Au interfaces

The heterophase interfaces separating the phases of different composition migrate in a non-conservative manner, and their mobilities depend on the efficiency of sources/sinks located at the interface (shuffling between Fe atoms and Au vacancies) [10]. The anisotropy of interface mobility is directly associated with the atomic structure of the migrating interface. Compared

to the PX incoherent interface which developed stacking faults (SFs), TBs, and nanoscale roughness facilitating migration (Figure 3.7a), SX coherent interface remained nearly flat at 350°C and only developed steps at 425°C (Figure 3.7b) and 600°C, Figures 3.8 and 3.9 show the related results. Therefore, the motion of coherent interfaces is controlled by the nucleation and propagation of steps, which in most cases also possess the dislocation character. The latter is related to the mismatch of rigid body displacements of the two phases adjacent the interface on the two sides of the step. These linear defects having both a step and a dislocation character are referred to as disconnections [41, 42].

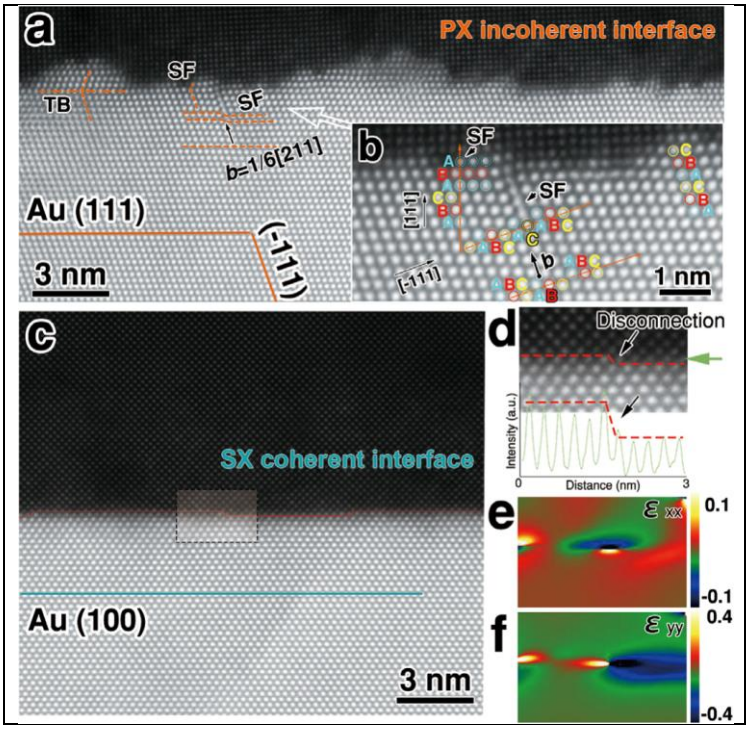

Figure 3.7 Atomic structure of the migrating incoherent and coherent Au–Fe interfaces after annealing at 425 °C for 8 min. Atomic resolution HAADF-STEM images showing (a) the development of growth stacking fault (SF) and TB, and nanoscale roughness at the PX incoherent interface after annealing; insert (b) highlights the growth SF parallel to $(111)_{Au}$ a Shockley partial dislocation 1/6[211] formed in the Au NW on $(\bar{1}11)_{Au}$ to relax the coherency strain and a cone-shaped protrusion formed with- out changing of the stacking sequence along $[111]_{Au}$; (c) the formation of disconnections on the SX coherent interface after annealing; red lines drawn along the interface highlight the disconnections; (d) the enlarged view of one selected disconnection and intensities along the interface plane (as indicated by green arrow), the sharp decrease of intensities from left to right indicates the change from Au-rich to Fe-rich composition and the location of the disconnection; the fluctuation of the intensities of Au-rich atom columns is due to kinks on these ledges (e, f) Geometric phase analysis of (d) showing the singularity of the strain field consistent with the singular strain field of the dislocation component of the disconnection.

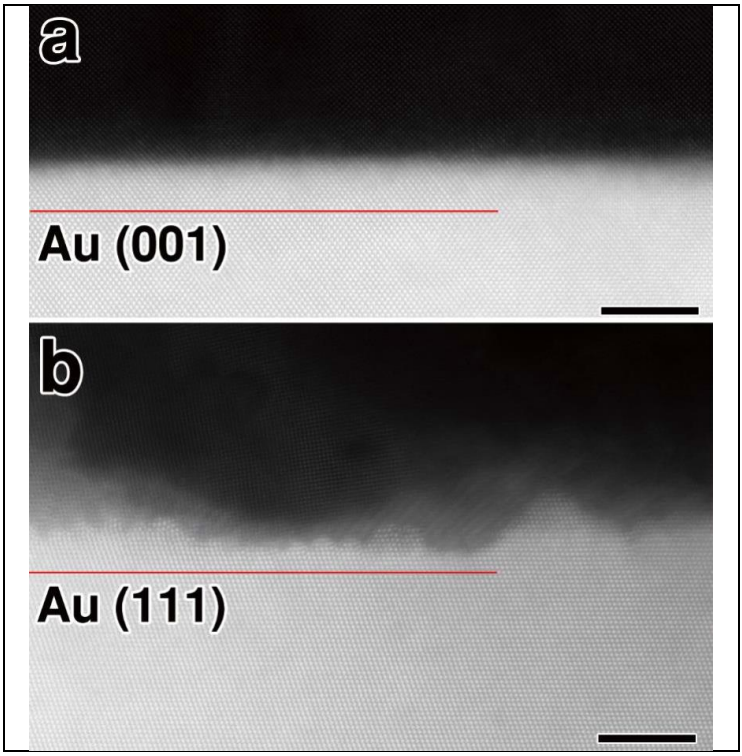

Figure 3.8 Coherent and incoherent interfaces after heat treatment at 350 °C for 30 min. Atomic resolution HAADF-STEM images showing that SX coherent interface remained flat, and that PX incoherent interface developed nanoscale roughness. This difference in atomic structures explains why the mobility of PX incoherent interfaces is higher than that of SX coherent interface. Scale bars are 5nm.

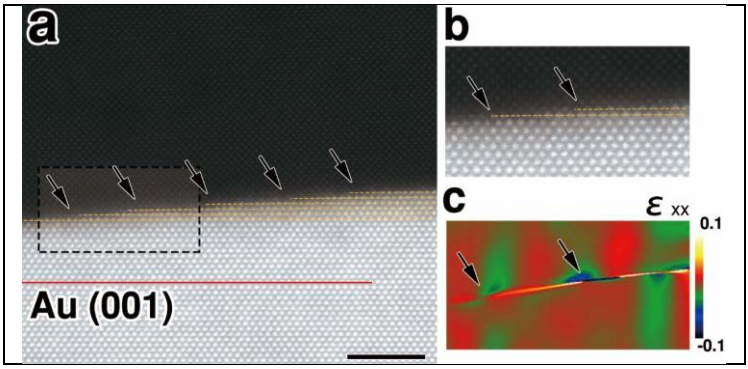

Figure 3.9 SX coherent interface migration at 600 ºC by formation of interface disconnections. (a) atomic resolution HAADF-STEM images showing SX coherent interface after annealing at 600 ºC for 7 min, yellow dashed lines highlight the Au (001) planes and black arrows point out where the Au (001) planes meet Fe (001) planes at the interface disconnections, (b) an enlarged view containing two disconnections and (c) the corresponding GPA analysis showing the strain field at the interface. Scale bar are 3nm.

We calculated the component of the Burgers vector of disconnection perpendicular to the interface.

The low mobility of SX coherent interface is the main kinetic factor that limits the diffusional penetration of Fe into Au. Compared to PX incoherent interfaces, which developed nanoscale roughness facilitating migration, SX coherent interface remained flat at low temperature (Figure 3.8) and developed multiple steps at relatively high temperatures such as 600 °C (Figure 3.9).

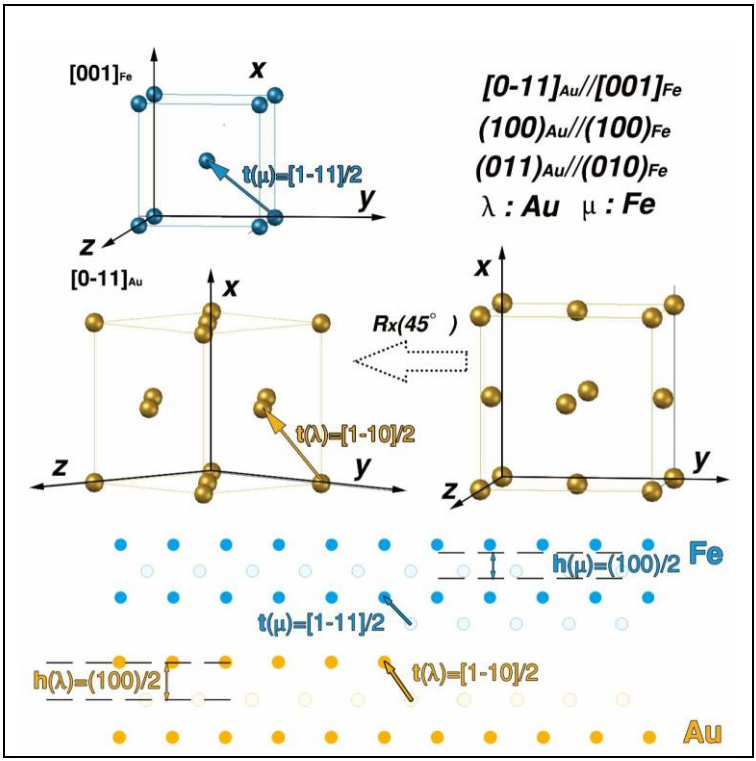

Figure 3.10 Illustration of the reference frame and the studied disconnection at the Fe-Au SX coherent interface. A rotation of 45˚ about z-axis was applied to convert a vector from Cartesian coordinates to λ (Au) crystal coordinates.

We analyzed one representative interfacial disconnection using the formalism developed by Pond and Hirth [43]. The Burgers vector of an interfacial line defect between two crystals, $\boldsymbol{\lambda}$ and $\boldsymbol{\mu}$, can be determined from: $\boldsymbol{b = t(\lambda) - Pt(\mu)}$, where $\boldsymbol{t(\lambda)}$ and $\boldsymbol{t(\mu)}$ are lattice translation vectors in the $\boldsymbol{\lambda}$ and $\boldsymbol{\mu}$ crystals, and $\boldsymbol{P}$ is the matrix that transforms a vector from the crystal coordinates of $\boldsymbol{\mu}$ to those of $\boldsymbol{\lambda}$. here, we consider Au and Fe as $\boldsymbol{\lambda}$ and $\boldsymbol{\mu}$, respectively. We define the Burgers vectors with respect to a reference frame in which the crystals are aligned with $[0\bar{1}1]_{Au}//[001]_{Fe}$, $(100)_{Au}//(100)_{Fe}$, and $(011)_{Au}//(010)_{Fe}$ and

strained into coherency (Figure 3.10). We consider a disconnection having a single atomic layer step height.

We used Medlin and Sugar's method to calculate the matrix ***P=LAM*** [44]. Here, ***M*** converts a vector from $\boldsymbol{\mu}$ (Fe) crystal coordinates to Cartesian coordinates, ***A*** operates in Cartesian coordinates to bring $\boldsymbol{\mu}$ and $\boldsymbol{\lambda}$ into coherency, i.e. the nearest-neighbor distances within the $\{100\}_{Au}$ and $\{100\}_{Fe}$ are strained into coherency ($r = \propto_{Au} / \sqrt{2 \propto_{Fe}} = 1.006$), and ***L*** converts a vector from Cartesian coordinates to $\boldsymbol{\lambda}$ (Au) crystal coordinates, which includes an anti-clockwise rotation of 45˚ about z axis (Figure 3.10)

$$\boldsymbol{L = R_x(45°).}\begin{pmatrix} \frac{1}{\alpha_{Au}} & 0 & 0 \\ 0 & \frac{1}{\alpha_{Au}} & 0 \\ 0 & 0 & \frac{1}{\alpha_{Au}} \end{pmatrix} = \begin{pmatrix} \frac{1}{\alpha_{Au}} & 0 & 0 \\ 0 & \frac{1}{\sqrt{2\alpha_{Au}}} & \frac{-1}{\sqrt{2\alpha_{Au}}} \\ 0 & \frac{1}{\sqrt{2\alpha_{Au}}} & \frac{1}{\alpha_{Au}} \end{pmatrix}$$

$$\boldsymbol{P = LAM}$$

$$= \begin{pmatrix} \frac{1}{\alpha_{Au}} & 0 & 0 \\ 0 & \frac{1}{\sqrt{2\alpha_{Au}}} & \frac{-1}{\sqrt{2\alpha_{Au}}} \\ 0 & \frac{1}{\sqrt{2\alpha_{Au}}} & \frac{1}{\alpha_{Au}} \end{pmatrix} . \begin{pmatrix} 1 & 0 & 0 \\ 0 & r & 0 \\ 0 & 0 & r \end{pmatrix} . \begin{pmatrix} \alpha_{Fe} & 0 & 0 \\ 0 & \alpha_{Fe} & 0 \\ 0 & 0 & \alpha_{Fe} \end{pmatrix}$$

$$= \begin{pmatrix} \frac{\alpha_{Fe}}{\alpha_{Au}} & 0 & 0 \\ 0 & \frac{1}{2} & -\frac{1}{2} \\ 0 & \frac{1}{2} & \frac{1}{2} \end{pmatrix}$$

The lattice translation vectors ***t(λ)*** of Au and ***t(μ)*** of Fe are $\frac{1}{2}[011]$ and $\frac{1}{2}[111]$, respectively.(Figure3.10)

The Burgers vector expressed relative to the Au crystal is:

$$\boldsymbol{b} = \boldsymbol{t}(\lambda) - \boldsymbol{P}\boldsymbol{t}(\mu) = \frac{\alpha_{Au}}{2}[1\bar{1}0] - \frac{\alpha_{Au}}{2}\begin{pmatrix} \frac{\alpha_{Fe}}{\alpha_{Au}} & 0 & 0 \\ 0 & \frac{1}{2} & -\frac{1}{2} \\ 0 & \frac{1}{2} & \frac{1}{2} \end{pmatrix}.[1\bar{1}1]$$

$$= \left(\frac{\alpha_{Au} - \alpha_{Fe}}{2}, 0, 0\right)$$

With $|\boldsymbol{b}| = 0.61$Å**.**

The component of the Burgers vector of disconnection perpendicular to the interface is:

$$\boldsymbol{b}_{\perp} = \frac{\alpha_{Au} - \alpha_{Fe}}{2}[100], |\boldsymbol{b}_{\perp}| = 0.61\text{Å}.$$

The activation energy for migration of the coherent interface can be associated with the nucleation energy of the critical disconnection loop [45]. The elastic energy contribution to the total energy of the loop scales as $\boldsymbol{b}^2$ and, therefore, relatively high amplitude of the determined Burgers vector is consistent with the high activation energy for interface mobility. Finally, it is worth noting that the critical temperature for disconnection nucleation at the coherent Fe-Au interface (~425 °C) is consistent with the fact that the thickening ledges on the broad

facets of precipitates in age hardenable Al- and Mg- alloys form only above a certain temperature threshold [46 , 47].

3.4 Conclusions

The anisotropy of interface mobility established in the present study sheds a new light on the development of highly anisotropic microstructures during heterogeneous solid-solid phase transformations. The best-known example of shape anisotropy of the second phase precipitates is the Widmanstätten microstructure that can be observed by the naked eye in the cross-sectioned Fe-Ni meteorites [48]. Similarly, highly anisotropic platelet-like precipitates of α-Fe have been observed during solid-solid phase transformations in the Au-based Au–Fe solid solutions [49–51]. Three factors were named as possible reasons for the shape anisotropy of the second phase precipitates: (i) the anisotropy of the matrix-precipitate interface energy; (ii) the shape-dependent elastic strains developing in the vicinity of the precipitate, and (iii) the anisotropic interface mobility [52–56]. With the quantitative data on interface mobilities lacking, all three factors were discussed on an equal footing. The atomistic and mesoscopic models of phase transformations taking into account only the former two factors consistently predicted less anisotropic precipitate shapes than those observed experimentally. The results of the present study clearly demonstrate that the anisotropy of interface mobility is the leading factor responsible for the growth of highly anisotropic precipitates, especially at relatively low annealing temperatures. Indeed, the density functional theory [28] and regular solution model [51] – based estimates of the energy of the coherent Fe-Au interface yield the values in the range of 0.36-0.5 J/m^2 . This relatively high value

can be attributed to the chemical component of the energy of Fe-Au bonds (scaling with the enthalpy of mixing in the Fe-Au solid solution). The energy of high angle non- special grain boundary in BCC Fe, 1.0 J/m2 [57], can be accepted as an upper bound for the energy of incoherent Fe-Au interface. Thus, the maximum anisotropy of the interface energy (factor of ~3) is significantly lower than that of the interface mobility (factor of ~10) and, hence, the latter is the most important factor determining the platelet morphology of α-Fe precipitates in the Au–Fe alloys.

In summary, we demonstrated that anisotropic penetration of Fe into defect-free, single crystalline Au nanowhiskers is caused by a much lower mobility of the coherent Fe-Au interface as compared to that of its incoherent counterpart. Our work provides a direct experimental evidence supporting theoretical models of multiphase interdiffusion with limited interphase boundary mobility [58, 59]. Moreover, even though it is commonly accepted that the coherent interfaces exhibit lower mobility than their incoherent counterparts, the quantitative data on absolute interface mobilities, and the ratios of coherent/incoherent interface mobilities were not available in the literature. Our data unambiguously showed that the incoherent Au–Fe interfaces exhibit up to one order of magnitude higher mobilities than their coherent counterparts. The sluggish migration of the coherent interface was associated with the difficulties in nucleation of the interface disconnections. The kinetic data of the type obtained in the present work are crucial to mesoscopic computer simulations of precipitate morphology evolution and interdiffusion in multilayers [52–54]. Finally, interdiffusion in bimetallic nanowhiskers can be employed to study the kinetics of a wide range of heterophase interfaces.

[1] Mehrer, H. ”Diffusion in Solids: Fundamentals, Methods, Materials, Diffusion-Controlled Processes” (2007) Berlin: Springer-Verlag.

[2] Erdélyi, Z., Sladecek, M., Stadler, L.M., Zizak, I., Langer, G.A., Kis-Varga, M. Beke, D.L, Sepiol, B., Transient interface sharpening in miscible alloys, Science 306 (2004).

[3] Erdélyi, Z., Beke, D.L., Nanoscale volume diffusion, J. Mater. Sci. 46 (2011).

[4] Haag, S.T., Richard, M.I., Welzel, U., Favre-Nicolin., Balmes, V.O., Richter, G., Mittemeijer, E.J., Thomas, O., Concentration and strain fields inside a Ag/Au core–shell nanowire studied by coherent X-ray diffraction, Nano. Lett. 13 (2013).

[5] Müller, M., Albe, K., Concentration of thermal vacancies in metallic nanoparticles, Acta. Mater. 55 (2007).

[6] Philibert, J.M., Atom movements-Diffusion and mass transport in solids, EDP Sci. (2012).

[7] Laird, C., Aaronson, H., The growth of γ plates in an Al-15% Ag alloy, Acta. Metall. 17 (1969).

[8] Laird, C., Aaronson, H., The dislocation structures of the broad faces of widmanstätten γ plates in an Al-15% Ag alloy, Acta. Metall. 15 (1967).

[9] Howe, J.M., Interfaces in Materials: Atomic Structure, Thermodynamics and Kinetics of Solid–Vapor, Solid–Liquid and Solid–Solid Interfaces, (1997).

[10] Sutton, A.P., Balluffi, R.W., Interfaces in Crystalline Materials, Oxford University Press, (1995).

[11] Aaronson, H., Decomposition of austenite by diffusional process, The Proeutectoid Ferrite and the Proeutectoid Cementite Reaction, (1962).

[12] Richter G., Hillerich, K., Gianola, D.S., Mönig, R., Kraft, O., Volkert, C.A., Ultrahigh strength single crystalline nanowhiskers grown by physical vapor deposition, Nano. Lett. (2009).

[13] Lee, S., Im J., Yoo Y., Bitzek E., Kiener, D., Richter G, Kim, B., Oh, S.H., Reversible cyclic deformation mechanism of gold nanowires by twinning–detwinning transition evidenced from in situ TEM, Nat. Commun., (2014).

[14] Roos, B., Kapelle, B., Richter, G., Volkert, C., Surface dislocation nucleation controlled deformation of Au nanowires, App. Phys. Lett., (2014).

[15] Chen, L.Y., He, M.R., Shin, J., Richter, G., Gianola D.S., Measuring surface dislocation nucleation in defect-scarce nanostructures, Nat. Mater. (2015).

[16] Shin, J., Chen, L.Y., Sanli, U.T., Richter, G., Labat, S., Richard, M.I., Cornelius, T., Thomas, O., Gianola, D.S., Controlling dislocation nucleation-mediated plasticity in nanostructures via surface modification, Acta. Mater., (2019).

[17] Okamoto, H., Massalski, T., Swartzendruber, L., Beck, P., The Au −Fe (gold-iron) system, Bull. Alloy Phase Diag. (1984).

[18] Cheng, G., Yin, S., Chang, T.H., Richter, G., Gao, H., Zhu, Y., Anomalous tensile detwinning in twinned nanowires, Phys. Rev. Lett., (2017).

[19] Minkwitz, C., Herzig, C., Rabkin, E., Gust, W., The inclination dependence of gold tracer diffusion along a Σ3 twin grain boundary in copper, Acta. Mater. (1999).

[20] Braithwaite, E.R., Haber, J., Molybdenum: An Outline of its Chemistry and Uses, (2013).

[21] Williams, D.B., Carter, C.B., X-ray spectra and images, transmission electron microscopy, in: A Textbook for Materials Science, (2009).

[22] Egerton, R.F., Electron energy-loss spectroscopy in the electron microscope, Springer Science & Business Media (2011).

[23] Malis, T., Cheng, S., Egerton, R., EELS log-ratio technique for specimen-thickness measurement in the TEM, J, Electron Microsc. Tech.(1988).

[24] Gatan, Why EELS . https://eels.info/why-eels/overview, (2020).

[25] Ahn, C.C., Transmission Electron Energy Loss Spectrometry in Materials Science and the EELS Atlas, (2006).

[26] Koch, C. T., FRWR tools Plugin for Digital Micrograph (Humboldt- Universität zu Berlin).

[27] Hÿtch, M.J., Snoeck, E., Kilaas, R., Quantitative measurement of displacement and strain fields from HREM micrographs, (1998).

[28] Benoit, M., Langlois, C., Combe, N., Tang, H., Casanove, M.J., Structural and electronic properties of the Au(001)/Fe(001) interface from density functional theory calculations, (2012).

[29] Freund, L.B., Suresh, S., Thin film Materials: Stress, Defect Formation and Surface Evolution, (2004).

[30] Duhl D., Hirano K.I., Cohen M., Diffusion of iron, cobalt and nickel in gold, (1963).

[31] Neumann, F.E., Meyer, O.E., Vorlesungen über die Theorie der Elasticität der festen Körper und des Lichtäthers: gehalten an der Universität Königsberg, BG Teubner, (1885).

[32] Mehrer, H., Diffusion in Solids: Fundamentals, Methods, Materials, Diffusion–Controlled Processes, Springer Science & Business Media, (2007).

[33] Sutton, A.P., Balluffi, R.W., Interfaces in Crystalline Materials, (1995).

[34] Self-Diffusion in Gold. Self-Diffusion in Gold. Phys. Soc. (1957).

[35] Triftshäuser, W., McGervey, J.D., Monovacancy formation energy in copper, silver, and gold by positron annihilation. Appl. Phys. (1975).

[36] Larche, F., Cahn, J., The interactions of composition and stress in crystalline solids, J. Res. Natl. Bur. Stand., (1984).

[37] Cahn, J.W., On spinodal decomposition in cubic crystals, Acta. Metall., (1962).

[38] Munoz, J.A., Lucas, M., Mauger, L., Halevy, I., Horwath, J., Semiatin, S., Xiao, Y., Chow, P., Stone, M., Abernathy, D., Electronic structure and vibrational entropies of FCC Au–Fe alloys, Phys. Rev. B, (2013).

[39] Grünwald, W., Haessner, F., Thermisch aktivierte Korngrenzenwanderung in gewalzten Goldeinkristallen unter dem Einfluss gelöster Fremdatome, Acta. Metall., (1970).

[40] Katona, G., Erdélyi, Z., Beke, D., Dietrich, C., Weigl, F., Boyen, H.G., Koslowski, B., Ziemann, P., Experimental evidence for a nonparabolic nanoscale interface shift during the dissolution of Ni into bulk Au (111), Phys. Rev. B., (2005).

[41] Erdélyi, Z., Katona, G., Beke, D., Nonparabolic nanoscale shift of phase boundaries in binary systems with restricted solubility, Phys. Rev. B., (2004).

[41] Hirth, J., Pond, R., Dislocations and disconnections as interface defects relating to structure and phase transformations, Acta. Mater., (1996).

[42] Howe, J., Pond, R., Hirth, J., The role of disconnections in phase transformations, Progr. Mater. Sci. (2009).

[43] Hirth, J. and Pond, R., Acta Mater. 44, 4749 (1996).

[44] Medlin, D.L. and Sugar J.D., Scripta Mater. 62, 379 (2010).

[45] Han, J., Thomas, S.L., Srolovitz, D.J., Grain-boundary kinetics: a unified approach, Progr. Mater. Sci. (2018).

[46] Zhu, Y.M., Morton, A.J., Nie, J.F., Growth and transformation mechanisms of 18R and 14H in Mg–Y–Zn alloys, Acta. Mater., (2012).

[47] Hutchinson, C.R., Fan, X., Pennycook, S.J., Shiflet, G.J., On the origin of the high coarsening resistance of Ω plates in Al–Cu–Mg–Ag Alloys, Acta. Mater., (2001).

[48] Porter, D.A., Easterling, K.E., Sherif, M., Phase Transformations in Metals and Alloys. (2009).

[49] Frebel, M., Predel, B., Beitrag zur Kenntnis einer durch volumendiffusion gesteuerten diskontinuierlichen

ausscheidung in Au–Fe mischkristallen, Mater.Sci.Eng., (1974).

[50] Favez, D., Wagnière, J.D., Rappaz, M., Au–Fe alloy solidification and solid-state transformations, Acta. Mater. (2010).

[51] Amram, D., Klinger, L., Rabkin, E., Phase transformations in Au (Fe) nano and microparticles obtained by solid state dewetting of thin Au–Fe bilayer films, Acta. Mater., (2013).

[52] Vaithyanathan, V., Wolverton, C., Chen, L., Multiscale modeling of precipitate microstructure evolution, Phys. Rev. Lett., (2002).

[53] Kim, K., Roy, A., Gururajan, M.P., Wolverton, C., Voorhees, P.W., First-principles/Phase-field modeling of θ′ precipitation in Al-Cu alloys, Acta. Mater., (2017).

[54] Ji, Y., Ghaffari, B., Li, M., Chen, L.Q., Phase-field modeling of θ′ precipitation kinetics in 319 aluminum alloys, Comput. Mater. Sci., (2018).

[55] Hutchinson, C., Modeling the kinetics of precipitation in aluminium alloys, in: Fundamentals of Aluminium Metallurgy, (2011).

[56] Bourgeois, L., Medhekar, N.V., Smith, A.E., Weyland, M., Nie, J.F., Dwyer, C., Efficient atomic-scale kinetics through a complex heterophase interface, Phys. Rev. Lett., (2013).

[57] Roth, T., The surface and grain boundary energies of iron, cobalt and nickel, Mater. Sci. Eng., (1975).

[58] Langer, J.S., Sekerka, R.F., Theory of departure from local equilibrium at the interface of a two-phase diffusion couple, Acta. Metall., (1975).

[59] Beke, D.L., Atomic interpretation of the interface transfer coefficients for interdiffusion in AB binary phase separating system, Int. J. Heat Mass Transf., (2017).

[60] Qi, Y., Richter, G., Suadiye, E., Klinger, L., Rabkin, E., Interdiffusion in bimetallic Au–Fe nanowhiskers controlled by interface mobility, Acta Materialia, 2020.

4. NANO-DEFORMATION

4.1 Interdiffusion-Induced Bending of Bimetallic Nanowhiskers

Nanocrystalline materials usually yield at near theoretical shear strength and this makes the plastic forming of the nanomaterials via mechanical loading a big challenge. When tried, due to newly created dislocation piling, loading leads to either catastrophic failure or uncontrolled shapes. Therefore, utilizing different strategies are important to achieve controlled architectures at nano scales. Here, we use the chemical stress created by imbalanced interdiffusion to manipulate NWs shape[49].

Annealing the bimetallic NWs at elevated temperatures led to gradual change of curvature and irreversible bending. We show here changes at the thickness, microstructure, composition and the heat treatment parameters can lead to a controlled plastic deformation of bimetallic NWs.

4.2 General Aspects of Plastic Deformation at Small Scale

When we look at macro scale the deciding point of many forming processes are related to defects and polycrystalline structure of the metals. Depending on parameters like grain size, sacking fault energy, strain rate and composition, plastic deformation of polycrystalline bulk metallic materials driven by; pre-existing/newly formed dislocation sources [1], formation of deformation twinning and stacking faults [2], grain boundary sliding [3] or phase transformations [4]. In contrast to bulk, deformation of single crystalline defect free nanocrystals such as NWs [5] and NPs is controlled via nucleation of new

dislocations. In the uniaxial deformation regime, the nanocrystal deforms elastically up to very high strains of several percents and stresses of several gigapascals, followed by a catastrophic plastic failure (Figure 4.1) [6].

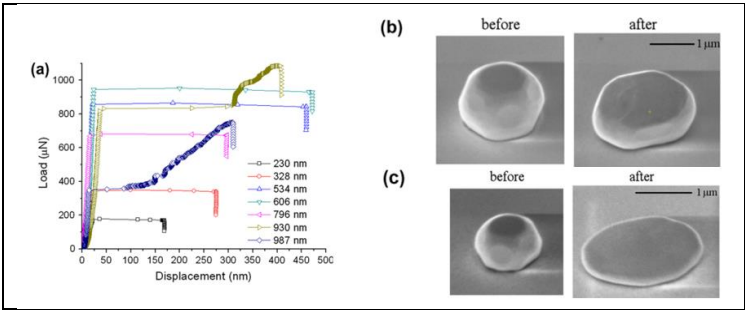

Figure 4.1 (a) Load-displacement curves of different size microparticles, (b) SEM image of compressed ~ 800nm to diameter particle, (c) SEM image of compressed ~300nm top diameter microparticle. [6]

Literature refers to this failure mode as nucleation controlled plasticity [7-9]. Plasticity initiation in single crystalline Au NWs via nucleation of prismatic dislocation loops also observed *in-situ* and modelled numerically [10]. For single crystalline NPs and NWs since their strength is the main challenge to yield them for a desired shape. Main mechanical aspect that nucleation controlled plasticity changes in nanocrystal is that it leads to high mechanical strength approaching its upper theoretical limit [6-12]. This strength increase also increases the difficulty of yielding the material to desired shape [13-15]. Such forming may be necessary because the variety of shapes of the as-synthesized defect-free nanocrystals is severely limited by the relative specific surface energies of the crystal Facet as discussed widely at the previous chapters of this work. The curvature of NWs and the morphology of the structure cannot effectively manipulated using the mechanical load [16]. An

alternative to mechanical stress introduction, is utilizing the chemical stresses created during interdiffusion [17]. Imbalance of the atomic diffusion causes vacancy flux, which is accompanied with lattice drift, and shape changes due to climb of edge dislocations [17-21]. In addition, the scarcity of internal vacancy sinks may result in the generation of high internal elastic stresses and viscous material flow [17, 21]. We should note that chemical diffusion induced stresses represent dire problems at some of the nanostructured technologies such as Li-ion batteries [22]. During insertion/removal of alkali ions cause significant shape changes, fracture and capacity decrease of the battery [23-25].

However, the possibility of using interdiffusion-generated internal stress for controlled plastic forming at the nanoscale has not yet been explored. Here, we performed annealing of Au/Fe bimetallic NWs to demonstrate the feasibility of controlled plastic forming of NWs by interdiffusion-generated stresses.

4.3 Experimental Setup

The preparation of Au/Fe bimetallic NWs is described in detail at the Chapter 2. The same NWs were used to challenge the plastic forming problem.

4.3.1 Preparation of Nanowhiskers for Annealing

Au/Fe bimetallic NWs were harvested using an easy-lift system in a focused ion beam (FIB) −scanning electron microscope (SEM) dual beam instrument (FEI Helios Nanolab Dualbeam G3). For the heat treatments, the NWs were mounted on Mo foil using Pt deposition (Figure 4.2). The Mo foil substrates were

employed because of a favorable combination of their thermal conductivity (ensuring homogeneous distribution of temperature), oxidation resistance, and mechanical strength.57 The NWs have been cut into several segments, thus enabling a comparative analysis of their cross-sectional microstructures before and after heat treatment. Employing very low ion beam currents, small pixel number (738 × 512 or 1536 × 1024), and short dwell time (50−100 ns) for imaging (30 keV, 1.1 pA) and cutting (30 keV, 7 pA) enabled minimizing the damage to the NWs caused by Ga ion beam exposure.

4.3.2 Annealing Treatments of Nanowhiskers

The *in-situ* heating experiments were performed in a high-resolution scanning electron microscope (Zeiss Ultra Plus) equipped with a heating stage (Kammrath Weiss heating module 1050 °C). A heating rate of 5 °C s^{-1} was used for the annealing. The *ex-situ* heating experiments were performed in a rapid thermal annealing furnace (RTA; ULVACRIKO MILA 5000 P−N) under the flow of forming gas (Ar-10 vol % H_2, 6N purity). The heating rate was 40 °C s^{-1}, while fast cooling was achieved by switching off the heating.

4.3.3 Characterization of Nanowhiskers

The atomic resolution microstructure features and the composition of the NWs were characterized in a scanning transmission electron microscope (STEM). The cross-sectional TEM lamellae were prepared from the NWs employing standard FIB procedures. STEM was performed with a double Cs-corrected FEI 80-300 Themis G^2 operated at 300 kV. A 21

mrad beam convergence semi-angle was used, resulting in spatial resolution better than 0.9 Å. With camera length set at 94 mm, inner and outer collection semi-angles of 119 and 200 mrad, respectively, were used for the HAADF detector. The low-angle annular dark-field (LAADF) and bright-field (BF) STEM images were also collected in the semi-angle ranges of 19−33 and 0−11 mrad, respectively. Energy dispersive X-ray spectroscopy (EDX) mapping was performed in STEM using a Dual-X detector (Bruker) with an effective solid angle of 1.76 sr. selected area diffraction patterns (SADPs) were acquired in an FEI Technai T20 TEM operating at 200 keV. Finally, transmission Kikuchi diffraction (TKD) measurements were conducted in the Zeiss SEM equipped with a TKD system (Bruker).

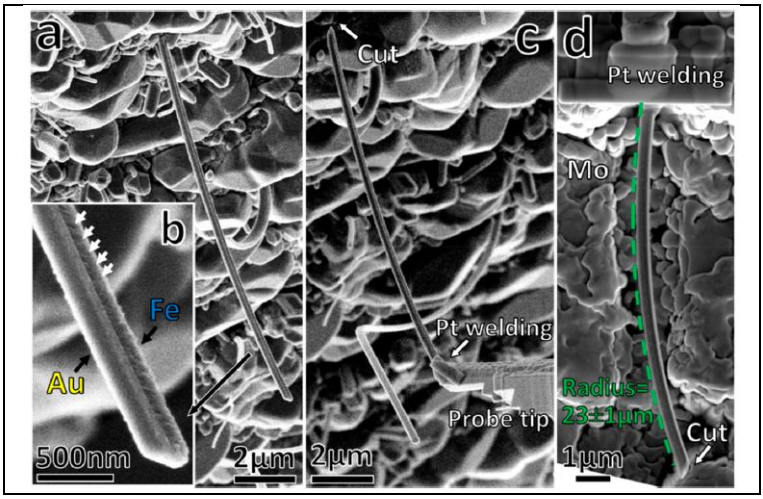

Figure 4.2 Au/Fe bimetallic NW characterization, harvesting, and mounting. Secondary electron (SE)-SEM micrographs of (a) a NW grown on a W substrate; (b) an enlarged view to distinguish the Fe layer on the Au NW; white arrows mark some of the morphological features on the polycrystalline Fe layer associated with the GBs or nanocavities between the nanocrystalline Fe grains; (c) welding of the probe tip and the NW employing Pt deposition followed by cutting the NW free from the W substrate; (d) mounting of the NW on a Mo foil substrate by Pt deposition and cutting it free from the probe tip; the green dashed line highlights the radius of curvature of the NW. The error in radius of curvature is related to the measurement uncertainties.

4.3.4 As-Synthesized Au/Fe Bimetallic Nanowires

The side facets of Au NWs were {111} and {100}, which are the closest-packed and second closest packed planes, respectively, of the FCC lattice. The Fe layers deposited on the {100} facets were single crystalline (SX), whereas their

counterparts on the {111} facets were polycrystalline (PX) Figure 4.3.

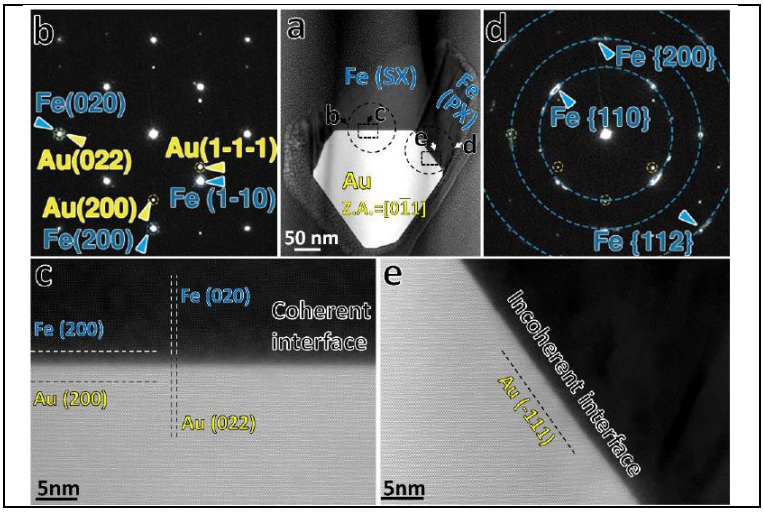

Figure 4.3 Interfaces in bimetallic Au/Fe NW. (a) HAADF-STEM image of the cross-section of a representative NW; (b, c) the SADP and atomic-resolution HAADF-STEM image showing a single-crystalline Fe layer on a Au (100) facet and a coherent interface between them; (d, e) the SADP and atomic-resolution HAADF-STEM images showing a poly-crystalline Fe layer on a Au (111) facet and an incoherent interface between them. Images were taken along the $[0\bar{1}1]$ Z.A. of Au.

Typical as-prepared bimetallic NWs exhibiting both SX and PX Fe layers are shown in Figure S1. The SX Fe layer exhibits the Bain orientation relationship with the Au NW, for example, $[01\bar{1}]$ Au// [001] Fe, (011) Au// (010) Fe, and (100) Au// (100) Fe. Most of the nano grains in the PX Fe layers exhibit low misorientation angles, which is confirmed by the diffuse diffraction streaks in the diffraction patterns (Figure 4.3d). The reason why incoherent PX interface and coherent SX interface

were formed on {111} and {100} Au facets, respectively, was probably related to the high difference of the respective values of lattice mismatches between Fe coating and Au substrate. Indeed, it was shown that during initial stages of Fe deposition on Au (111), the first few monolayers of Fe grow pseudomorphically as a FCC phase [26]. Even though the corresponding lattice mismatch is very high (about 14%), so that at a thickness of only 2−3 monolayers a set of misfit dislocations is nucleated at the interface. These dislocations serve as heterogeneous nucleation sites of the BCC α-Fe phase, which occurs once the thickness of the Fe layer reaches 5−7 monolayers. The stochastic nature of this nucleation in the strong stress field of misfit dislocations causes a transformation of the single crystalline pseudomorphic γ-Fe layer into the polycrystalline α-Fe. In contrast, very small lattice mismatch between α-Fe and (100) Au of only 0.59% (Bain orientation relationship $[0\bar{1}1]_{Au}//[001]_{Fe}$, $(011)_{Au}//(010)_{Fe}$, and $(100)_{Au}//(100)_{Fe}$) probably causes the Frank−Van der Merwe growth of α-Fe on {100} facets of Au NW from the onset of Fe deposition.

4.4 Annealing Results and Discussion

In addition to above mentioned characterization as-synthesized bimetallic NW was slightly bent in the
direction toward the Fe coating (Figure 4.2d), which cannot be observed on the single-phase Au NWs.
This bending can be explained by a combined effect of lattice mismatch strain and island-coalescence stress in the SX and PX Fe layers. Figure 4.4 presents an estimation of the contribution of this two effect.

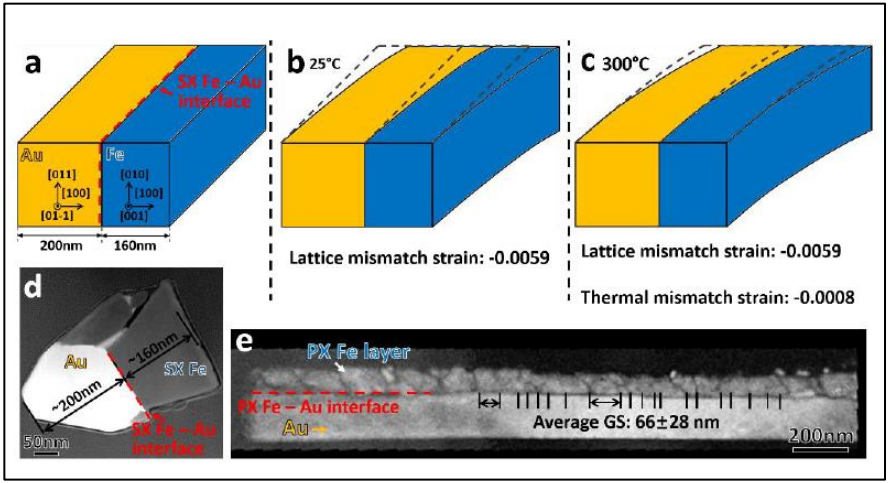

Figure 4.4 Illustration of the initial NW bending due to lattice mismatch strain and island coalescence stress. (a-d) the lattice mismatch strain induced by the heteroepitaxy at the single-crystalline Fe – Au interface; (a) the model of initial configuration; (b) the bending induced by the lattice mismatch strain; (c) additional elastic bending at 300 °C due to the mismatch in thermal expansion coefficients of Au and Fe; (d) the geometric parameters used for the estimation of the NW radius of curvature; (e) Longitudinal cross-sectional TKD band contrast image of the NW illustrating the geometric parameters used for the estimation of island coalescence stress in PX Fe layer.

The lattice mismatch strain at the SX Fe−Au interface between $(011)_{Au}//(010)_{Fe}$ can be estimated as $\varepsilon_m = (d_{Fe(010)} - d_{Au(011))}/d_{Au(011)} = -0.0059$, where $d_{Fe(010)} = 2.867$ Å and $d_{Au(011)} = 2.884$ Å are the interplanar spacings in Fe and Au[27] The radius of curvature associated with this mismatch strain was estimated to be 40μm employing the Timoshenko formula [28]. Numerous nanocavities at the GBs in the PX Fe layer also cause high tensile stress in the layer, similar to island zipping stress [29]. Using the model of Nix and Clemens [29] this stress was estimated to be 19.1 GPa; this tensile stress also contributes to the bending of NWs toward the Fe layer. However, it is worth noting that such high stress is certainly partially relaxed by various plasticity mechanisms [30] such as plastic deformation of the Au NW resulting in the formation of ledges at the PX Fe−Au interface, see Figure 4.5.

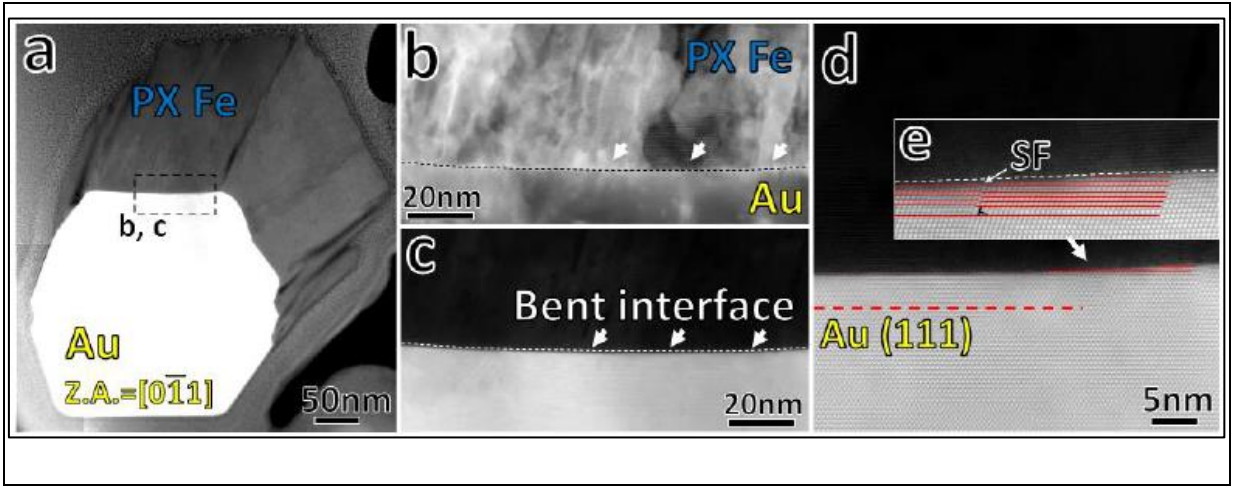

Figure 4.5 Fe-Au interface bending due to island coalescence in the PX Fe layer. (a) HAADF-STEM of the cross-section of the Au/Fe NW; (b, c) LAADF and HAADF-STEM images showing the bending of the PX Fe layer – Au interface due to the island coalescence induced tensile stress in the Fe layer; arrows and dashed lines highlight the bent interface; (d, e) atomic-resolution HAADF-STEM image showing the ledges on the interface and a stacking fault (SF) in the Au NW. The formation of interface ledges and a Shockley partial dislocation indicated the strain was partially relieved by plastic deformation. Images were taken along the [0$\bar{1}$ 1] Z.A. of Au.

4.5 In Situ Heat Treatments of the Nanowhiskers

In this series of experiments three NWs were lifted, heat treated and characterized (Table 4.1).

Table 4.1 Heat treated nanowires and the art of the treatment.

Nanowire	Fe Layer Thickness (nm)	Heat Treatment Art
NW#1	200	*In-situ*
NW#2	200	*In-situ*
NW#3	50	*Ex-situ*

NW#1 and NW#2 were mounted on a Mo foil, which was fitted into the heating stage, and the annealing was performed under vacuum of 5×10^{-5} mbar in the SEM chamber (Zeiss Ultra-Plus SEM). Before each SEM image acquisition, the temperature was kept constant for 20 min for thermal equilibration and stage stabilization. NW#3 with a ∼50 nm thick Fe layer was annealed *ex situ*. Figure 4.6 gives an overview for the NW#1 heating results. We first observed reversible bending behavior at relatively low temperatures (Figure 4.6a−c). The radius of curvature, *R*, changed from 23 ± 1 μm at room temperature to 18 ± 1 μm at 300 °C, increasing back to 21 ± 1 μm upon cooling to 25 °C after the heating system was switched off. This reversible bending behavior was attributed to elastic deformation due to the mismatch of the thermal expansion coefficients of the Au NW and the Fe coating (14.2×10^{-6} °C^{-1} and 11.4×10^{-6} °C^{-1}, respectively). Higher thermal expansion of Au compared to that of Fe upon heating from room temperature to 300 °C resulted in the development of compressive stress in the Au NW as the mismatch strain rose from −0.0059 to −0.0067. This increase in the mismatch strain

changes the estimated value of R from 40 to 36 μm, in qualitative agreement with the experimental results.

While we are making estimations of lattice mismatch strain and island zipping stress for NW#1 we consider two physical reasons for the observed bending on as-synthesized NW#1 at 25 °C; the lattice mismatch strain at the coherent single-crystalline (SX) Fe-Au interface, and the strain induced by the closing the nanocavities at the grain boundaries (GBs) in the poly-crystalline (PX) Fe layer.
First we estimate the contribution from the lattice mismatch strain. Because there is no coherency strain in the PX Fe layer adjacent to the incoherent PX Fe-Au interface, we will only consider the lattice mismatch strain at the coherent SX Fe-Au interface. Here, we use a simplified model (Figure 4.4), in which the Au NW has a square cross-section with four {100} facets, with the SX Fe layer covering one facet in the Bain orientation relationship with the Au NW. The mismatch strain between $(011)_{Au}//(010)_{Fe}$ on the Au NW can be estimated as $\varepsilon_m = d_{Fe(010)} - d_{Au(011)} / d_{Au(011)} = -0.0059$, where $d_{Fe(010)} = 0.2867\ nm$ and $d_{Au(011)} = 0.2884\ nm$ are the interplanar spacings in Fe and Au, respectively. To estimate the radius of curvature, *R*, the Timoshenko formula describing the bending of bimetallic beams is employed here:

$$R = \frac{E_{Fe}^2 h_{Fe}^4 + 4E_{Fe}E_{Au}h_{Fe}^3 h_{Au} + 6E_{Fe}E_{Au}h_{Fe}^2 h_{Au}^2 + 4E_{Fe}E_{Au}h_{Au}^3 h_{Fe} + E_{Au}^2 h_{Au}^4}{6E_{Fe}E_{Au}(h_{Fe}+h_{Au})h_{Fe}h_{Au}\varepsilon_m}$$

Eq. 4.1

where $E_{Fe} = 125\ GPa$ and $E_{Au} = 82\ GPa$ are the Young's moduli of Fe and Au along [001] and [011] crystallographic directions, respectively. $h_{Fe} = 160\ nm$ and $h_{Au} = 200\ nm$ are the thicknesses of the Fe and Au constituents, respectively, estimated from Figure 4.4d.

The radius of curvature, *R*, is estimated to be 40 μm, which is somewhat larger than the measured one, 23±1 μm, in figure 4.2. This difference could be caused by the tensile stress developed in the PX Fe layer during growth, and compressive strain in the Au NW in the vicinity of the interface (Figure 4.5). In particular, the drive of the system to close the long and narrow nanocavities at the GBs induces the tensile stress in the film, similar to the island zipping stress during the Volmer–Weber film growth. Here we estimate the average tensile stress, $\langle \boldsymbol{\sigma} \rangle$, using Nix-Clemens model:

$$\langle \boldsymbol{\sigma} \rangle = \left[\left(\frac{\mathbf{1}+\boldsymbol{v}}{\mathbf{1}-\boldsymbol{v}} \right) . \boldsymbol{E} . \frac{(2\boldsymbol{\gamma_s}-\boldsymbol{\gamma_{gb}})}{\boldsymbol{r}} \right]^{\mathbf{1/2}} \qquad \textbf{\textit{Eq. 4.2}}$$

where $\boldsymbol{v}$, *E*, $\boldsymbol{\gamma_s}$, and $\boldsymbol{\gamma_{gb}}$,are the Poisson's ratio, the Young's modulus, the surface energy and the grain boundary energy of ferrite α-Fe, which were chosen to be 0.3, 210 GPa, 2.1 J/m2 and 1 J/m2, respectively [37]. The parameter $\boldsymbol{r}$ denotes the radius of the grain and its chosen value is 33 nm, based on the measurements in Figure 4.4e. The average tensile stress,$\langle \boldsymbol{\sigma} \rangle$, is estimated to be 19.1 GPa. Though this high stress may partially relax by various plasticity and diffusion mechanisms, our results indicate that the residual internal stress in the PX Fe layer is tensile, and contributes to the bending of the as-prepared NW.

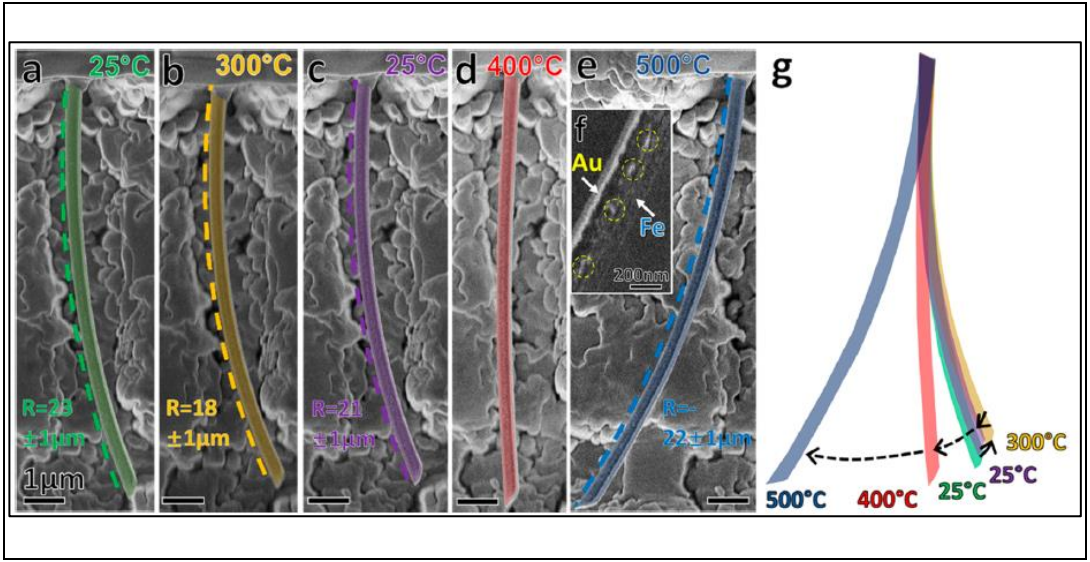

Figure 4.6 Reversible and irreversible bending of an Au/Fe bimetallic NW at elevated temperatures. SE-SEM micrographs of (a−c) reversible bending of NW#1 at 300 °C in elastic deformation regime; (d, e) irreversible bending of NW#1 at 400 and 500 °C. (f) Enlarged view of the NW acquired using back-scattered electrons (BSE), visualizing the Au clusters on the Fe layer by their Z-contrast. (g) Schematic illustration of the bending process. The radii of curvature, R, of the NW at each temperature are presented in panels a−e. The error in determining of the radius of curvature was estimated by performing 5−6 independent curvature measurements.

It was also noticed in the experiment that the radius of curvature of NW#1 did not fully recover from 18 back to 23 μm upon cooling from 300 to 25 °C, since the measured value of ***R*** was 21 μm after the full heating/cooling cycle. This was due to the healing of some nanocavities in the Fe layer at 300 °C, which resulted in volume shrinkage in the Fe coating Figure (4.7-4.9). Upon discussion on the kinetics of nanocavities at 300°C we observed that while the radius of curvature of the NW#1 decreased to R = 18±1 μm upon heating to 300 ºC, it has not fully recovered to its original value R = 23±1 μm after the NW has been cooled down to 25 ºC. A slight decrease of the radius of curvature upon the full heating-cooling cycle (from 23±1 to 21±1 μm) is related with the irreversible processes occurring in the NW at elevated temperatures. We attribute this phenomenon to the healing of nanocavities in the Fe layer, which results in a volume shrinkage of the Fe constituent and concomitant increase of the tensile stress in the layer. The healing and annihilation of the nanocavities at elevated temperatures was demonstrated in the ex-situ heat treatment, see Figures 4.7 and 4.8. We assume that the healing process occurred via Fe atoms diffusion through a GB connected to the nanocavity. The GB itself plays a role of a source of Fe atoms (or a sink of vacancies), which in turn contributes to the increase of tensile stress in the Fe coating. To prove this hypothesis, we propose a model to estimate the time required for Fe GB diffusion to heal a slit-shaped nano-cavity. In our model, the main driving force for the nano-cavity healing is the decrease of energy associated with replacing two free Fe surfaces (side surfaces of the slit) with an Fe GB.

If we consider a slit-shaped nano-cavity with the thickness h=3 nm and total length L_0= 50 nm, located at the distance l_0 = 20 nm away from the Fe-Au interface (Figure 4.9). A GB in the PX Fe layer is connected to the tip of the nanocavity. The depletion of Fe atoms at the GB and their diffusion towards the nanocavity

lead to the latter retraction and increase of the distance between the nanocavity tip and the Fe-Au interface, *l*. We will assume that the Fe grains on both sides of the GB homogeneously drift towards the GB (this way, the generation of additional elastic stresses at the GB associated with normal displacement variations is avoided). In this case, the distribution of chemical potential of Fe atoms along the GB, $\mu(x)$, is a parabolic (second-order) function of the distance, *x*, from the Fe-Au interface, $\mu(x)=ax^2+bx+c$ [38]. Furthermore, we assume that there is no Fe diffusion flux entering the GB at the Fe-Au interface, $|\partial\mu/\partial x|_{x=0} = 0$. This boundary condition results in $b = 0$ and $\mu(x)=ax^2+c$. The chemical potential of Fe atoms averaged over the whole GB length, *l*, is;

$$\bar{\mu}_0 = \frac{1}{l}\int_0^l (ax^2 + c)dx = \frac{1}{l}\left(\frac{al^3}{3} + cl\right)$$

Eq. 4.3

On the other hand, the average chemical potential of Fe atoms that is *l* away from the Fe-Au interface can be estimated by adding an infinitesimal thin layer of Fe at the GB, calculating the change of the total energy of the system, and normalizing it by the number of added atoms:

$$\bar{\mu}_0 = \Omega\frac{\gamma_s+\gamma_i-\gamma_{Au}}{l} \qquad \textit{Eq. 4.4}$$

where Ω denotes the atomic volume of Fe; γ_s , γ_i , and γ_{Au} are the surface energy of Fe, Fe/Au interface energy and surface energy of Au, respectively.

Substituting Eq. (S3) in Eq. (S4) yields,

$$\frac{al^2}{3} + c = \Omega \frac{\gamma_s + \gamma_i - \gamma_{Au}}{l} \qquad \textit{Eq. 4.5}$$

Furthermore, the chemical potential of the Fe atoms on the inner surface of the nanocavity tip (i.e. at the distance *l* from the Fe-Au interface) is,

$$\mu_f = al^2 + c \approx \Omega \frac{\gamma_{gb} - 2\gamma_s}{h} \qquad \textit{Eq. 4.6}$$

where γ_{gb} is the GB energy of ferrite α-Fe. The last term on the right hand side of Equation S6 is associated with the curvature of the inner surface of the nanocavity at the tip. Solving Eqs S5-S6 yields,

$$a = \frac{3\Omega}{2l^2}\left(\frac{\gamma_{gb} - 2\gamma_s}{h} - \frac{\gamma_s + \gamma_i - \gamma_{Au}}{l}\right) \qquad \textit{Eq. 4.7}$$

$$c = \frac{\Omega}{2}\left(3.\frac{\gamma_s + \gamma_i - \gamma_{Au}}{l} - \frac{\gamma_{gb} - 2\gamma_s}{h}\right) \qquad \textit{Eq. 4.8}$$

Then the GB diffusion flux of Fe atoms entering the nano-cavity at the intersection line of the GB and the inner surface of the nano-cavity is;

$$J = -\frac{D_{gb}\delta}{kT} \cdot \left(\frac{\partial \mu}{\partial x}\right)_{x=1} = -\frac{D_{gb}\delta}{kT}\frac{3\Omega}{l}\left(\frac{\gamma_{gb} - 2\gamma_s}{h} - \frac{\gamma_s + \gamma_i - \gamma_{Au}}{l}\right)$$

Eq. 4.9

where D_{gb} and δ are the self-diffusion coefficient of Fe along the GB at 300°C and the GB width, respectively. *kT* has its usual thermodynamic meaning. Assuming the constant width of the

nanocavity, this flux cases the nanocavity retraction according to:

$$J = h.\frac{dl}{dt} \qquad \textit{Eq.4.10}$$

Substituting Equation S10 in Equation S9 yields,

$$\frac{dl}{dt} = \frac{3D_{gb}\delta\Omega}{kTlh}\left(\frac{2\gamma_s-\gamma_{gb}}{h} + \frac{\gamma_s+\gamma_i-\gamma_{Au}}{l}\right) \qquad \textit{Eq.4.11}$$

For $l_0 >> h$ the magnitude of the second term on the RHS of Equation S11 is small compared to first term, and the Equation S11 can be approximately rewritten as;

$$\frac{dl^2}{dt} \approx \frac{6D_{gb}\delta\Omega}{kTh^2}\left(2\gamma_s - \gamma_{gb}\right) \qquad \textit{Eq.4.12}$$

Solving this differential equation yields the following solution for the annealing time required for nanocavity retraction by the distance l-l_0:

$$l^2 - l_0^2 \approx \frac{6D_{gb}\delta\Omega\left(2\gamma_s-\gamma_{gb}\right)}{kTh^2}t \qquad \textit{Eq.4.13}$$

where l, l_0, T, h, δ, Ω, γ_s and γ_{gb} are chosen to be 70 nm, 20 nm, 573 K, 3 nm, 0.5 nm, $7.1\cdot10^{-6}$ m^3/mol, 2.1 J/m^2, and 1 J/m^2, respectively. D_{gb} was chosen in the range between $1.3\cdot10^{-18}$ m^2/s and $2.8\cdot10^{-16}$ m^2/s. 5,6 The time of nanocavity retraction estimated with the aid of Equation S13 is then in the range from 17 s to 1 h, depending on the GB diffusivity, in good agreement with our experimental observations. Therefore, the nanocavities healing at the temperature of 300 °C leading to the increase of tensile stress in the Fe coating is feasible on the time scale of

our experiment.

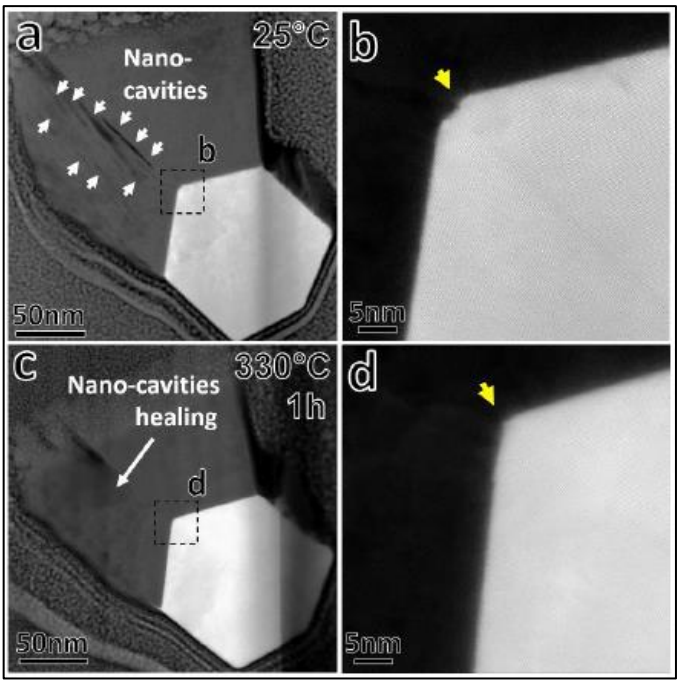

Figure 4.7 Quasi-*in-situ* demonstration of nano-cavities healing after annealing. HAADF-STEM images (a, b) showing the cross-section of a bimetallic NW in which some nano-cavities in the Fe layer were highlighted by arrows; (c, d) the same NW after annealing at 330 °C for 60 min in RTA exhibited much fewer nano-cavities. The atomic resolution HAADF-STEM images of (b, d) demonstrate that the Au-Fe interface at the facets intersection migrated towards Fe after annealing. Images were taken along the $[0\bar{1}1]$ Z.A. of Au.

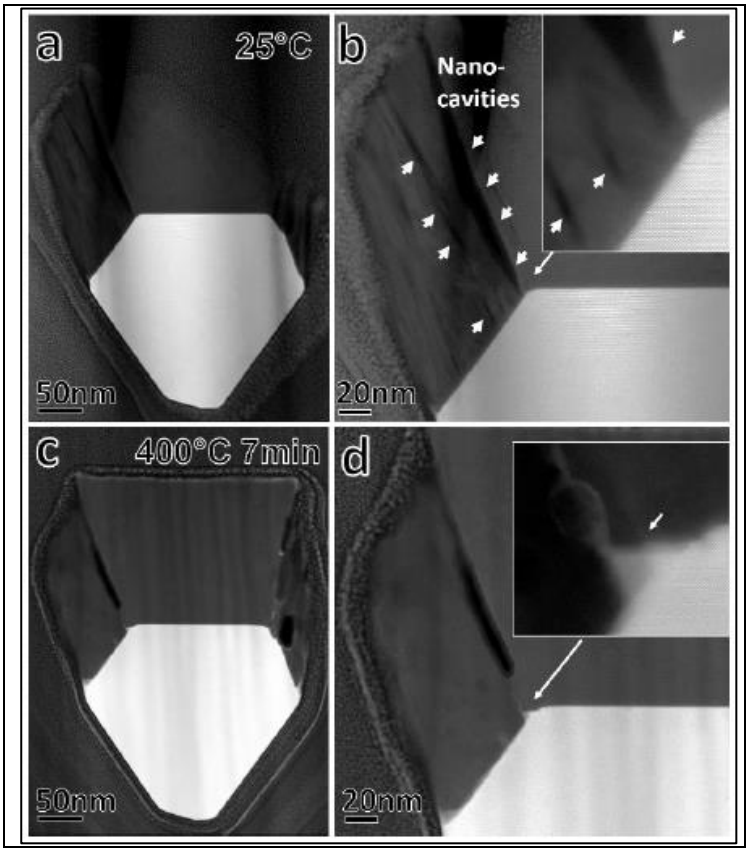

Figure 4.8 Quasi-*in-situ* demonstration of nano-cavities healing and Au penetration into Fe after annealing. HAADF-STEM images (a, b) showing the cross-section of a bimetallic NW in which some nano-cavities in the Fe layer were highlighted by arrows; (c, d) the same NW after annealing at 400 °C for 7 min in RTA exhibited much fewer nano-cavities. The enlarged HAADF-STEM images of (b, d) demonstrate the diffusion and penetration of Au into the nano-cavity at the intersection of Au facets. Images were taken along the $[0\bar{1}1]$ Z.A. of Au.

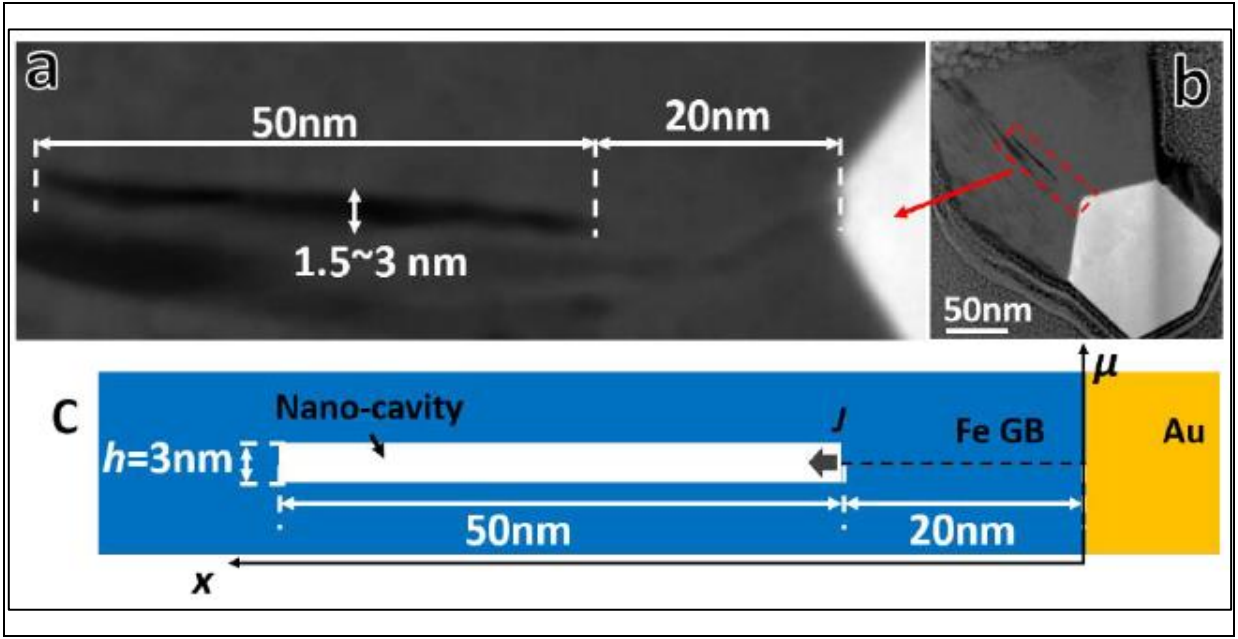

Figure 4.9 The geometric parameters of the model of a Fe nano-cavity healing by grain boundary (GB) diffusion mechanism. (a, b) HAADF-STEM images showing a representative nano-cavity in the Fe layers; (c) the schematic illustration of the nano-cavity.

Irreversible bending in the opposite direction occurred when the temperature was increased above 300 °C. NW#1 was nearly straight at 400 °C and kept bending toward the Au NW reaching a curvature of 22 ± 1 μm with an opposite sign at 500 °C (Figure 4.6e). At this stage, the Fe coating and Au NW were under compression and tension, respectively. Finally, from the BSE-SEM micrograph shown in Figure 4.6f, some isolated Au clusters were observed on the outer surface of Fe layer, which indicated significant Au diffusion at elevated temperatures. Indeed, the diffusional penetration of Au along the GBs and nanocavities in the Fe coating can explain the volume expansion and concomitant development of compressive stresses in the latter.

The penetration of Au into the Fe layers via the nanocavities and GBs is demonstrated in Figure 4.10. This penetration resulted in the formation of Au-rich clusters on the outer surface of the Fe layer shown in Figure 4.6f and highlighted in both normal (Figure 4.10a) and longitudinal (Figure 4.10d) cross-section views of high-angle annular dark-field scanning electron microscopy (HAADF-STEM) images of NW#1.

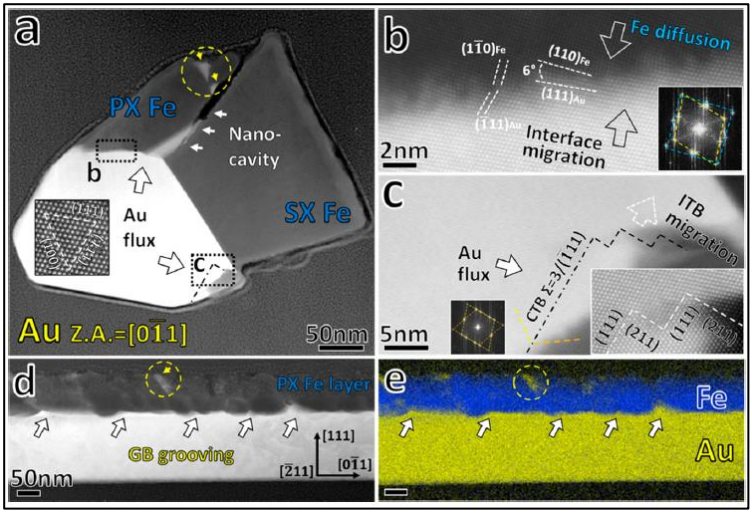

Figure 4.10 Plastic bending of the Au/Fe metallic NW induced by interdiffusion. STEM-EDX characterization of bent NW#1 after in situ heating at 500 °C. (a−c) HAADF-STEM images of the normal cross-section of NW#1, imaged along the [0$\bar{1}$1] zone axis (Z.A.) of Au. The diffusion flux of Au atoms into a Fe nanocavity at the intersection of Au (111) and (100) facets is schematically shown by arrows. (b) Nano roughness developed at the incoherent Au−Fe interface facilitating interface migration and Fe diffusion into Au; inset fast Fourier transform (FFT) image and lattice analysis indicate the incoherency of the interface. (c) Coherent twin boundary (CTB) and incoherent twin boundary (ITB) developed in Au to relax the diffusion-induced stress. (d, e) HAADF-STEM micrograph and corresponding EDX mapping of the longitudinal cross-section of NW#1, imaged along the [$\bar{2}$11] Z.A. of Au.

The GB diffusion process led to the formation of characteristic GB grooves at the Au−Fe interface, which are marked in Figure

4.10d,e. Also, the nanocavities in Fe got partially filled with the Au-rich alloy. The diffusion of Au along and segregation at the GBs in Fe nanostructures attached to the substrate has also been observed earlier by Amram et al.[31]. These phenomena have been utilized in bulk Fe−Au alloys for filling and healing of creep-induced microcavities at elevated temperatures, thus enhancing the alloy component lifetime [32].

Au diffusion along and accumulation at the GBs in the Fe layer caused its volume expansion and concomitant bending of the NW in the direction of Au. At the same time, Fe also diffused into Au via lattice diffusion. As seen in Figure 4.10b, the Au-rich phase grew at the expense of Fe, and the Au−Fe interface migrated in the Fe direction. This movement reflects high solubility of Fe in Au and negligible solubility of Au in Fe [33]. This volume interdiffusion and interface migration caused volume shrinkage of the Au constituent, since the lattice parameter of the Au−Fe alloys decreases with increasing Fe content. Finally, a twin boundary (TB) consisting of coherent and incoherent sections can be seen in Figure 4.10c. It nucleated on the free surface of the Au NW, migrated toward the Au−Fe interface, and stopped in the NW interior. This TB can be categorized as a deformation twin nucleated to relieve the diffusion generated elastic stresses in the Au NW. The twin has nucleated on the free surface of the Au NW rather than at the Au−Fe interface (the source of diffusion-generated stress) because the nucleation of the Shockley partial dislocations (also serving as twinning dislocations) is easier on the free surface than at the interface exhibiting lower diffusion mobility of Au atoms [34].

Finally, transmission Kikuchi diffraction (TKD) characterization of a segment (∼4.5 μm) of NW#1 reveals that the bending curvature was induced by a gradual lattice rotation of ∼6° of Au NW about [011] zone axis, which is normal to the

Au NW growth direction, [0$\bar{1}$1] (Figure 4.11). No GBs that could form via the polygonization process at 500 °C were found in the inverse pole figure (IPF, X-axis) image (Figure 4.11b).

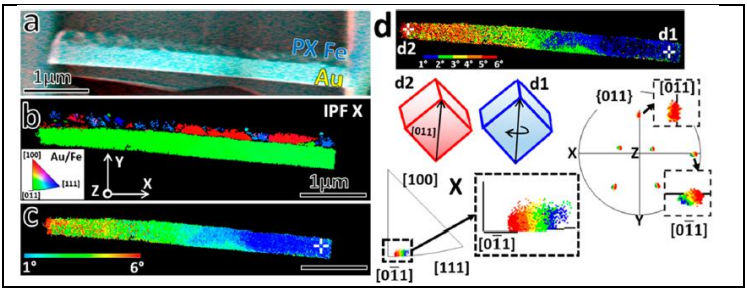

Figure 4.11 Lattice rotation in bent NW#1. (a) Color-coded dark-field (CCDF) image of the longitudinal cross-section of NW#1. (b) Orientation image with an inset illustrating the color codes of normal (Z) grain orientations. (c) Misorientation map of the Au NW where the reference location is marked by the white cross. The legend shows the range of misorientations (1°−6°). (d) Segmented misorientation map, inverse pole figure, and pole figure showing that the Au lattice distortion was caused by the lattice rotation around the [011] zone for 6°. The orientations of two locations at the ends of the segments, d1 and d2, are schematically illustrated; their [011] directions are parallel.

The interdiffusion induced plastic bending was reconfirmed in bent NW#2, which went through the same in situ heating cycle up to 500 °C as NW#1 (Figure 4.12a,b). Au diffusion via Fe GBs and nanocavities and Fe lattice diffusion into Au and accompanying interface migration are shown in Figure 4.12c,h,i. These micrographs support the hypothesis that the plastic bending has resulted from the interdiffusion between the Au NW and Fe coating.

Furthermore, a ⟨011⟩ asymmetric tilt GB characterized as a special Σ = 43/(455)$_1$/($\bar{5}$33)$_2$/99.37° GB was found at the "mouth" of the Au layer protruding into the gap between SX and PX Fe layers, Figure 4.12c,d. The formation of the GB could be understood in terms of the reduction of the energy of all GBs and interfaces in the system, Figure 4.13 gives a description on that matter. Futhemore to detail the formation of tilt GB, we will consider a simple model of a rectangular gap between two Fe layers which is filled with Au during high-temperature annealing (Figure 4.14). We will neglect the changes in the geometry of Au NW upon the gap filling, since the total volume of Au penetrating the gap is negligible in comparison to the volume of the Au NW. Thus, the total energy of all surfaces and interfaces only in the region of the gap will be considered. The initial energy per unit of longitudinal length, $E_{total}^{25°C}$ can be written as:

$$\boldsymbol{E_{total}^{25°C} = L\left(\gamma_{s-Fe}^{1} + \gamma_{s-Fe}^{2}\right) + h\gamma_{S-Au}^{1}}$$

Eq. 4.14

where *L* and *h* are the length and the width of the gap, respectively. γ_{s-Fe}^{1} and γ_{s-Fe}^{2} are the average surface energy of the PX Fe layer, and the energy of the side surface of the SX Fe layer, respectively. $\boldsymbol{\gamma_{S-Au}^{1}}$ is the energy of exposed Au surface at the entrance to the gap. Assuming that the gap is filled with Au in homoepitaxial orientation relationship with the underlying Au NW yields the following expression for the energy of the filled gap:

$$\boldsymbol{E_{total}^{500°C} = L\left(\gamma_{In-Fe}^{1} + \gamma_{In-Fe}^{2}\right) + h\gamma_{S-Au}^{1}}$$

Eq. 4.15

where $\boldsymbol{\gamma_{In-Fe}^{1}}$ and $\boldsymbol{\gamma_{In-Fe}^{2}}$ are the average energy of the PX Fe-Au interface, and the energy of the SX Fe-(277) Au interface, respectively. Another possibility is for the Au layer penetrating the gap to change its orientation, so that a low-energy SX Fe-(100) Au interface is formed on the right side of the gap. In this case, the total energy of the filled gap will be different from the one given by Equation S15:

$$\boldsymbol{E_{total}^{500°C^{*}} = L\left(\gamma_{In-Fe}^{1^{*}} + \gamma_{In-Fe}^{2^{*}}\right) + h\left(\gamma_{S-Au}^{1^{*}} + \gamma_{GB-Au}^{*}\right)}$$

Eq. 4.16

where $\boldsymbol{\gamma_{GB-Au}^{*}}$ is the energy of the GB formed at the mouth of the Au layer, and the star superscript denotes the change of surface orientation or interface crystallography. For simplicity, we assumed that the cross sectional length of the newly formed GB is the same as the gap width *h*. Since the anisotropy of surface energy of cubic metals rarely exceeds 2-3%, we will assume $\gamma_{S-Fe}^{1} \approx \gamma_{S-Fe}^{2} \approx \gamma_{S}$ ≈2.1 J/m^2, and $\gamma_{S-Au}^{1} \approx \gamma_{S-Au}^{1^{*}} \approx \gamma_{Au}$ ≈1.4 J/m^2. Because the average energy of the PX Fe-Au interface is determined for many different orientations of the Fe grains, we will assume the equal values of γ_{In-Fe}^{1}, $\gamma_{In-Fe}^{1^{*}}$, and of the incoherent interface energy, γ_{In-Fe}^{2}. We will estimate the values of these energies by the energy value of high-angle GB in Fe, ~1 J/m^2 [39]. The density functional theory [40] and regular solution model [41] – based estimates of the energy of the coherent Fe-Au interface, $\gamma_{In-Fe}^{2^{*}}$, yield the values in the range of 0.36-0.5 J/m^2. Finally, the energy of high-angle GB in Au will be estimated as one-third of its surface energy, γ_{GB-Au}^{*} ≈0.5 J/m^2. Comparing the Equations S14-S16 reveals that filling the gap between the two Fe layers by Au is energetically favorable for any values of *L* and *h*. Moreover, for *h < (1-1.3).L*, the formation of GB by lattice rotation about

$[0\bar{1}1]_{Au}$ axis leading to establishing a coherency at the SX Fe-Au interface becomes energetically more favorable than homoepitaxial penetration of Au into the gap. The analysis of Figure 4.11c, d and Figure 4.14 demonstrates that *h (<10 nm) << L (50-200 nm)* and, therefore, the formation of a GB is energetically favorable.

The penetration of Au into the gap between two Fe layers in homoepitaxial orientation relationship with the Au NW would result in the (277) plane of Au adjacent the SX Fe layer. Such Au−SX Fe interface exhibits high energy. Instead, Au penetrated the gap between the two Fe layers in a different orientation (rotated about the $[0\bar{1}1]$ axis by 99° with respect to the original Au NW), resulting in the low-index (100) plane of Au contacting the SX Fe layer at the interface and reducing the energy of the Au−SX Fe interface. The energy "penalty" of this process is the energy of the Σ43 GB formed at the "mouth", yet because its total length is significantly smaller than the length of the Au−SX Fe interface the process is energetically favorable. Finally, three deformation TBs were observed, extending from the free surface to the Au−Fe interface across the width of the Au NW (Figure 4.12 c,f) and Figure 4.14.

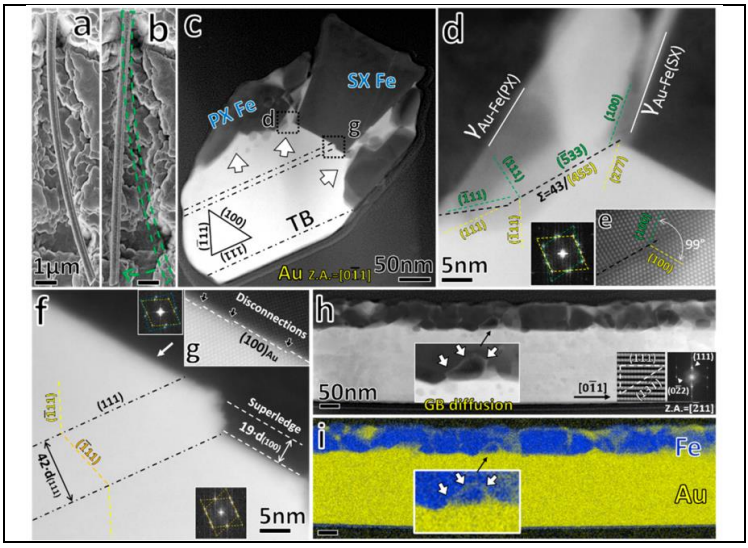

Figure 4.12 Plastic bending of the Au/Fe metallic NW mediated by tilt GBs. SEM and STEM-EDX characterization of bent NW#2 after in situ heating at 500 °C. (a, b) SE-SEM images showing the bending of NW#2 at 500 °C. (c−g) HAADF-STEM images of the normal cross-section of NW#2, acquired along the [0$\bar{1}$1] Z.A. of Au. (d, e) A tilt GB formed at the mouth of Au layer penetrating the gap between the PX and SX Fe layers. (f) Deformation twins formed to relax the interdiffusion-induced stresses and to mediate plasticity. (g) Disconnections and a superledge formed at the coherent Au−Fe interface indicating the interface migration toward Fe. (h, i) HAADF-STEM micrograph and corresponding EDX mapping of the longitudinal cross-section of NW#2, imaged along the [$\bar{2}$11] Z.A. of Au; an Fe grain fully covered with Au GB segregation layer is highlighted.

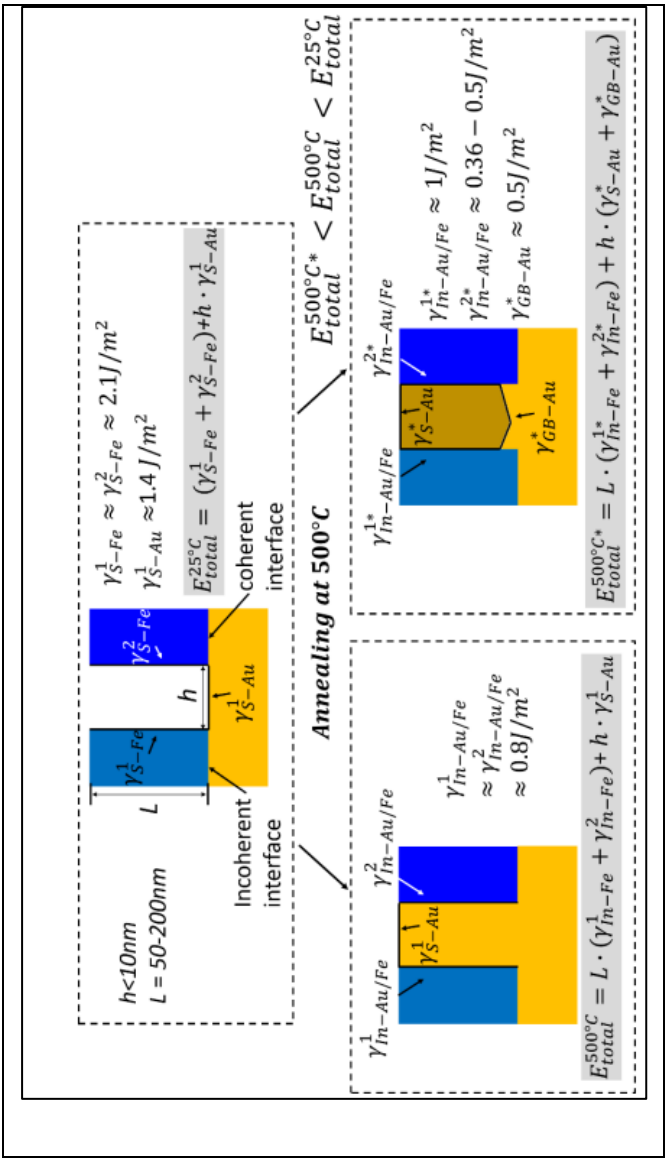

Figure 4.13 Energy minimization approach employed to explain the formation of tilt GB at the "mouth" of Au layer penetrating into the Fe nanocavity

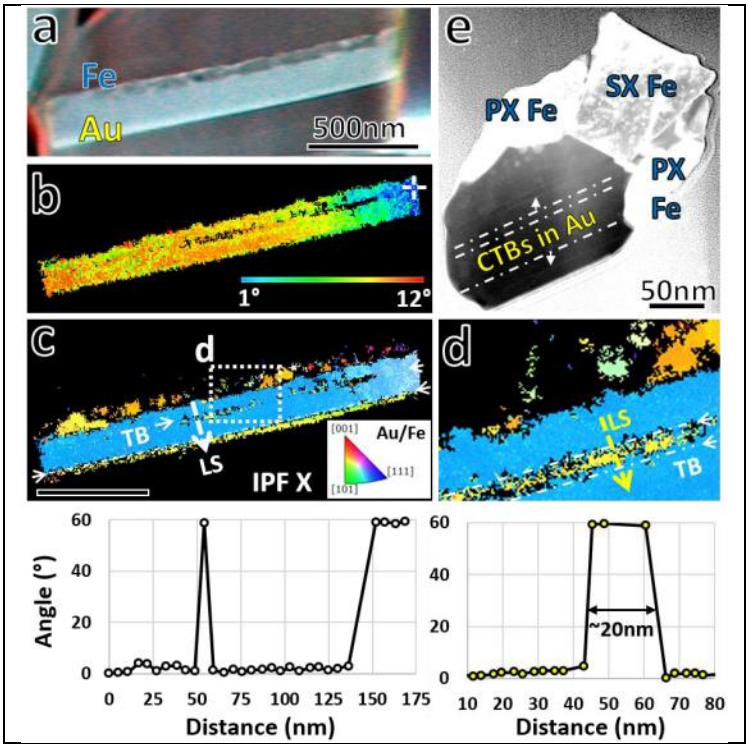

Figure 4.14 Lattice distortion and deformation twinning in bent NW#2 characterized by TKD and LAADF. (a) the CCDF image of the longitudinal cross-section of NW#2; (b) the misorientation map of the Au NW where the reference location is pointed by the white cross. The legend shows the range of misorientations (1°-12°); (c, d) the orientation images showing the twin boundary (TB) and misorientation line profile from the line scan (LS); (e) LAADF image showing the twin boundaries in the cross-section normal to the NW axis $[0\bar{1}1]_{Au}$.

It is worth noting that unlike the TBs formed in Au NWs during tensile testing experiments, which are inclined with respect to the NW growth axis [35] the TBs observed here are parallel to the growth axis and extend over the whole length of the NW. This is due to difference in the stress states and Schmid factors for the {111}⟨011⟩ slip system during uniaxial loading [35] and diffusion induced bending uncovered in the present work.

The irreversible bending of NW#1 and NW#2 caused by *in-situ* heating, together with the STEM-EDX and TKD characterization of the bent NWs, indicates that the diffusion of Au into Fe nanocavities and GBs caused the lateral (i.e., parallel to the NW axis) expansion of the Fe layer. Let us first assume that the partial diffusion coefficients of Au and Fe along the Fe GBs are equal. In this case, all Au atoms penetrating along the Fe GBs will replace the Fe atoms there, and with the average grain size in the PX Fe of 66 nm (Figure 4.4), one monolayer of Au at the GB will cause a lateral strain of 6×10^{-4}, 1 order of magnitude lower than the initial mismatch strain. However, in the case that Au diffuses along the GBs much faster than Fe (GB Kirkendall effect), the accretion of excess Au at the GB will not be accompanied by any outdiffusion of Fe. In this case, accretion of one monolayer of Au at the GBs will cause a Kirkendall strain of 0.004, comparable with the lattice mismatch strain. (see Figure. 4.15a, Figure 4.16)

We can detail the estimation of GB Kirkendall effect induced irreversible bending at the temperatures above 300 °C. The NW#1 bent in the opposite direction at 400 °C and 500 °C, indicating that the stress state of the Fe layer changed from tension to compression. We attribute this lateral expansion of the PX Fe layer to the accretion of Au atoms at the GBs in Fe, as observed in the STEM-EDX micrographs, and is shown schematically in Figure 4.17. However, due to the high solubility of Fe in Au [33] the diffusion flux of Au along the

GBs in Fe can be accompanied by nearly equal flux of Fe atoms in the opposite direction, either leaving the Fe layer and dissolving in the Au NW, or re-distributing along the Fe-Au interface (chemical GB interdiffusion). Thus, Fe atoms leaving the Fe layer may compensate its lateral expansion due to accretion of Au atoms. We will estimate below whether a simple GB interdiffusion with equal partial GB diffusion coefficients of Au and Fe (i.e. full balance of the GB diffusion fluxes) can account for the observed bending of the NW#1.

The diameters of the Fe and Au atoms are 0.2482 and 0.2884 nm, respectively. With the average grain size in the PX Fe layer of 66 nm, replacing one monolayer of Fe at the GB with a monolayer of Au will cause a lateral strain of 6×10^{-4}, one order of magnitude lower than the initial mismatch strain. Therefore, the simple GB interdiffusion with equal partial GB diffusion coefficients of Au and Fe cannot account for the NW bending in the opposite direction. Let us now assume that Au diffuses much faster than Fe along the Fe GBs (GB Kirkendall effect). In this case, accretion of Au at the GBs will not be accompanied by any significant outdiffusion of Fe. One full monolayer of Au will cause a strain of 0.004, comparable with the lattice mismatch strain. Accommodating two-three monolayers of Au in the Fe GBs will fully compensate the lattice mismatch strain and lead to the NW bending in the opposite direction, in accordance with our experimental observations. From the measurements in Figure 4.13b, the width of the Au-rich diffusion/segregation layer at the Fe GBs after annealing at 400°C and 500°C for 20 min is about 2 nm. Thus we conclude that the major part of plastic bending of the bi-metallic Au-Fe NW at high temperatures is caused by the GB Kirkendall effect. It should be noted that the formation of "GB diffusion wedges" of the diffuser during the GB Kirkendall effect has been described by Klinger and Rabkin [36].

A schematic representation of the atomic and vacancy fluxes during the GB Kirkendall effect is presented in Figure. S10. For simplicity, we assume that the Fe atoms at the GB are immobile. The GB diffusion of Au atoms into the GB in the PX Fe layer causes an equal in amplitude flux of vacancies in the opposite direction. The divergence of this flux describes the material (Au) accretion at the GB and concomitant lattice drift of both grains away from the GB, assuming that the GB is a perfect source of vacancies. It is this lattice drift which causes a lateral strain of the PX Fe layer. The GB vacancy flux emerges at the triple line where the GB contacts the Fe-Au interface. It is then re-distributed along the Fe-Au interface, which is also a perfect sink of vacancies because of its incoherent nature. The divergence of the interface vacancy diffusion flux causes a concomitant lattice drift of the Au NW in the direction of interface. Thus, an overall picture of the mass balance is as follows: the near-interface Au atoms diffuse into the GBs in the PX Fe layer and cause a lateral expansion of the latter. As a result, the diameter of the Au NW is slightly decreasing, and the NW bends in the direction of Au.

Formation of the GB diffusion wedge of 2−3 Au monolayers in thickness can fully compensate the initial mismatch strain and cause NW bending of similar magnitude in the opposite direction. Therefore, the main underlying mechanism of the plastic bending at 500 °C is the imbalanced GB interdiffusion in the PX Fe layer and the GB Kirkendall effect [36].

Moreover, it should be noted that Fe lattice diffusion into Au contributed to the lateral shrinkage of the Au NW, because the lattice parameter of the Au(Fe) alloys decreases with increasing Fe content [33] and partial lattice diffusivities of Au and Fe in dilute Au(Fe) solid solution are nearly equal [42]. This lattice shrinkage in the Au NW also contributes to the NW curvature (Figure 4.15b).

Finally, it should be emphasized that at relatively low temperatures and short annealing times employed in the in situ heating of NW#1 and NW#2, lattice diffusion of Fe into Au is very limited (as evidenced by the limited interface migration distance and formation of disconnections at the interface, see previous chapter), therefore, the GB Kirkendall effect is the dominant factor in the plastic bending of the NWs when annealing was conducted below 500°C.

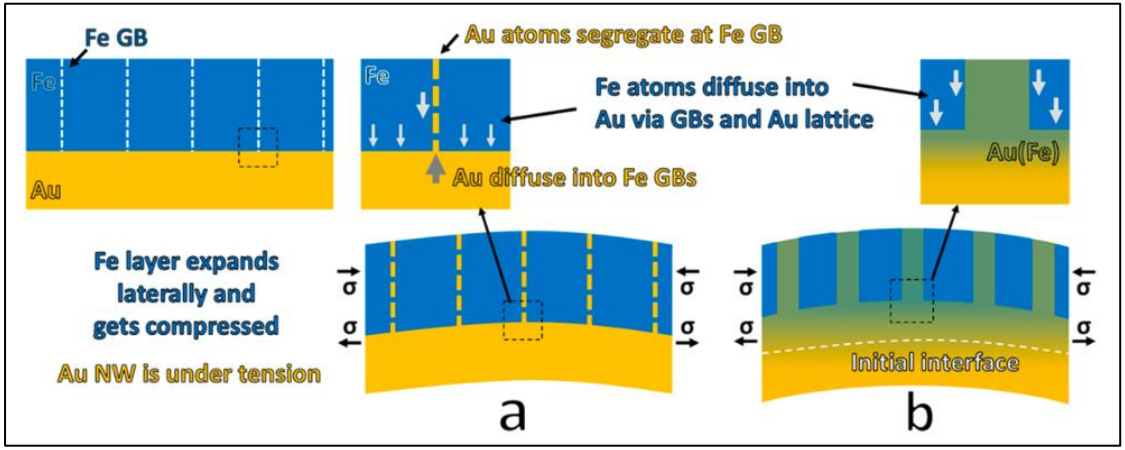

Figure 4.15 Two mechanisms to modulate the bending curvature of an Au/Fe metallic NW. Schematic illustrations of (a) Au atom accretion at the GBs in PX Fe layer via the GB Kirkendall effect and (b) diffusion of Fe into Au, formation of Au(Fe) interdiffusion zone, and interface migration. Both mechanisms cause lateral expansion of the Fe layer and contraction of the Au NW, which lead to the NW bending toward Au

Our TKD measurements of the longitudinal cross sections of the Au NWs did not reveal any low-angle GBs (Figure 4.11b and Figure 4.14c). Assuming that the bending of Au NWs proceeds by classical dislocation plasticity mechanisms, it was expected that geometrically necessary dislocations (GNDs) would accommodate the plastic bending and self-organize at elevated temperatures in the form of low-angle GBs according to the classical polygonization mechanism [43-44]. In contrast, we observed a gradual change of lattice orientation and formation of TBs in the bent Au NWs. This is consistent with the defect-free nature of as-grown Au NWs (no pre-existing dislocations or dislocation sources) and indicates that the energy barrier associated with nucleation of twinning dislocations (Shockley partials) is lower than that of GNDs. It is should be noted that diffusion-controlled irreversible NW bending with little involvement of lattice dislocations uncovered in the present work bears some similarities to the time-dependent plastic deformation by Coble creep [45] and Nabarro−Herring creep [46, 47]. GB Kirkendall effect and Coble creep are active at low homological temperatures at which the GB diffusion is a dominant mode of mass transport and lattice growth and expansion. On the other hand, full diffusion intermixing and Nabarro−Herring creep operate at higher temperatures and longer annealing times at which the plastic bending or deformation are dominated by bulk diffusion.

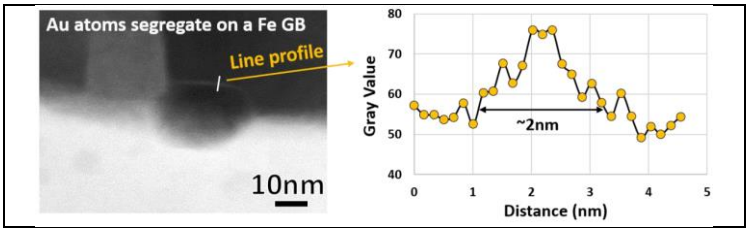

Figure 4.16 Au atoms accretion at the GBs in Fe causing lateral expansion of the Fe layer and the NW bending towards Au. The HAADF-STEM image-based measurement of the width of Au diffusion/segregation layer at the Fe GB after the *in-situ* annealing at 500 ºC.

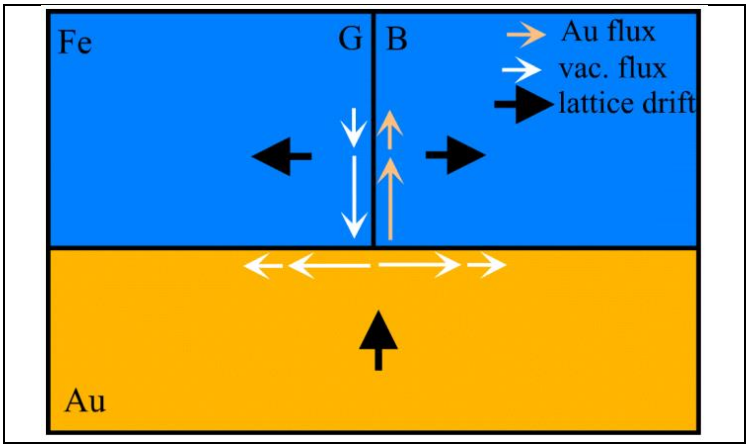

Figure 4.17 Schematic illustration of Au and vacancy diffusion fluxes during the GB Kirkendall effect. For simplicity, we assumed that only Au atoms diffuse along the GBs in Fe. Only one GB in the PX Fe layer is shown. The divergence of the vacancy flux along the GB and along the Fe-Au interface causes the lattice drifts.

We also tested the feasibility of using a thin layer of Fe to bend the Au NW and then dissolve the Fe. We employed NW#3 with a ~50 nm thick Fe layer for this experiment. The NW was

annealed in a rapid thermal annealing furnace under forming gas flow (Ar−10% H_2, 6N purity) at a temperature of 600 °C for 30 min. Observations shown in Figure 4.18a-d, the radius of curvature changed from 43 to −56 μm after annealing, with most of the Fe layer being dissolved in the Au NW.

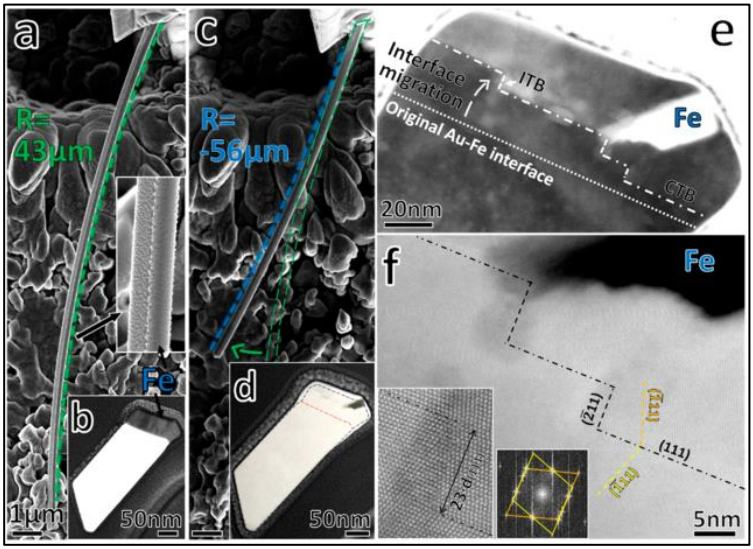

Figure 4.18 Bending by dissolving Fe layer in the Au NW, revealed by the characterization of NW#3 after annealing at 600 °C for 30 min. (a−d) Morphology and cross-section of the as-synthesized and annealed NW#3, (e) dark-field (DF)-STEM image showing the TBs formed in the interdiffusion zone during the bending and interface migration, and (f) HAADF-STEM image characterizing the TB

We estimated the volume fractions of the Fe layer and the Au NW in the pristine bimetallic NW to be 16.5% and 83.5%, respectively (Figure 4.19). This is equivalent to the overall

composition of Au−13.5 atom % Fe, so that full homogenization of the NW would result in a decrease of lattice parameter from 4.078 Å (in pure Au) to 4.041 Å [33, 48]. Taking into account that the lattice parameter of body-centered cubic (BCC) Fe is 2.867 Å, full homogenization of the NW would result in a volume swelling of 6.5%. This estimate is very close to the measured increase of the cross-sectional area of 5.5% determined by comparing Figure 4.18b and d. This indicates that even nearly full dissolution of the Fe layer does not cancel internal stresses in the NW and its plastic bending. This is because the Au NW contracts upon dissolving Fe (due to the decrease of the lattice parameter of the Au(Fe) solid solution), while the former Fe coating expands due to its transformation into the Au(Fe) solid solution (with atomic volumes of 11.78 $Å^3$ and 16.50 $Å^3$ in BCC Fe and in the Au(Fe) solid solution, respectively) (Figure 4.15b). A closer observation showed a TB formed in the interdiffusion zone and exhibiting both CTB and ITB sections. It formed during the migration of the Au−Fe interface toward the Fe layer and may be responsible for partial relaxation of the bending stresses (Figure 4.20).

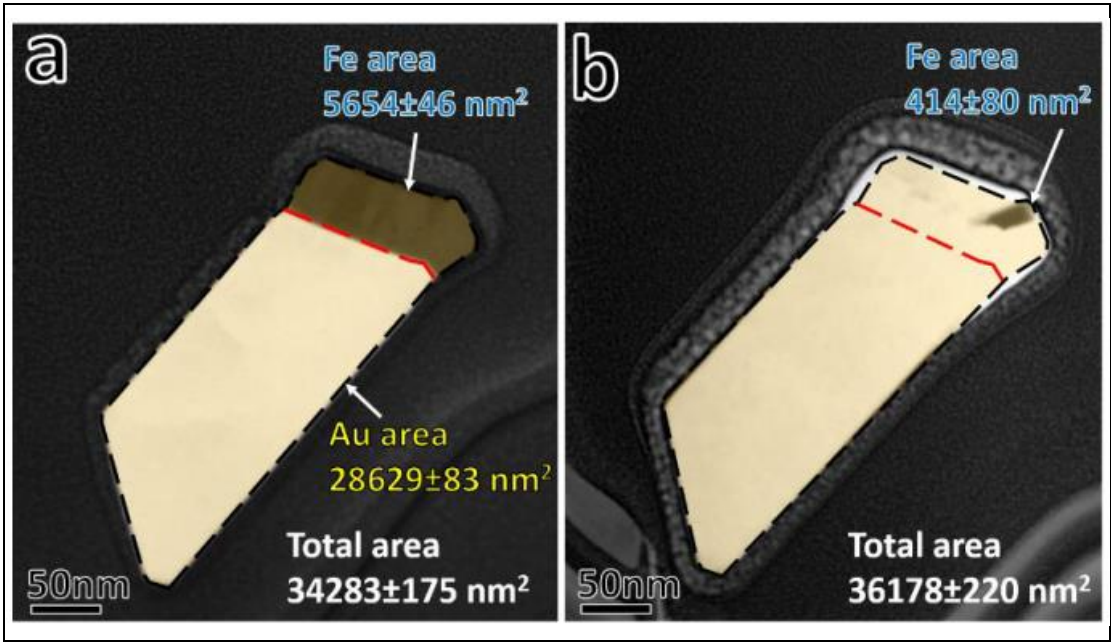

Figure 4.19 The evolution of the cross-sectional dimensions of the NW#3 after annealing at 600°C for 30 min. The estimation was based on the measurements of the areas in HAADF-STEM images before (a) and after (b) annealing. Images were taken along the [01$\bar{1}$] Z.A. of Au.

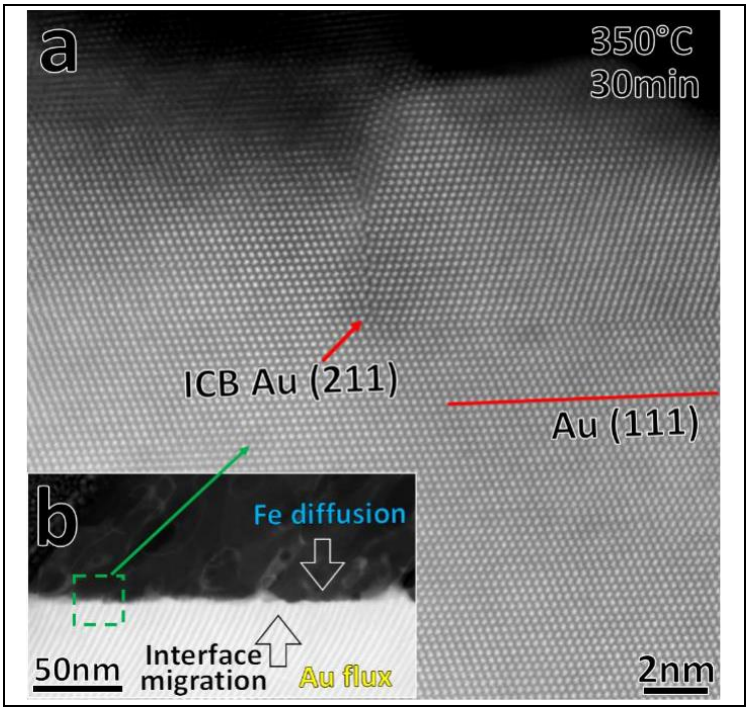

Figure 4.20 The formation of an incoherent twin boundary (ITB) induced by interface migration and bulk Fe-Au interdiffusion. (a) an atomic resolution HAADF-STEM image showing an ITB (211) formed in the vicinity of the incoherent Au – PX Fe interface after annealing at 350 °C for 30 min. (b) the lower magnification HAADF-STEM image showing the nano-roughness of the interface which indicates the migration process. Images were taken along the $[0\bar{1}1]$ Z.A. of Au.

5. CONCLUSION AND OUTLOOK

Present work had metallic NWs in focus, in particular the NWs growth, the interdiffusion studies at nanoscale based on NWs and the plastic deformation of bimetallic NW.

Chapter 1 represents the introduction to this work. It contains the necessary fundamental tools, theories and models of nano materials, i.e. fundamentals about PVD and crystal growth.

Chapter 2 was dedicated to explain the NW growth process, which was developed in our research group more than a decade ago. Rather than putting a model, Chapter 2 is aimed to optimize the parameters and discuss the underlying reasons for this particular NW production process. As a result, we achieved a PVD process for production of single-crystalline metallic NWs, which has great reproducibility levels. This process not only results on big numbers of NWs, but also gives a great amount of control for NW production process. In addition, it generates flexibility towards extending the material combinations with their architecture. Chapter 3 and Chapter 4 are results of that control of architecture. In both these chapters we used bimetallic NWs which were prepared with the know-how we gained thorough the Chapter 2.

Chapter 3 is focused on interdiffusion at nano scale. In the case of interdiffusion in the Au-Fe bimetallic NWs, the rate of intermixing was significantly slower than what could be expected based on diffusion parameters obtained in the literature for the bulk Au-Fe diffusion couples. Moreover, we observed a significant directional anisotropy of Fe penetration into Au. We observed that the Fe layer on the Au {100} facets is single crystalline and the corresponding Au-Fe interface is smooth and coherent. On the contrary, the Fe layer on the Au {111} facets was polycrystalline and the corresponding Au-Fe interface was rough and incoherent. Therefore, we stated that the interdiffusion in the studied NWs is controlled by the mobility of Au-Fe interfaces, and proposed a simple kinetic

model enabling to determine the absolute values of interface mobility from the interdiffusion data.
In Chapter 4 we studied the changes of the overall shape of the one-sided bimetallic Au-Fe NWs during thermal cycling and annealing. We found that up to the temperature of 300°C the NWs reversibly bend in the direction of Fe upon heating. This reversible bending is associated with the mismatch of thermal expansion coefficients of Au and Fe. However, at higher temperatures an irreversible plastic bending in the opposite direction was observed. Our microstructure investigation indicated that this plastic bending is associated with the unbalanced inflow of Au along the grain boundaries in Fe layer. Our results open the way of controlled plastic forming of ultra-strong metal nanostructures.

This work has shown that metallic NWs can be consistently produced, that bimetallic NWs can be used as a medium for further research on interdiffusion on nano scale, and that we can induce plastic deformation on NWs using diffusion. Further research on the topic is required. Based on the knowledge this work provided on NWs, some elements of the future research consists of continuation of the presented work on NW growth and plastic deformation and some of them will be new research ideas.
As a continuation of the current research work, the model from Chapter 3 should be extended to different bimetallic NW couples. Observations over different bimetallic NWs will be able to show where our model stands. In addition to the one sided bimetallic couples, research will be extended to core shell NW couples. A further work for nano-diffusion studies is the in-situ TEM observations. The aim here is to put the time stamps over the observations, which we already have.
Extending the nano-deformation studies discussed in Chapter 4 is another promising future research goal deriving from this work. Some work on this topic using Au-Pd bimetallic NWs has been already done. As next step, changing the core material is

planned in order to have a comparative study over deformation behavior and how to utilize this behavior to create desired shapes.

A new interesting study for Au-Pd bimetallic NWs is the hydrogenation cycling of the NWs. Since Pd expands upon hydrogen (H) absorption, we expect a bending at Au-Pd NWs. The curvature at H absorbed state and the variation of it at the H desorbed state should be further studied using in-situ SEM techniques. Additional work should include the comparative study of H sensing capabilities of curved and straight Au-Pd NWs.

An extended study on mechanical properties of NWs as well as NPs is planned in the research group. This will be possible thanks to two newly acquired tools (FIB and Nanoindenter). Mechanical testing is another way to understand the plastic deformation and shaping at nano scale.

[1] Kuhlmann-Wilsdorf, D. The Theory of Dislocation-Based Crystal Plasticity. Philos. Mag. A (1999).

[2] De Cooman, B. C.; Estrin, Y.; Kim, S. K. Twinning-Induced Plasticity (TWIP) Steels. Acta Mater. (2018).

[3] Langdon, T. A Unified Approach to Grain Boundary Sliding in Creep and Superplasticity. Acta Metall. Mater. (1994).

[4] Li, Z.; Pradeep, K. G.; Deng, Y.; Raabe, D.; Tasan, C. C. Metastable High-Entropy Dual-Phase Alloys Overcome the Strength−Ductility Trade-off. Nature. (2016).

[5] Richter, G.; Hillerich, K.; Gianola, D. S.; Monig, R.; Kraft, O.; Volkert, C. A. Ultrahigh Strength Single Crystalline Nanowhiskers Grown by Physical Vapor Deposition. Nano Lett. (2009).

[6] Mordehai, D.; Lee, S.-W.; Backes, B.; Srolovitz, D. J.; Nix, W. D.; Rabkin, E. Size Effect in Compression of Single-Crystal Gold Microparticles. Acta Mater. (2011).

[7] Roos, B.; Kapelle, B.; Richter, G.; Volkert, C. Surface Dislocation Nucleation Controlled Deformation of Au Nanowires. Appl. Phys. Lett. (2014).

[8] Chen, L. Y.; He, M.-R.; Shin, J.; Richter, G.; Gianola, D. S. Measuring Surface Dislocation Nucleation in Defect-Scarce Nanostructures. Nat. Mater., (2015).

[9] Mordehai, D.; David, O.; Kositski, R. Nucleation-Controlled Plasticity of Metallic Nanowires and Nanoparticles. Adv. Mater., (2018).

[10] Lee, S., Vaid, A., Im, J. et al. In-situ observation of the initiation of plasticity by nucleation of prismatic dislocation loops. Nat Commun., (2020).

[11] Lee, S.; Im, J.; Yoo, Y.; Bitzek, E.; Kiener, D.; Richter, G.; Kim, B.; Oh, S. H. Reversible Cyclic Deformation Mechanism of Gold Nanowires by Twinning−Detwinning Transition Evidenced from In Situ TEM. Nat. Commun. (2014).

[12] Sharma, A.; Hickman, J.; Gazit, N.; Rabkin, E.; Mishin, Y. Nickel Nanoparticles Set a New Record of Strength. Nat Commun., (2018).

[13] Csikor, F. F.; Motz, C.; Weygand, D.; Zaiser, M.; Zapperi, S. Dislocation Avalanches, Strain Bursts, and the Problem of Plastic Forming at the Micrometer Scale. Science. (2007).

[14] Greer, J. R.; De Hosson, J. T. M. Plasticity in Small-Sized Metallic Systems: Intrinsic versus Extrinsic Size Effect. Prog. Mater. Sci., (2011).

[15] Weinberger, C. R.; Cai, W. Plasticity of Metal Nanowires. J. Mater. Chem., (2012).

[16] Batra, N. M.; Syed, A.; Costa, P. M. Current-Induced Restructuring in Bent Silver Nanowires. Nanoscale. (2019).

[17] Stephenson, G. B. Deformation during Interdiffusion. Acta Metall., (1988).

[18] Smigelskas, A.; Kirkendall, E. Zinc Diffusion in Alpha Brass. Trans. AIME (1947).

[19] Yu, H. C.; Van der Ven, A.; Thornton, K. Simulations of the Kirkendall-Effect-Induced Deformation of Thermodynamically Ideal Binary Diffusion Couples with General Geometries. Metall. Mater. Trans. A (2012).

[20] Daruka, I.; Szabo, I.; Beke, D.; Cserhati, C.; Kodentsov, A.; Van Loo, F. Diffusion-Induced Bending of Thin Sheet Couples: Theory and Experiments in Ti-Zr System. Acta Mater. (1996).

[21] Boettinger, W. J.; McFadden, G. B. Bending of a Bimetallic Beam Due to the Kirkendall Effect. J. Phase Equilib. Diffus. (2010).

[22] Deshpande, R.; Cheng, Y. T.; Verbrugge, M. W. Modeling Diffusion-Induced Stress in Nanowire Electrode Structures. J. Power Sources. (2010).

[23] Liu, X. H.; Zheng, H.; Zhong, L.; Huang, S.; Karki, K.; Zhang, L. Q.; Liu, Y.; Kushima, A.; Liang, W. T.; Wang, J. W.; et al. Anisotropic Swelling and Fracture of Silicon Nanowires During Lithiation. Nano Lett. (2011).

[24] Luo, L.; Yang, H.; Yan, P.; Travis, J. J.; Lee, Y.; Liu, N.; Molina Piper, D.; Lee, S.-H.; Zhao, P.; George, S. M.; et al. Surface-Coating Regulated Lithiation Kinetics and Degradation in Silicon Nanowires for Lithium Ion Battery. ACS Nano (2015).

[25] Li, Z.; Tan, X.; Li, P.; Kalisvaart, P.; Janish, M. T.; Mook, W. M.; Luber, E. J.; Jungjohann, K. L.; Carter, C. B.; Mitlin, D. Coupling In Situ TEM and Ex-Situ Analysis to Understand Heterogeneous Sodiation of Antimony. Nano Lett. (2015).

[26] Honjo, G.; Takayanagi, K.; Kobayashi, K.; Yagi, K. Ultra-High- Vacuum In-Situ Electron Microscopy of Growth Processes of Epitaxial Thin Films. J. Cryst. Growth. (1977).

[27] Lide, D. R., Ed. CRC Handbook of Chemistry and Physics; CRC press: Boca Raton, FL, (2004).

[28] Timoshenko, S. Analysis of Bi-Metal Thermostats. J. Opt. Soc. Am., (1925).

[29] Nix, W.; Clemens, B. Crystallite Coalescence: A Mechanism for Intrinsic Tensile Stresses in Thin Films. J. Mater. Res. (1999).

[30] Freund, L. B.; Suresh, S. Thin Film Materials: Stress, Defect Formation and Surface Evolution; Cambridge University Press. (2004).

[31] Amram, D.; Amouyal, Y.; Rabkin, E. Encapsulation by Segregation − A Multifaceted Approach to Gold Segregation in Iron Particles on Sapphire. Acta Mater. (2016).

[32] Zhang, S.; Kwakernaak, C.; Sloof, W.; Bru¨ck, E.; van der Zwaag, S.; van Dijk, N. Self Healing of Creep Damage by Gold Precipitation in Iron Alloys. Adv. Eng. Mater. (2015).

[33] Okamoto, H.; Massalski, T.; Swartzendruber, L.; Beck, P. The Au − Fe (Gold-Iron) System. Bull. Alloy Phase Diagrams (1984).

[34] Shin, J.; Chen, L. Y.; Sanli, U. T.; Richter, G.; Labat, S.; Richard, M.-I.; Cornelius, T.; Thomas, O.; Gianola, D. S. Controlling Dislocation Nucleation-Mediated Plasticity in Nanostructures via Surface Modification. Acta Mater. (2019).

[35] Sedlmayr, A.; Bitzek, E.; Gianola, D. S.; Richter, G.; Mönig, R.; Kraft, O. Existence of Two Twinning-Mediated Plastic Deformation Modes in Au Nanowhiskers. Acta Mater. (2012).

[36] Klinger, L.; Rabkin, E. Theory of the Kirkendall Effect during Grain Boundary Interdiffusion. Acta Mater. (2011).

[37] Langdon, T. A Unified Approach to Grain Boundary Sliding in Creep and Superplasticity. Acta Metall. Mater. (1994).

[38] Rabkin, E., Metastable Porosity in Thin Polycrystalline Films. Scr. Mater. (2013).

[39] Roth, T., The Surface and Grain Boundary Energies of Iron, Cobalt and Nickel. Mater. Sci. Eng. (1975).

[40] Benoit, M.; Langlois, C.; Combe, N.; Tang, H.; Casanove, M.-J., Structural and Electronic Properties of the Au (001)/Fe (001) Interface from Density Functional Theory Calculations. Phys. Rev. B. (2012).

[41] Amram, D.; Klinger, L.; Rabkin, E., Phase Transformations in Au (Fe) Nano-and Microparticles Obtained by Solid State Dewetting of Thin Au–Fe Bilayer Films. Acta. Mater. (2013).

[42] Iijima, Y.; Yamazaki, Y. Interdiffusion Between Metals of Widely Different Self-Diffusion Rates, Defect Diff us. Defect Diffus. Forum (2005).

[43] Gilman, J. J. Structure and Polygonization of Bent Zinc Monocrystals. Acta Metall. (1955).

[44] Sun, Z.; Huang, C.; Guo, J.; Dong, J. T.; Klie, R. F.; Lauhon, L. J.; Seidman, D. N. Strain-Energy Release in Bent Semiconductor Nanowires Occurring by Polygonization or Nanocrack Formation. ACS Nano (2019).

[45] Coble, R. A Model for Boundary Diffusion Controlled Creep in Polycrystalline Materials. J. Appl. Phys. (1963).

[46] Nabarro, F. Report of a Conference on the Strength of Solids; The Physical Society. (1948).

[47] Herring, C. Diffusional Viscosity of a Polycrystalline Solid. J. Appl. Phys. (1950).

[48] Kubaschewski, O.; Ebert, H. Diffusion Measurements in Gold and Platinum Alloys. Z. Elektrochem. (1944).

[49] Qi, Y., Richter, G., Suadiye, E., Kalina, M., Rabkin, E., Plastic Forming of Metals at the Nanoscale:Interdiffusion-Induced Bending of Bimetallic Nanowhiskers, ACS Nano, 2020.

APPENDIX A

A.1 Bimetallic NW systems

Bimetallic nanowires (NWs) refer to nanostructures that are composed of two different metals, typically with one metal forming the core and the other forming the shell. These NWs have unique properties that are different from those of their individual components and have potential applications in various fields, including catalysis, sensing, and energy storage. The synthesis of bimetallic NWs can be achieved through various methods, such as chemical vapor deposition, electrochemical deposition, and galvanic replacement reaction. The properties of bimetallic NWs can be tailored by adjusting the composition, size, and shape of the NWs. Additionally, the use of bimetallic NWs in catalysis has shown promising results due to their high surface area and unique surface properties, making them potential candidates for a wide range of catalytic reactions.

Another possible way to produce bimetallic NWs using MBE. The existing metallic NW can serve as a ‘template’ or substrate for the deposition of the second metal. By carefully controlling the deposition conditions and parameters, such as the deposition rate and temperature, it is possible to achieve the desired bimetallic structure and composition. One metal forms the core and the other metal forms the secondary layer, or for creating heterostructured NWs with different metal segments along the length of the NW.

Using the Single crystalline Au NWs as substrate further research has been carried out on MBE to produce bimetallic NWs. In this work, we have prepared several bimetallic NW

systems with the Au being the core NW material and Mo being the substrate for single crystalline Au NWs. Table 2.4 lists the lattice parameters of the metals used in the bimetallic NWs.

Table A.1 List of the elements used for bimetallic NW systems.

Element	Lattice parameter (nm)
Au	0.40
Fe	0.28
Pd	0.38
Pt	0.39
Ag	0.41

Bimetallic NWs were prepared by physical vapor deposition onto Mo substrates using MBE under a near-equilibrium growth condition. The Au NWs deposition rate was again 0.5Å/s at 760 °C and the deposition lasted 2 hours. The Au deposition was followed by the deposition of secondary metal layer at room temperature. Room temperature (RT) growth gives limited surface diffusion capabilities to the secondary metallic layer but eliminates the disappearance of the Au NWs via dewetting. Both depositions were carried out in the same chamber without breaking the ultra-high vacuum. In the following subsections, the characterization of four bimetallic NWs, Au – Fe, Au – Pd, Au – Pt and Au - Ag, are shown through SEM and TEM images.

A.1.1 Characterization of Au – Fe bimetallic nanowires

The characterization of Au – Fe bimetallic NWs is based on close up SEM images detailing the morphology of the Fe layer (Figures 2.26-28). In addition, cross section TEM images are focused on crystal structure of the Au core (Figures 2.29).

Fe deposition with a relative deposition thickness of 200nm show three different features, as depicted and described directly on the Figures 2.26-27. Feature 3 shows the smallest size particles (8~12 nm), each of the particles not showing any connection to the others. That is consistent with the shadowing effect of Thornton model. We also deposited samples with 50nm relative thickness in order to understand if feature 3 is a growth feature or it comes from shadowing effect (Figure 2.26). Samples show slight beginning of features 1 and 2 but not feature 3. Thus, it can be inferred that feature 3 is the result of shadowing effect. When we consider the feature 1 and 2 and the differences seen in these two features we can refer to different surface diffusion rates in different NW surfaces. This also explains polycrystalline and single crystalline growth on (100) and (111) Au NW planes.

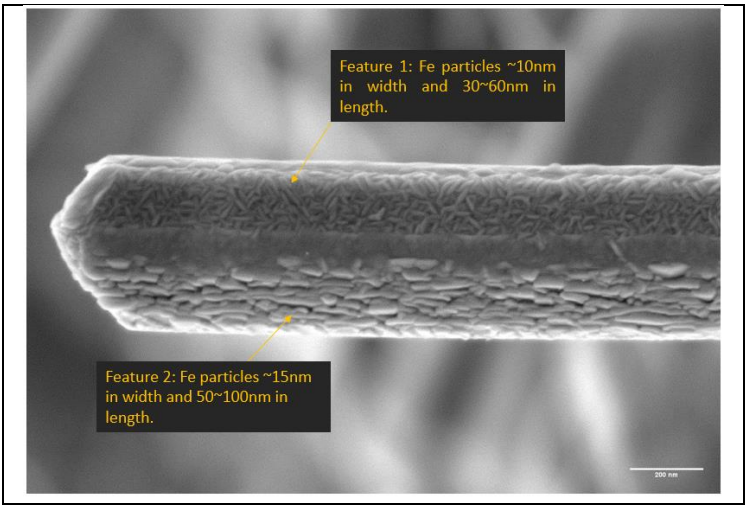

Figure A.1 Close up of Au-Fe NWs. Different facets of the NW core shows to have different Fe layer morphologies. Scale bar is 200 nm. SEM images.

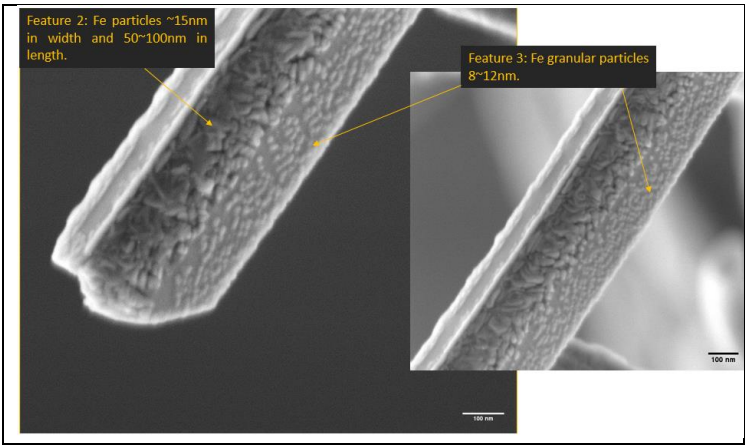

Figure A.2 Close up of Au-Fe NWs. As a result of NW shadowing, smaller sized particles are visible (feature 3). Scale bar in both images is 100 nm. SEM images.

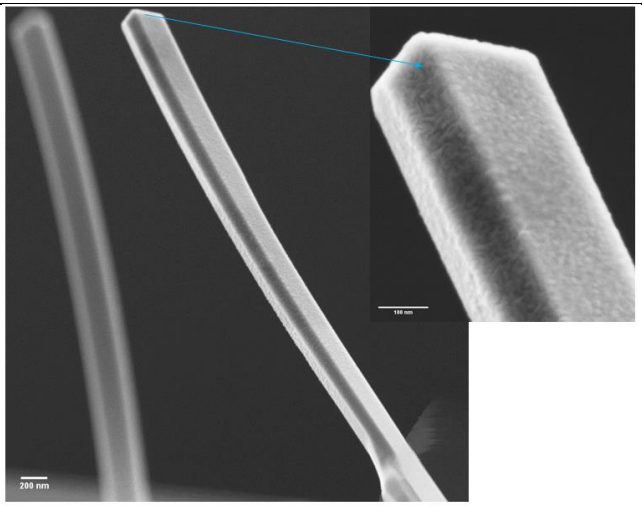

Figure A.3 Bimetallic Fe - Au NW after Fe deposition of 50nm thickness. A continuous film rather than interruptions is visible. Scale bars are 200 nm (left) and 100 nm (right). SEM images.

As shown in Figure A.4, TEM cross section analysis of the Au-Fe NW was conducted and diffraction patterns show single crystalline defect free structure of the Au core. With this said we have observed also twins at some of Au NWs. Detailed TEM characterization for Au-Fe bimetallic NWs is given in chapter 3

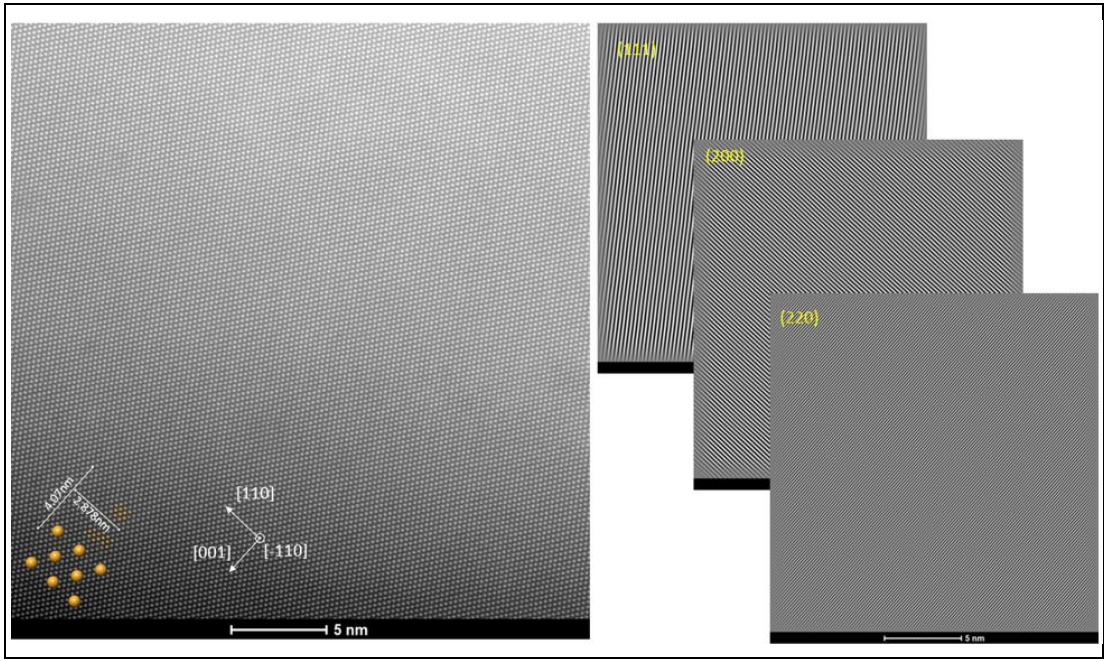

Figure A.4 Defect free Au core in different orientations. Scale bars are 5nm. TEM images

A.1.2 Characterization of Au – Pd bimetallic nanowires

Multiple samples of bimetallic Au-Pd NW system were produced for later hydrogenation experiments. A first look to the Au-Pd NWs showed some equiaxed (feature 1 and jigsaw puzzle (feature 2) shaped Pd structures. (Figures A.5-8).

Due to the close lattice parameter (Table A.1), the Pd layer has exact same crystallographic orientation as the Au layer it was deposited onto (Figure A.8). The Au whisker mainly has {111} and {001} facets with a round corner connecting them. Even though Pd layer seems to be polycrystalline, diffraction patterns showed that Pd layer is in fact a single crystalline film.

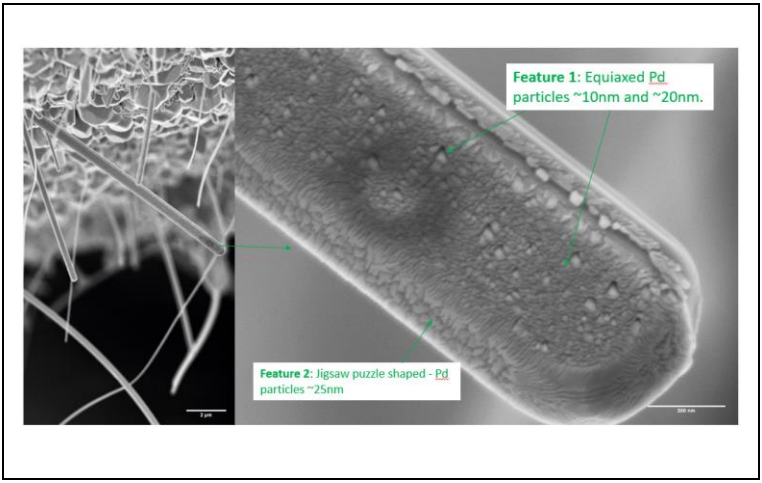

Figure A.5 Equiaxed and jigsaw puzzle shaped structures on Au-Pd NW. Scale bars are 2 µm (left) and 200 nm (right). SEM images.

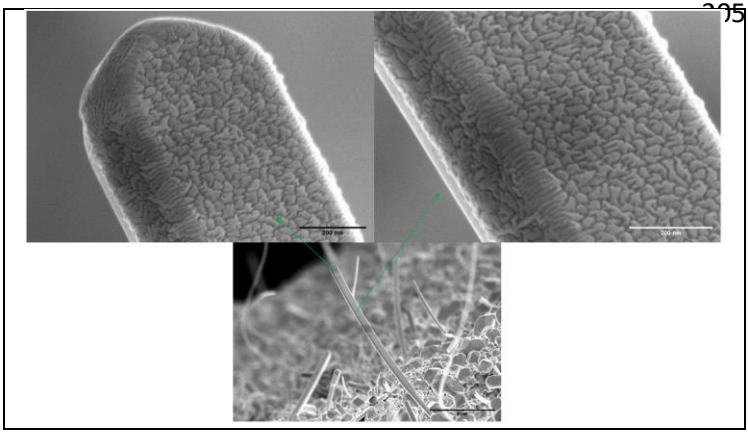

Figure A.6 Close-up to a jigsaw puzzle structure of AU-Pd NW. Scale bars are 200 nm (top) and 5 µm (bottom). SEM images.

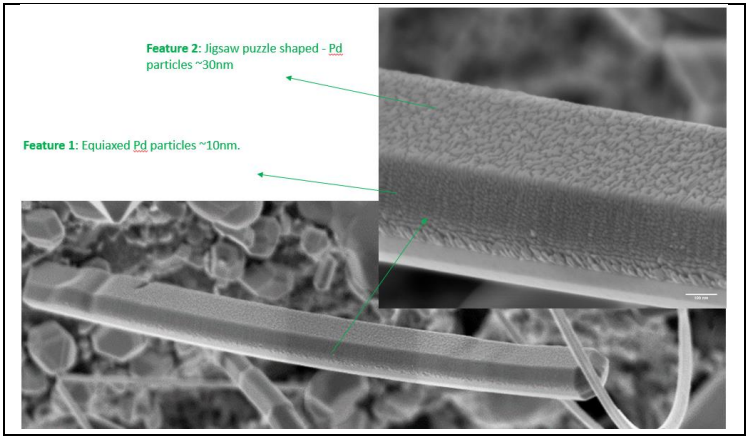

Figure A.7 Bimetallic Au-Pd NW shows both features together. Scale bar is 100 nm. SEM images.

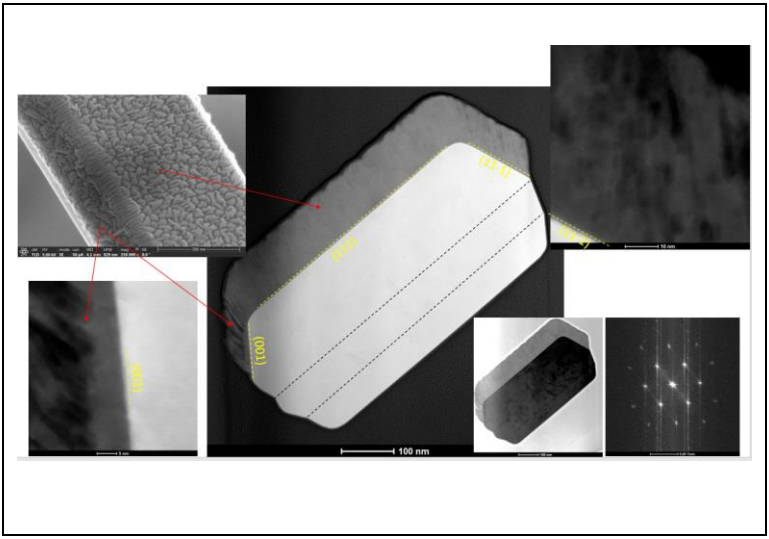

Figure A.8 TEM cross section characterization of a Au-Pd NW.

With the single crystalline Pd film, observation it is obvious that further research on the characterization is required.

A.1.3 Characterization of Au – Pt and Au – Ag bimetallic nanowires

Bimetallic Au-Pt NWs were produced and characterized. SEM images of these Au-Pt NWs showed four features as described in Figures A.9-11: rod shaped towards the NW tip (feature 1), equiaxed on the facets (feature 2), zig-zag on the edges (feature 3) and rod shaped towards the NW tip with larger particle size (length ~ 40 nm).

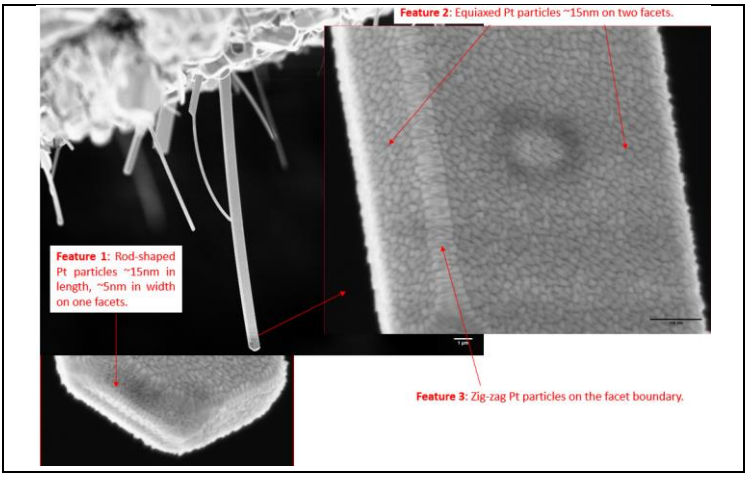

Figure A.9 Three features observed on Au-Pt NWs. Scale bars are (left) 1µm, (right) 100nm. SEM images.

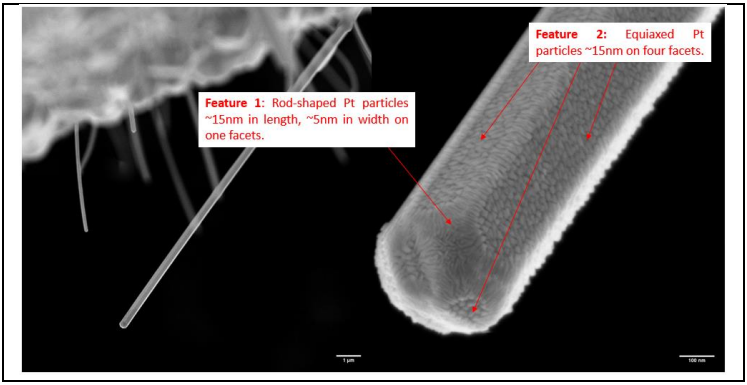

Figure A.10 Close up tip of another Au-Pt NW. Scale bars are (left) 1µm, (right) 100nm. SEM images.

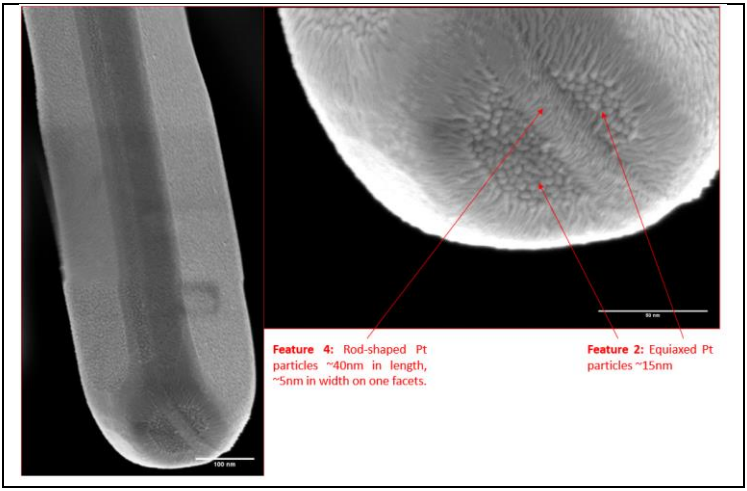

Figure A.11 Close up of the Au-Pt NW tip with an embedded twin. Scale bars are 100 nm (left) and 50 nm (right). SEM images.

In addition, Au-Ag NWs were produced and observed (Figures A.12, 13). Because of similar Au and Ag lattice parameters, bimetallic system was expected to have fully epitaxial growth. We observed that, after a certain thickness, there are some homogenously distributed island-like structures on the NW length (Figures A.12). However, this is not always the case (Figure A.13). Further research is needed to understand the underlying reason of island-like structure.

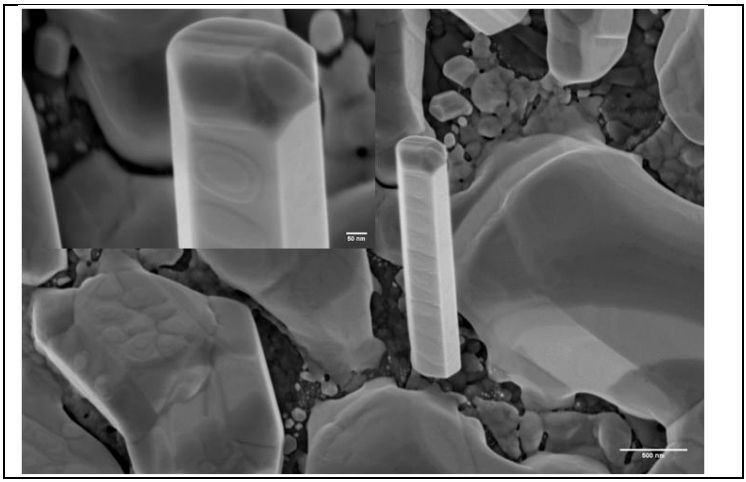

Figure A.12 Close up of bimetallic Au-Ag NW. Island structures are not visible, tip shows a twinned fivefold symmetry. Scale bars are 50 nm (top left) and 500 nm (bottom right). SEM images.

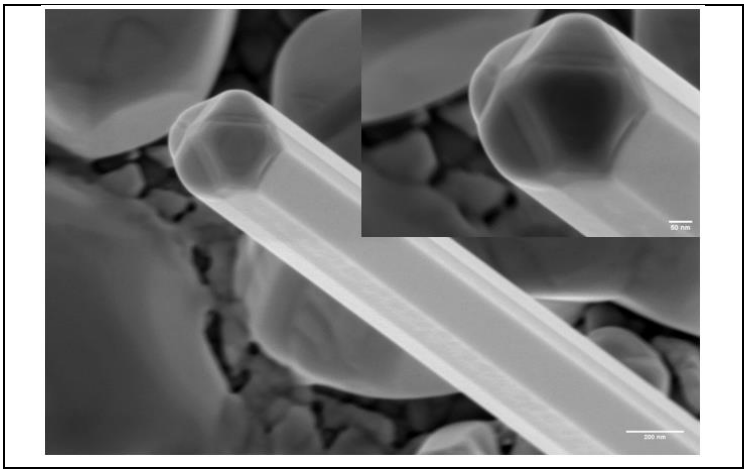

Figure A.13 Close up of bimetallic Au-Ag NW. Island structures are not visible, tip shows a twinned fivefold symmetry. Scale bars are 50 nm (top right) and 200 nm (bottom left). SEM image.